ROYAUME DU MAROC
Université Mohammed V - RABAT -
جامعة محمد الخامس – الرباط –
Faculté des sciences
كلية العلوم
CENTRE D'ETUDES DOCTORALES - SCIENCES ET TECHNOLOGIES

N° d'ordre : 3440

THESE

En vue de l'obtention du :

DOCTORAT

Structure de Recherche : Laboratoire de matière condensée et sciences interdisciplinaires (LaMCScI)
Discipline : Physique.
Spécialité : Energie photovoltaïque et étude des matériaux.

Présentée et soutenue le 06 /03 /2021 par :

Hassan ZITOUNI

DFT study of structural, optical, electronic and transport properties of Perovskites $LaGaO_3$, $SrHfO_3$, $BaZrS_3$ and $CsPbX_3$

JURY

Rachid BENCHRIFA	PES, Université Mohammed V-Rabat, Faculté des sciences	Président de jury
Abdelaziz MHIRECH	PES, Université Mohammed V-Rabat, Faculté des sciences	Rapporteur/Examinateur
Noureddine MASAIF	PES, Université Ibn Tofail-Kénitra, Faculté des sciences	Rapporteur/Examinateur
Omar EL BOUNAGUI	PH, Université Mohammed V-Rabat, Faculté des sciences	Rapporteur/Examinateur
Abdelilah BENYOUSSEF	PES, Académie Hassan II des sciences et techniques, Rabat	Invité d'honneur
Hamid EZ-ZAHRAOUY	PES, Université Mohammed V-Rabat, Faculté des sciences	Directeur de Thèse
Najim TAHIRI	PA, Université Mohammed V-Rabat, Faculté des sciences	Co-Encadrant de Thèse

Année Universitaire : 2020-2021

Remerciements

L'ensemble des travaux de ce projet de recherche doctoral ont été réalisés au sein du Laboratoire de la matière condensée et sciences interdisciplinaires (LaMCScI) de la Faculté des Sciences de l'Université Mohammed V-Rabat, sous la direction de monsieur Hamid EZ-ZAHRAOUY PES à l'Université Mohammed V-Rabat, Faculté des sciences et le co-encadrement de monsieur Najim TAHIRI PA à l'Université Mohammed V-Rabat, Faculté des sciences.

Je tiens à remercier **M. Hamid EZ-ZAHRAOUY**, PES à l'Université Mohammed V-Rabat, Faculté des sciences, mon directeur de thèse qui fut pour moi un directeur attentif, généreux et disponible malgré ses nombreuses charges. Il avait des solutions à tous les problèmes rencontrés, une vision claire sur ma recherche et n'hésitait pas à présenter ses conseils et ses orientations qui témoignent de sa compétence et de sa rigueur scientifique.

Ma reconnaissance et mon profond respect à **M. Najim TAHIRI**, PA à l'Université Mohammed V-Rabat, Faculté des sciences, mon co-encadrent de thèse, qui a été toujours une ressource scientifique de référence et une source capitale de motivation et d'encouragement. C'est à ses côtés que j'ai acquis les incontournables qualités de la recherche scientifique, notamment en termes de rigueur et de précision. Je le remercie également pour sa disponibilité permanente et pour le grand intérêt qu'il a accordé à ce travail.

J'exprime ma reconnaissance à **M. Rachid BENCHRIFA,** PES à l'Université Mohammed V-Rabat, Faculté des sciences, d'avoir accepté de participer à ce jury en tant que Président de jury.

J'adresse tous mes remerciements également à **M. Abdelaziz MHIRECH**, PES à l'Université Mohammed V-Rabat, Faculté des sciences de l'honneur qu'il m'a fait en acceptant d'être rapporteur et examinateur de cette thèse.

Je tiens à exprimer mes sincères remerciements à **M. Noureddine MASAIF**, PES à Université Ibn Tofail, Faculté des sciences de Kénitra, d'avoir accepté de participer à ce jury en tant que rapporteur et examinateur.

Toute ma gratitude et toute ma reconnaissance s'adressent **à M. Omar EL BOUNAGUI**, PH à l'Université Mohammed V-Rabat, Faculté des sciences, d'avoir accepté de participer à ce jury en tant que rapporteur et examinateur.

Je tiens à exprimer mes sincères remerciements à **M. Abdelilah BENYOUSSEF,** Membre résident à l'Académie Hassan II des Sciences et Techniques de Rabat, pour avoir accepté de participer à ce jury en tant qu'invité d'honneur.

Un grand merci aussi spécial qu'il puisse l'être, à l'attention de **mes parents**. Merci d'être mes parents, de m'avoir donné des racines et des ailes, de m'avoir supportée et appuyée durant toutes ces années, de me faire confiance, de m'avoir inculquée de vraies valeurs et de m'avoir permis de devenir la personne que je suis aujourd'hui. Grace à vous j'ai pu m'épanouir et m'ouvrir à la vie et surtout surmonter toute sorte d'épreuves que je rencontre.

Je dédie également ce travail à **Mon frère Houssain**, **ma sœur Houda**, **mon beau-frère Mahmoud** et **ma belle-sœur Hind**, qui ont été toujours à mes côtés. Je vous remercie pour tout ce que vous avez fait pour moi… je vous remercie tous du fond du cœur.

Enfin, Je tiens à remercier chaleureusement toutes les personnes qui, de près ou de loin, ont contribué à l'accomplissement de ce cheminement.

Résumé

Les matériaux pérovskites ABX_3 ont connu un grand intérêt scientifique ces dernière années en raison de leurs propriétés variées ce qui leurs permettent d'être utiliser dans différents domaines tels que la nouvelle anode prometteuse pour batteries rechargeables (Ni / MH), photovoltaïques et photochromiques, …

Dans ce travail de thèse on a déterminé les propriétés électriques, optiques et de transport des matériaux pérovskites de type oxide $LaGaO_3$ et $SrHfO_3$, du matériau pérovskite de type chalcogénure $BaZrS_3$ et aussi de du matériau pérovskite de type halogénure $CsPbX_3$ (X= Br,Cl et I).

Cette étude vise à déterminer le type de pérovskite le plus convenable pour une application photovoltaïque.

Mots clés : Pérovskites, Photovoltaïque, Calcul ab-initio, DFT, Matériaux.

Abstract

ABX_3 perovskite materials have enjoyed great scientific interest in recent years due to their varied properties which allow them to be used in different fields such as the new promising anode for rechargeable batteries (Ni / MH), photovoltaic and photochromic, …

In this thesis work we determined the electrical, optical and transport properties of oxide perovskite materials $LaGaO_3$ and $SrHfO_3$, of chalcogenide perovskite material $BaZrS_3$ and also for halide perovskite material CsPbX3 (X = Br, Cl and I).

This study aims to determine the most suitable type of perovskite for a photovoltaic application.

Keywords: Perovskites, Photovoltaics, Ab-initio calculation, DFT, Materials.

Résumé étendu

Les cellules solaires à base de matériaux pérovskites ont connu un grand intérêt scientifique depuis leur première publication en 2009. Depuis cette date, l'intérêt de la recherche sur les matériaux pérovskites a été étendu à de nombreux types d'applications. Grâce à des études et des recherches intensives, le rendement de conversion de la cellule solaire à pérovskite a été considérablement amélioré jusqu'à 23% dans une courte durée (10 ans). C'est un résultat incroyable par rapport aux cellules solaires au silicium qui ont mis plusieurs décennies à atteindre un rendement aussi élevé. Les recherches portent maintenant sur tous les composants solaires de la pérovskite : le matériau de pérovskite lui-même, la couche de transport d'électrons et de trous ainsi que la structure et les contacts de l'appareil.

Les travaux menés au cours de cette thèse concernent principalement des études abinitio des matériaux pérovskites. Le but de ces études est déterminé les propriétés physiques des différents types de pérovskites en appliquant des contraintes tel que le stress ou le dopage affin de déterminer le type de pérovskite le plus convenable pour une application photovoltaïque.

Au premier chapitre, nous avons présenté les matériaux de type pérovskite, leur première observation, la structure cristalline d'origine. Le facteur de tolérance et le facteur octaèdre sont également introduits. Dans un second temps, nous avons présenté des généralités sur le domaine du photovoltaïque. En particulier, nous avons rappelé le principe de fonctionnement d'une cellule solaire, puis nous avons cité les différentes technologies existantes ainsi que les records d'efficacité de conversion de l'énergie solaire en électricité pour les cellules de laboratoire.

Dans le chapitre II, nous avons détaillé les méthodes qui nous permettent de réaliser notre étude. La méthode basée sur la théorie fonctionnelle de la densité sera mentionnée. La théorie des groupes dans le solide qui nous permet d'effectuer l'analyse de symétrie sera également incluse.

Dans le chapitre III, nous avons étudié les pérovskites de type oxyde $LaGaO_3$ et $SrHfO_3$ présentant une étude théorique des propriétés électroniques, structurelles, de transport et optiques de ces composés. Ces composés ont connu un grand intérêt scientifique en raison de

leurs propriétés qui leur permettent d’être utilise dans diffère domaines tel que les batteries de stockage, les cellules solaires, etc... Ces deux composés adoptent la structure orthorhombique qui se conforme au groupe Pnma dans les conditions ambiantes et à des températures plus élevées, la structure est la pérovskite cubique idéale qui se conforme au groupe spatial Pm3m.

Au chapitre IV, nous avons présenté une étude théorique des propriétés électroniques, structurelles, de transport et optiques de la pérovskite de chalcogénure $BaZrS_3$. Les pérovskites de chalcogénure ABS_3 sont l'actualité de la recherche scientifique est cela est due aux propriétés qu'ils ont montré et qui leurs permettent d’être utilisé dans divers domaine. $BaZrS_3$ cristallise en structure orthorhombique avec le groupe Pnma.

Au chapitre V, nous présentons une étude théorique des propriétés électroniques, structurelles et optiques de la pérovskite halogénure $CsPbX_3$. Les pérovskites d’halogénure ont un rendement proche à celui du silicium commercial, mais les contraintes qui empêchent la commercialisation de cellules solaires à base de pérovskite à base d'halogénures sont l'instabilité chimique dans les conditions ambiantes, la toxicité, la stabilité de la pérovskite aux halogénures organiques et la cancérogénicité probable du plomb et halogénures de plomb.

Table of contents

Introduction

The current energy issue is focused on the energy transition towards renewable and less polluting energies. Applications based on hybrid perovskites have flourished in recent years, especially since the latter's boom as a low-cost material for photovoltaic cells. Hybrid perovskite has become the "black gold" for photovoltaic cells. Since 2009, when a hybrid perovskite was first introduced into a photovoltaic cell, the efficiency of these cells has quadrupled, and has just reached record efficiencies equaling those of silicon-based cells. The predicted efficiency for perovskite-based cells is in the order of 30%, exceeding that of silicon cells.

The interest of these materials stems from several factors: the ease of their synthesis, their low cost and their integration into a photovoltaic architecture. These traits make this form of energy accessible to a wide range of users. The crucial issue for these cells is their industrialization. But certain drawbacks must be overcome to achieve this end: the aging of the layers and the presence of lead are two problems in which many researchers have been interested. Perovskite degrades at temperatures above 40 ° C and is soluble in water. Regarding lead, the opinion of experts is mixed between those who do not consider lead as a problem in view of the extremely low quantities of lead in the devices, and others who point to its toxicity and high solubility in the water. Attempts are underway to substitute lead with other metals, for example tin, but this is at the expense of yields. To find a solution to all these problems, it is necessary to deepen the knowledge of the physico-chemical properties of the material, which are not yet very well known.

A family of hybrid perovskites had already aroused interest in the 1990s for applications in microelectronics such as OLEDs (Organic Light Emitting Diodes) and transistors. But due to the lack of electrical injection possible, these applications had not resulted in commercial devices. What is new with the family of hybrid perovskites of interest for photovoltaics is the relatively high mobility of charge carriers and the possibility of electrical injection. New OLEDS, photodetectors and transistors based on these new hybrid perovskites are now starting to emerge in parallel with the work on perovskite-based cells.The work carried out during this thesis mainly involves abinitio studies of perovskite materials. The aim of these studies is to improve the understanding of the

structural, optical, transport and electronic properties of various type of perovskite, in order to find the most suitable type of material for photovoltaic application.

In Chapter II, we will first detail the methods that allow us to achieve our study. The method based on the density functional theory will be mentioned. The theory of groups in the solid which allows us to perform the symmetry analysis will also be included.

In Chapter III, we will study an oxide perovskites compounds $LaGaO_3$ and $SrHfO_3$ presenting a theoretical investigation of electronic, structural, transport and optical properties of this compounds.

In Chapter IV, we present a theoretical investigation of electronic, structural, transport and optical properties of Chalcogenide perovskite $BaZrS_3$.

In Chapter V, we present a theoretical investigation of electronic, structural, and optical properties of halide perovskite $CsPbX_3$.

Chapter I

General Introduction

I.1 Introduction

This first chapter is an opportunity for us to introduce perovskite-type materials, their first observation, the original crystal structure and the richness of variations identified since. The tolerance factor is also introduced. In a second step, we will present generalities on the field of photovoltaic. In particular, we will recall the operating principle of a solar cell, then review the various existing technologies as well as the records for the conversion efficiency of solar energy into electricity for laboratory cells. Finally, we will show that halogenated perovskite materials have a strong potential for applications in other fields such as photodetection or light emission.

I.2 Perovskite materials

I.2.1 History and generality

Historically, exploration of minerals for metallurgy was intense during the XVIIIth and XIXth centuries in the Ural Mountains of Russia. This exploration led to the appearance of many local mines. In 1839, the perovskite $CaTiO_3$ was discovered in the Akhmatov mine by AB Kemmerer and the German mineralogist, Gustav Rose, who first described it and named it after the Russian mineralogist Lev Aleksevich von Perovski [1, 2].

Since then, the term perovskite has been used to describe all structures analogous to that of the compound $CaTiO_3$. These oxides, of general formula AMX_3 where A and M are cations and X an anion. The perovskite structure, is a three-dimensional (3D) grid of MX6 octahedra linked together by their vertices and forming cuboctahedral cavities which are occupied by the cation A. Depending on the nature of the anion X, we distinguishes several kinds of perovskites: oxides ($X = O^{2-}$), chalcogens ($X = S^{2-}$, Se^{2-}, Te^{2-}) and halogenated ($X = Cl^-$, Br^-, I^-). In addition, if cation A is an organic cation, the perovskites are referred to as hybrids (organic-inorganic).

I.2.2 Structure

The general formulas AMO_3 and AMX_3 refer to three-dimensional structures (see Figure I.1). Take the case of the compound CaTiO3: the octahedra of Ti-O share vertices and repeat in the three directions of space. In the cavities formed by these octahedra are found calcium cations.

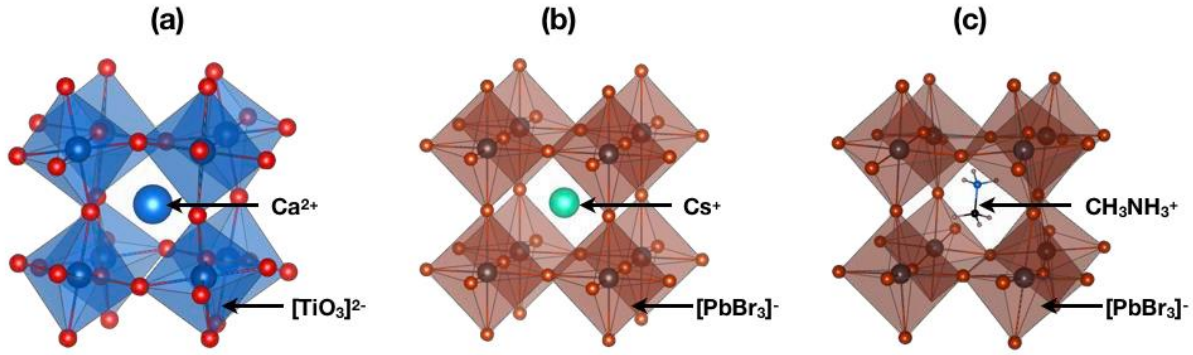

Figure I.1 Schematic representations of the crystal structures of the compound $CaTiO_3$ (a), of the halogenated perovskite $CsPbBr_3$ (b), of the hybrid halogenated perovskite $MAPbBr_3$ (c). The cation at site A is located in the cavity formed by the octahedra.

If the diversity of the structures characterized is indicative of a very rich chemistry, it is especially thanks to the cation occupying site A. Its chemical nature leads to other types of perovskites. So when the inorganic cation at site A is replaced by an organic cation, we are dealing with a hybrid halogenated perovskite (see Figure I.1). The term "hybrid" reflects the fact of finding both an organic part (cation at site A) and an inorganic part (MX6 octahedra) within the same structure. Many organic cations exist, methylammonium (MA = $CH3NH3^{+}$) remains the most common among hybrid halogenated perovskites. With this last cation, we can obtain 3D structures, such as $CsPbX_3$. The $CsPbX_3$ compound will be discussed in Chapters 4. The size of the organic cation can directly influence the stability of the perovskite structure. Figure I.2 shows different compounds ranging from zero-dimensional structure (0D) to three-dimensional structure (3D) 3– 5. In the two-dimensional (2D) structure, octahedra propagate only in both directions of space thus forming layers. The A cations are located on either side of these octahedra. These compounds are associated with the presence of large organic cations. In the one-dimensional structure (1D), we find chains of octahedra. Lastly, the isolated octahedra are found in the 0D structure.

Figure I.2.a shows A zero-dimensional structure: $(C_8N_2H_{18})_2PbI_6$. Inorganic clusters are surrounded by organic cations: 1,4-dimethyl-1,4-diazoniabicyclo [2.2.2] octane. Figure I.2.b shows the structure of the compound $(C_8N_2H_{11})PbI_3$ adopting a one-dimensional structure. The organic cation is Nphenylethanimidamidine. Figure I.2.c shows the structure of the compound $NH_3(CH_2)_4NH_3PbI_4$ in one dimension where the Pb-I octahedra share the vertices and form layers. The organic cation is 1,4-butanediammonium and Figure I.2.d shows the structure of the compound $CH_3NH_3PbI_3$ having a three-dimensional structure. The octahedra share the vertices. The organic cation is methylammonium.

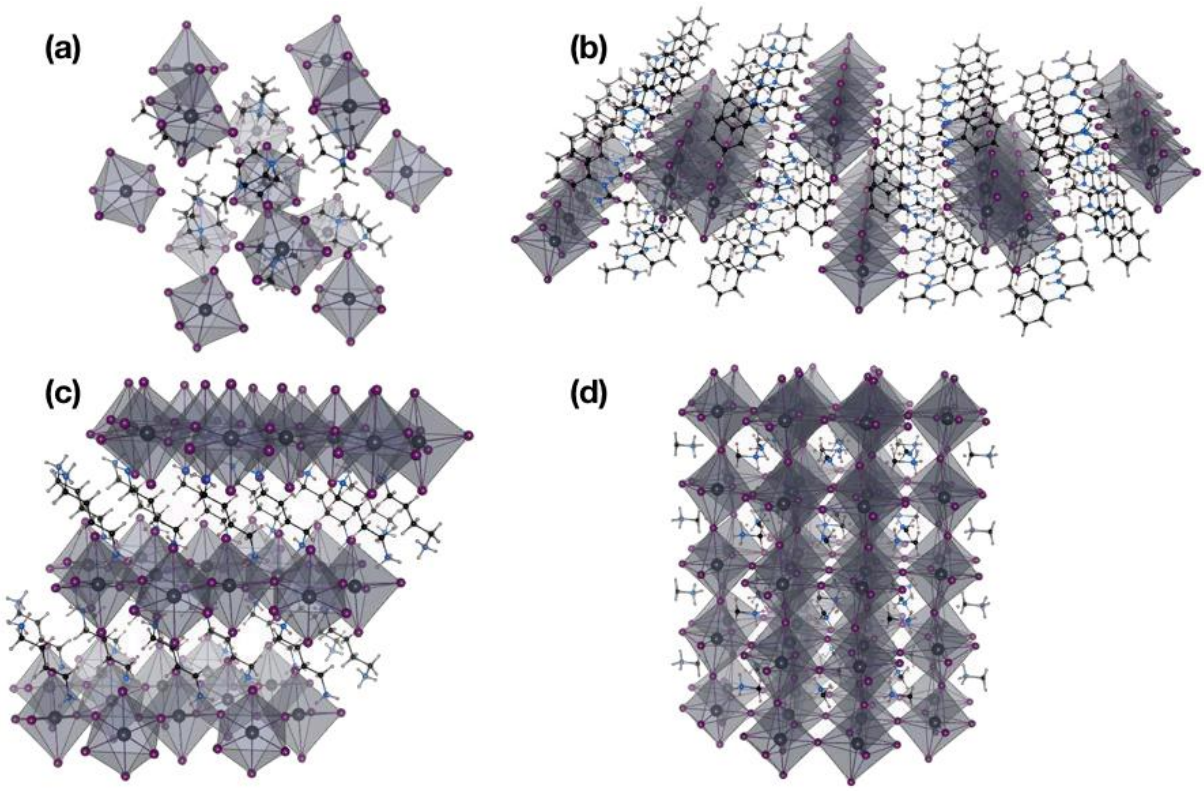

Figure I. 2 Schematic representation of halogenated hybrid perovskite.

I.3 Solar cell

I.3.1 A brief history of the solar cell

The photovoltaic effect was discovered in 1839 by the French physicist Edmond Becquerel. He observed that an electric current could be generated by AgCl between two platinum electrodes after exposure to light [3]. A few decades later, Adam and Day demonstrated for the first time the photovoltaic effect in selenium, a semiconductor compound [4]. Subsequently, in 1905, Albert Einstein published a theory explaining the photoelectric effect. The Nobel Prize in Physics was awarded to him in 1921 for work [5]. During the 1950s, the yields of solar cells continued to increase. In 1954, D. Chapin, C. Fuller and G, Pearsonthe developed the first silicon-based solar cell containing a p-n junction, reaching a yield of 6% [6]. That same year, the photovoltaic effect was also discovered for cadmium sulphide (CdS) crystals [7]. More recently, the first concrete application of solar cells has taken place in the aerospace field. The artificial Explorer 6 satellite launched in 1959 and the first Teslar 1 communication satellite launched in 1962 were equipped with silicon-based solar panels. At

that time, this technology was extremely expensive, and large-scale marketing was unthinkable. It was not until the oil crisis in the 1970s that the effort to find alternatives to fossil fuels was stepped up. Since then, the cost of photovoltaic technology has been constantly decreasing. In 1971, Alferov's group, Z. proposed the first group III-V semiconductor solar cell, with a cell based on gallium arsenide (GaAs) [8]. Seven years later, Hovel, H. J. and Woodall, J. M. produced a solar cell from GaAlAsGaAs reaching a yield of 20% [9]. The Carlson group, D.E., presented a yield of 2.4% on an amorphous silicon cell, thus launching the domain of thin-film solar cells [10]. The first monolithic tandem solar cell was produced by Lodowise et al. in 1982. This type of component makes it possible in principle to exceed the Shockley-Queisser limit (vacuum infra) defined for single cells [11]. In 1985, the yield reached 20% for simple silicon-based cells [12]. This technology is so far the standard and still dominates the market. The first low-cost organic solar cell was reported by Tang, CW in 1986 [13]. A few years later, the architecture of a photosensitive pigment solar cell (English designation: dye-sensitized based solar cell, DSSC) was proposed by O 'Regan, B. and Grätzel, M [14]. More recently (2009), Kojima et al. tested a DSSC solar cell in which the halogenated perovskite is the active layer [15]. These three types of solar cells are still in strong development and are promising for large-scale industrialization at low cost.

Photovoltaic technologies are classified in different categories; we have single-junction cell such as Silicon (crystalline cell) with an efficiency of 26.7 % [16], GaAs (thin film cell) 28.8% [17], CIGS (cell) 21.7% [18],perovskite (cell) 20.9% [19],Organic (cell) 11.2% [20] and Dye (cell) 11.9% [21]. We have multiple-junction cell such as 5 junction cell (bonded) 38.8% [22], InGaP/GaAs/InGaAs 37.9% [23], GaInP/GaAs/Si (mech. Stack) 35.9% [24] and GaInP/GaInAs/Ge; Si (spectral split minimodule) 34.5% [25]. We have also another categorie is concentrator cell which have a high efficiency such as GaInP/GaAs; GaInAsP/GaInAs 46.0% [26], InGaP/GaAs/InGaAs 44.4% [27], and Three junction (3j) 35.9% [28].

I.3.2 The state of the art in the photovoltaic field

The National Renewable Energy Laboratory (NREL) regularly updates a figure that shows the evolution of record efficiencies for the majority of technologies in the photovoltaic field (Figure I.3). We find solar cells based on silicon and III-V semiconductors (GaAs), thin-film cells. Some universities, research institutes and companies have a major contribution, for example NREL, EPFL (École Polytechnique Fédérale de Lausanne), Spectrolab (Boeing), Sharp, Soitec, Sanyo, etc. This figure can be divided into three parts according to the photovoltaic efficiencies. In the middle of the figure are the “classic”, monojunction, silicon-

based, GaAs solar cells as well as thin-film cells. These give efficiencies ranging from 21% to 27%. At the top of this figure are the multi-junction solar cells. The efficiencies reach 47.1% but these cells have significant manufacturing costs. At the bottom of this figure are organic and photosensitive pigment solar cells (DSSCs) as well as cells based on halogenated perovskites. It should be noted that the first two technologies achieve an efficiency of 11-13% while for that based on halogenated perovskites achieve an efficiency of around 25.5%.

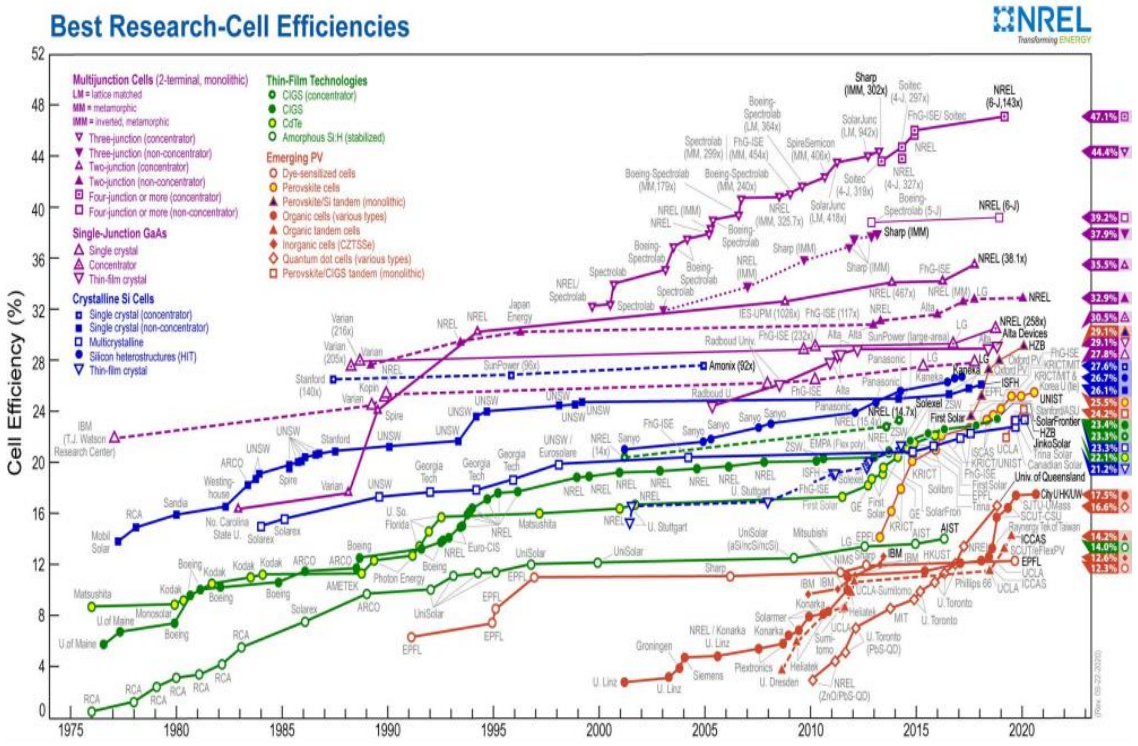

Figure I.3 Performance records for various technologies over time. (source: https://www.nrel.gov/pv/assets/images/efficiency-chart.png)

I.3.3 Operation of a solar cell with selective contacts

A solar cell is the process of transforming solar energy into electricity. In order to achieve this goal, semiconductors inherently having a bandgap (gap) are used to absorb light. In general, we can summarize the mechanism of operation in several steps: absorption of the photon, separation of charges, transport of charges and collection of charges (Figure I.4). In the case of perovskite cells, these latter stages are possible thanks to the presence of selective contacts.

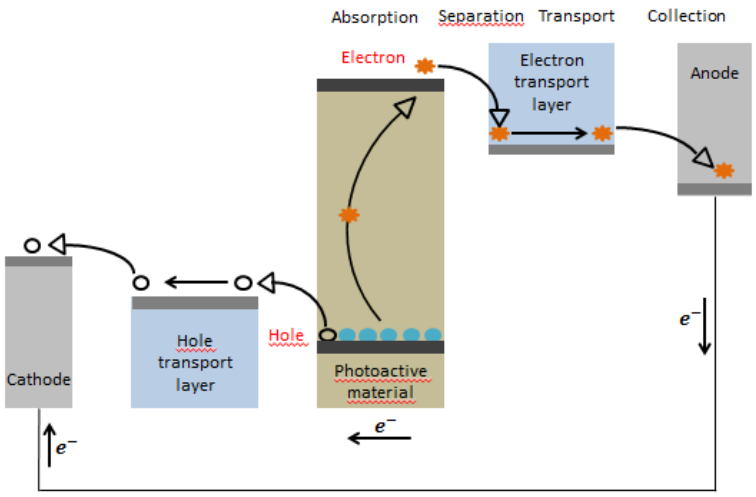

Figure I.4 Schematic representation of the operation of a solar cell with selective contacts for electrons and holes.

- ***Photon absorption***

The sun emits light at different frequencies in the form of particles called photons. The energy of the photon (E_{photon}) depends on its wavelength λ:

$$E_{photon} = hv = \frac{hc}{\lambda} \quad \text{(I.1)}$$

In this equation, *h* is Planck's constant, c the speed of light in a vacuum and λ the frequency.

Two factors determine the absorption by the material. The first factor is the width of the forbidden band (energy of the electronic gap) of the semiconductor (E_{gap}). We can have three different situations:

(1) If $E_{photon} < E_{gap}$, the photon is not absorbed.
(2) If $E_{photon} = E_{gap}$, the photon is absorbed by the semiconductor.
(3) If $E_{photon} > E_{gap}$, the photon is absorbed by the semiconductor but the relaxation in the bands towards the electronic states near the gap causes a loss of energy.

The absorption of the photon also depends on the absorption coefficient of the semiconductor. It's a function of the wavelength of the incident photon and determines the thickness required for optimum absorbance. For example, the silicon-based material is known to be a bad absorber, because its gap is indirect [29]. As a result, the thickness of the silicon must be in the range of several hundred micrometers in order to ensure optimum absorbance. Unlike organic materials where less than a hundred nanometers may be sufficient [30]. When both

conditions are satisfied, the photons efficiently excite electrons from the valence band (valence band, VB) to the conduction band (conduction band, CB).

This phenomenon has two consequences. On the one hand, the promoted electrons bring negative charges into the CB and leave positively charged "holes" in the VB. On the other hand, due to the Coulomb interaction, these two charges can be linked. A bonded electron-hole pair is also called an exciton. Note that the energy of the exciton bond depends on the dielectric constant of the material.

- ***Separation of charges***

Due to the exciton interaction, it may be more difficult to effectively separate the charges produced.

In the case of crystalline silicon, the excited electrons and the holes can be considered as free charges because the Coulomb interaction between the charges is very weak [31]. In contrast, for organic semiconductors, which exhibit a low dielectric constant, the binding energy of the excitons can reach 300-500 meV. These values are higher than thermal energy at 25 ° C (25.7 meV) and lead to localization of charges and poor collection [32]. In order to overcome this problem of charge separation in organic materials, several strategies exist. For example, in solar cells with bulk heterojunctions (BHJ), charge separation is achieved through charge transfer between a donor material and an acceptor material. Another important aspect concerns the driving force behind the separation of charges. This matrix force can be created by an electric field or by an electron density gradient. In a silicon-based solar cell, separation is achieved through a p-n junction which creates a depletion zone. In the case of organic cells but also based on perovskites, it is the difference in work functions at the interfaces between contact materials that constitutes the driving force.

- ***Charge transport and charge collection***

After separation of the charges, the electrons and the holes must be transported and collected at the electrodes. Electrons (holes) are transported to the anode (cathode) where they are collected. For DSSC solar cells, the charges generated by the pigment are transported to the electrodes using an oxide on the n side and an electrolyte on the p side. For best function, photoactive materials must be good semiconductors with long charge carrier lifetimes. It should be noted that during transport, the charge carriers may or may not recombine radiatively. This latter phenomenon is generally characterized by a diffusion length, ie the average distance traveled by a charge carrier before recombination.

I.3.4 Characterization of a solar cell

The most common way to characterize a solar cell is to measure the current-voltage curve (J-V curve) under standard radiation. This can be achieved by applying an electric voltage V to the two electrodes of a cell by measuring the current I. The current density J is preferred over the electric current I, as this allows a direct comparison between different types of solar cells with different contact surfaces.

In the dark, an ideal solar cell behaves like a diode and its characteristic J (V) satisfies equation [33]:

$$J = J_0 \left[e^{\left(\frac{qv}{\eta kT}\right)} - 1 \right] \qquad \text{(I.2)}$$

Where J_0 is the saturated current density, η the ideality factor (η = 1 for an ideal diode), k the Boltzmann constant, q the elementary charge and T the temperature. When a solar cell is illuminated, the *J-V* curve of the diode shifts downward (Figure I.5), this is due to the photo-current generated by the solar cell itself [34].

The *J-V* curve of a cell under illumination has several important parameters: short-circuit current density (J_{sc}), open-circuit voltage (V_{oc}), and fill-factor (FF).

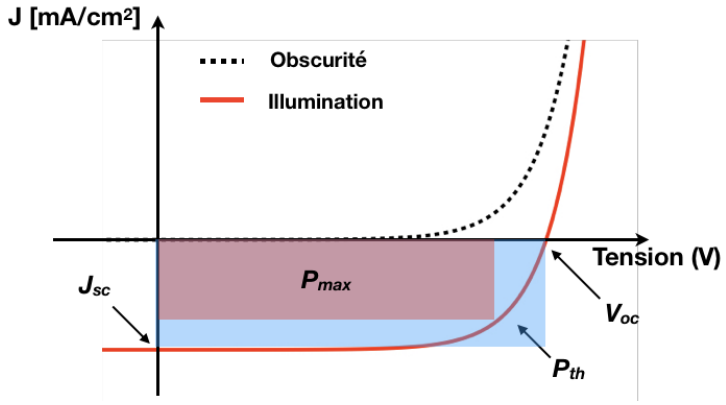

Figure I.5 The schematic representation of the J-V curves under conditions of darkness and illumination. The red rectangle represents the maximum output power of a cell. The blue rectangle refers to the maximum output power produced by an ideal cell (Pth). The area ratio of the two rectangles gives the fill-factor (FF).

More precisely, V_{oc} is the voltage measured between the two contacts of an open circuit cell; J_{sc} is the current density between two contacts of a shorted cell. Finally, FF is given by the following relation:

$$FF = \frac{P_{max}}{P_{th}} = \frac{P_{max}}{V_{oc} \cdot J_{sc}} \qquad \text{(I.3)}$$

P_{max} is the maximum output power that a solar cell can give in real conditions. P_{th} is the maximum output power given by an ideal solar cell. The efficiency of a solar cell is defined by the ratio P_{max} and the incident power P_{in}:

$$Eff = \frac{P_{max}}{P_{in}} = \frac{FF.V_{oc}.J_{sc}}{P_{in}} \quad \text{(I.4)}$$

It is noted that other factors can influence on the efficiency such as the energy of the gap, the intensity of the incident light as well as the temperature. For this reason, the measurement conditions are standardized so that the performance of various solar cells can be compared.

I.3.5 Cellules photovoltaïques avec absorbeur pérovskite

The potential of hybrid halogenated perovskites was revealed in 2009 when they were first used as an absorber in photovoltaic cells. Kojima and al. integrated the 3D perovskite $CH_3NH_3PbI_3$ to Dye-Sensitized solar cells with a liquid electrolyte, thus demonstrating a photovoltaic conversion efficiency of 3.8% [35]. In 2012, a major breakthrough was made by replacing the liquid electrolyte with a solid electrolyte, which achieved a conversion efficiency of 9% [36-37]. Following this work, photovoltaic cells with the hybrid perovskite absorber $CH_3NH_3PbI_3$, more commonly known as perovskite cells, have aroused unprecedented enthusiasm in the scientific community. The evolution of cell architecture and perovskite absorber manufacturing processes and devices have contributed to a meteoric rise in perovskite cell performance to reach 25.5% in 2020, rivaling other photovoltaic technologies such as silicon-based cells or thin film technologies (Figure I.3).

I.4 Other applications

While materials based on halogenated perovskites show potential in the photovoltaic field, more and more research work indicates that these materials could also be used for other applications such as light emitting diodes (LEDs). , lasers, photodetection, bio-medical imaging [38–48].

- ***Light Emitting Diode (LED)***

The first LEDs based on halogenated perovskites were presented in the 90s. The active materials were lamellar structures [49,50]. However, more recently, materials based on 3D halogenated perovskites in colloidal structures (nanocrystals, quantum dots, etc.) have shown a higher potential. The gap of these materials is tunable. It is therefore possible to produce

multicolored LEDs [38,51–55]. Among these materials, the compound $CH_3NH_3PbBr_3$ and the brominated compounds in general exhibit particularly advantageous optical properties. Kim and al. studied in 2014, an LED based on this material, with a high luminance of 417 $cd.m^{-2}$ at room temperature [52].

Thanks to simple architectures and manufacturing processes, components based on technologies close to OLEDs (organic diodes) are promising [56,57]. In 2015, Ayguler et al. succeeded in having a cell based on FAPbBr3 nanoparticles with a stable luminance of 1-2 $cd.m^{-2}$ [58].

- ***Laser***

Kondo and al. observed in 1998, for the first time, a laser effect in perovskite materials. They observed a bi-excitonic laser emission on the lamellar compound of perovskite $(C_6H_{13}NH_3)_2PbI_4$ at a temperature of 16 Kelvin and under optical pumping [59]. Twenty years later, Zhu and al. have produced nanotubes based on three-dimensional perovskites [60]. These nanotubes have a tunable emission wavelength at room temperature.

- ***Photodetectors***

In 2014, Dou and al. studied a photodetector based on the compound $CH_3NH_3PbI_{3-x}Cl_x$ [61]. That shows a high detectivity (10^{14} Jones). In 2015, Yakunin and al. used the compound $CH_3NH_3PbI_3$ for the detection of X-ray [62]. In 2016, Fang and al. have shown that the $CH_3NH_3PbBr_3$ compound can also be used for X-ray detection, and is four times more sensitive than the detector based on α-Se [63,64].

- ***Field Effect Transistors (FET)***

Mitzi and al. introduced field-effect transistors at the end of the 90s [50, 65]. And in 2015, the compound $CH_3NH_3PbI_3$ also showed potential for this application [66].

Chapter II

Ab initio approach

II.1 Density Functional Theory (DFT)

II.1.1 Theoretical foundations

Ab initio methods seek to predict the properties of materials, by solving quantum mechanical equations, without using adjustable variables. Among the ab initio methods, the density functional theory (DFT) is a reformulation of the N-body quantum problem into a problem dealing only with electron density. Today, DFT constitutes one of the most widely used methods for quantum calculations of the electronic structure of the solid, because the reduction of the problem that it brings makes it possible to make accessible to the calculation the ground state of a system comprising a large number of electrons. It is therefore a method of choice for studying the physical properties of the ground state of solids. We have used in this manuscript for the equations of quantum mechanics the atomic units, that is, $\hbar = 1$, $e^2 = 1$ and $m_e = 1$, which gives energies in Hartree.

We place ourselves within the framework of the Born-Oppenheimer approximation where the degrees of freedom of nuclei and electrons are decoupled due to the very large difference in mass. The electrons therefore react instantaneously to changes in the positions of the ions and we can then solve the equations concerning the electrons by considering that the position of the nuclei is fixed. To determine the ground state of Ne electrons, we must calculate the eigen energies and eigenfunctions of the Hamiltonian with many bodies:

$$H = \sum_{i=1}^{N_e} -\frac{1}{2}\nabla_{ri}^2 - \sum_{i=1}^{N_e}\sum_{\alpha}\frac{Z_\alpha}{\|r_i - r_\alpha\|} + \sum_{j<i}^{N_e}\frac{1}{\|r_i - r_j\|} \qquad \text{(II.1)}$$

Where the indices i and j traverse all electrons and the index α traverse all nuclei. We call V the external potential for the N_e electrons and *v* the external potential for an electron.

$$V\left(r_1, \dots, r_{N_e}\right) = \sum_{i=1}^{N_e} v(r_i) = \sum_{i=1}^{N_e}\sum_{\alpha}\frac{Z_\alpha}{\|r_i - r_\alpha\|} \qquad \text{(II.2)}$$

We must therefore solve the eigenvalue equation:

$$H\left(\mathrm{X}_1, \mathrm{X}_2, \dots, \mathrm{X}_{N_e}\right)\psi(\mathrm{X}_1, \mathrm{X}_2, \dots, \mathrm{X}_{N_e}) = E\psi(\mathrm{X}_1, \mathrm{X}_2, \dots, \mathrm{X}_{N_e}) \qquad \text{(II.3)}$$

Where the variables X_i denote both the space variables r_i, and the spin variables s_i.

Since the number N_e of electrons for a solid is of the order of the number of Avogadro Na ~10^{23}, the problem must be simplified before it can be solved. For this, we try to replace the unknown of the problem ψ (X_1, X_2,..., X_{Ne}), by the variable ρ (x) which is the electron density defined by:

$$\rho(X) = N_e \sum_{s_i \neq s_1} \int dr_2 \dots \int dr_{N_e} \psi^*(\mathrm{X}_1, \mathrm{X}_2, \dots, \mathrm{X}_{N_e}) \psi(\mathrm{X}_1, \mathrm{X}_2, \dots, \mathrm{X}_{N_e}) \qquad \text{(II.4)}$$

The integration is done on all the space variables except one and on all the spin variables. It may seem impossible at first glance to condense the information so much, since we have gone from a 3Ne variable unknown to a 3 variable unknown (if we neglect the spin). However, the first theorem of Hohenberg and Kohn [67] authorizes this substitution in a rigorous way. The second theorem of Hohenberg and Kohn also allows us to state that the solution of these equations can be replaced by the search for the minimum of the energy.

II.1.2 Kohn and Sham's approach

We are now able to determine the density and all the properties of the ground state of any system by a simple search for the minimum of the energy, where the energy is considered as a functional of ρ. It is written in the form:

$$E[\rho] = F[\rho] + \int \rho(r) v(r) d^3r \qquad \text{(II.5)}$$

Where v is the external potential defined by (1.2) and F [ρ] is a universal function not dependent on the system.

Unfortunately we do not know the expression of the functional F [ρ]. We must therefore find an approximation of F [ρ] which explains the expression to be minimized. We can decompose F [ρ] in the form:

$$F[\rho] = T[\rho] + W[\rho] \qquad \text{(II.6)}$$

Where T is kinetic energy and W is the electronic interaction term. W [ρ] can itself be written as a Hartree term representing the classical electrostatic energy of a charge density ρ, plus quantum terms E_{xc}:

$$W[\rho] = \frac{1}{2} \iint \frac{\rho(r_1) \rho r_2}{|r_1 - r_2|} dr_1 dr_2 + E_{xc}[\rho] \qquad \text{(II.7)}$$

It then remains to determine the kinetic term T [ρ] and the terms of trade and correlation Exc. An approach was proposed by W. Kohn and L. Sham [68] in 1965 to solve this problem by going through an auxiliary problem of electrons which do not interact with each other. This gives us the functional form of T and replaces *v* by an effective potential:

$$H_s = T_s + V_s = \sum_{i=1}^{N_e} \left(-\frac{1}{2}\nabla_i^2 + v_s(r_i) \right) \quad \text{(II.8)}$$

Where H_s is the Hamiltonian of N_e not interacting electrons. Then there exists a functional $E_s[\rho] = T_s[\rho] + \int v_s(r)\rho(r)d^3r$ whose minimization gives the exact density of the ground state ρ_s. Ts [ρ] is also a universal functional, which represents the kinetic energy of a system of non-interacting electrons. In this case we can always write the wave function in the form:

$$\psi_s = \frac{1}{\sqrt{N_e!}} \det[\phi_1, \phi_2, \dots, \phi_{N_e}] \quad \text{(II.9)}$$

Where the ϕ_i are monoelectronic wave functions.

Kinetic energy then takes the simple form:

$$T_s = \sum_i f_i \langle \phi_i | -\frac{1}{2}\nabla_i^2 | \phi_i \rangle \quad \text{(II.10}$$

Where f_i is the occupancy number of the orbital ϕ_i between 0 and 1. The density is in the form:

$$\rho_s(r) = \sum_i f_i |\phi_i(r)|^2 \quad \text{(II.11)}$$

The corresponding total energy is an explicit functional of the orbitals ϕ_i and is written:

$$E_s[\{\phi_i, f_i\}] = -\frac{1}{2}\sum_i \int f_i \phi_i^*(r)\nabla^{2\phi_i}(r)dr + \sum_i \int f_i |\phi_i(r)|^2 v_s(r)dr \quad \text{(II.12)}$$

To find the equations governing the ϕ_i, we must minimize $E_s[\{\phi_i, f_i\}]$ under the constraint that the orbitals are orthonormal:

$$\int \phi_i^*(r)\phi_j(r)dr = \delta_{ij} \quad \text{(II.13)}$$

We must therefore minimize the generalized Lagrangian:

$$\Omega\left[\{\phi_i, f_i\}, \{\lambda_{ij}\}\right] = E_s[\{\phi_i, f_i\}] - \sum_{ij} \lambda_{ij} \left(\int \phi_i^*(r)\phi_j(r)dr - \delta_{ij} \right) \quad \text{(II.13)}$$

And find the Lagrange multipliers λ_{ij} which ensure the orthonormality. δ_{ij} is the symbol of Kronecker.

We see that inverting i and j in the expression of the constraint amounts to evaluating its conjugate complex. Since the constraint is real, the constraint or its conjugate must give the same solution to the minimum of the functional. We therefore have $\lambda^*_{ji} = \lambda_{ij}$. As the solution matrix (λ_{ij}) is a Hermitian matrix of dimension N_e, we can diagonalize it. The eigenvalues εi are real and the transition matrix (U_{ij}) is unitary. We call ε the diagonal matrix, whose diagonal elements are the εi, then:

$$(\lambda) = ({}^tU^*)(\varepsilon)(U) \quad \text{(II.14)}$$

We can define a unit transformation on the set $\{\phi_i\}$ as follows:

let the vector depending on r,

$$(\phi(r)) = (\phi_1(r), \phi_2(r), \dots, \phi_{N_e}(r)) \quad \text{(II.15)}$$

We can apply the matrix U to it. This gives us a vector dependent on r, (ψ) = (ψ_1 (r), ψ_2 (r),..., Ψ_{Ne} (r)). More formally:

$$\psi_i(r) = \sum_k U_{ik}\phi_k(r) \quad \text{(II.16)}$$

Let us look at the effect of a unit transformation TU on the density ρ:

$$TU\rho(r) = \sum_i \psi_i(r)\psi_i^*(r) = \sum_{ikl} U_{ik}U_{il}^*\phi_k(r)\phi_l^*(r) \quad \text{(II.17)}$$

Since U is unitary, its inverse is equal to its deputy:

$$\sum_i U_{ki}^{-1}U_{il} = \sum_i U_{ik}^*U_{il} = \delta_{kl} \quad \text{(II.18)}$$

So

(II.19)

$$TU\rho(r) = \sum_{kl} \delta_{kl}\phi_k(r)\phi_l^*(r) = \sum_k \phi_k(r)\phi_k^*(r) = \rho(r)$$

Any unit transformation therefore leaves ρ invariant. We can prove in the same way that T_s is invariant. The functional E [{ϕ_i, f_i}] is therefore invariant by unit transformation.

The ground state must minimize the generalized Lagrangian:

$$\frac{\delta\Omega}{\delta\phi_i} = \left(\frac{\delta\Omega}{\delta\phi_i^*}\right)^* = 0 \qquad \text{(II.20)}$$

$$\frac{\delta\Omega}{\delta\lambda_{ij}} = 0 \qquad \text{(II.21)}$$

This gives us:

$$-\frac{1}{2}\nabla^2\phi_i(r) + v_s(r)\phi_i(r) = h_s\phi_i(r) = \sum_j \lambda_{ij}\phi_j(r) \qquad \text{(II.22)}$$

$$\int \phi_i^*(r)\phi_j(r)dr = \delta_{ij} \qquad \text{(II.23)}$$

either in matrix notation

$$(h_s\phi) = (\lambda)(\phi) \quad , \quad (h_s\phi) = ({}^tU^*)(\varepsilon)(U)(\phi) \qquad \text{(II.24)}$$

If we apply (U) to the left:

$$(U)(h_s\phi) = (\varepsilon)(U)(\phi) \qquad \text{(II.25)}$$

However, h_s does not depend on the index of orbital i, and h_s is a linear operator. It is therefore irrelevant to apply the operator h_s before or after the unit transformation:

$$(h_s\psi) = (\varepsilon)(\psi) \qquad \text{(II.26)}$$

We have therefore transformed our problem (II.21) and (II.22) into an eigenvalue problem where the ε_i are the eigenvalues and $\psi_i = ((U)(\phi))_i$ are the eigenvectors.

Let us now return to the problem of interacting electrons: the central hypothesis of Kohn and Sham is that for any interacting system, we can find a potential v_s such that the exact density of the system ρ (r) is equal to ρ_s (r), the density of the independent electron system. We have

(II.27)

therefore replaced a problem of interacting electrons with a simpler fictitious problem where the electrons do not interact, but evolve in an effective potential. A system accepting this type of representation is said to be v-non-interacting-representable [69]. v_s is called effective potential. To calculate the latter, we rewrite the total energy of the system in the form:

$$E[\rho] = T_s[\rho] + \frac{1}{2}\iint \frac{\rho(r_1)\rho(r_2)}{|r_1 - r_2|} dr_1 dr_2 + \int \rho(r) v(r) d^3r + E_{xc}[\rho]$$

Here E_{xc} changes definition with respect to equation (II.7) since:

$$E_{xc} \Rightarrow E_{xc} + T - T_s \tag{II.28}$$

It therefore contains a part of the kinetic energy that is not in T_s [ρ].

To find v_s, we write that ρ must minimize the 2 functional E_s [ρ] and E [ρ]. The equation on the derivative of E [ρ] and E_s [ρ] with respect to ρ then gives us:

$$v_s(r) = v_{ext}(r) + \int \frac{\rho(r')}{|r - r'|} dr' + v_{xc}[\rho](r) \tag{II.29}$$

v_{xc}[ρ](r) denotes the exchange and correlation potential and $v_{Hartree}$ the potential of Hartree.

$$v_{xc}[\rho](r) = \frac{\delta E_{xc}[\rho]}{\delta \rho} \tag{II.30}$$

$$v_{Hartree} = \int \frac{\rho(r')}{|r - r'|} dr' \tag{II.31}$$

We have limited ourselves here to the *v*-non-interacting-representable system. In the same way as for the theorem of Hohenberg and Kohn, we can extend the definition of T_s over a less limited set and show that the approach of Kohn and Sham is still valid as long as the ground state is non-degenerate.

In summary, to solve the Kohn and Sham equations, we start from an initial density ρ (r), from which we calculate the effective potential using equation (II.30). We then solve the eigenvalue problem (II.27), which gives us the ψ_i from which we can calculate ρ. This is done by successive iterations until the density no longer changes from one iteration to another.

II.2 Functional exchange and correlation

To be able to do the math we now need an approximation for the term of exchange and correlation, which is the last term for which we do not know an expression in terms of density or orbitals. The search for precise approximations for the exchange and correlation is still relevant and we present here only the standard functionals, which have already been widely used.

II.2.1 Local Density Approximation (LDA)

The most popular approximation for calculating the exchange and correlation term is the Local Density Approximation, or LDA. This approximation assumes that the density fluctuates quite slowly. It therefore replaces the potential for exchange and correlation at each point in space with that of a uniform gas of interacting electrons. The electron gas is taken as the same density as the density at the calculated point. This makes it possible to give an exact expression by interpolating Monte-Carlo calculations. This was done in the early 1980s [70]. The LDA is often an effective approximation, even when the density fluctuates significantly. However, it has some disadvantages, such as a systematic underestimation of the cohesive energy of solids and lattice parameters [71,72]. The error in the structural parameters is often small (in the order of 1 to 2%), but can become large when Van der Vaals type bonds are involved.

This approximation is the basis of all modern exchange-correlation functionalities and can be defined as follows:

$$\begin{cases} E_{xc}^{LDA}[\rho] = \int \rho(r)\,\varepsilon_{xc}\left(\rho(r)\right)dr \\ E_{xc}^{LDA}\left[\rho_\alpha, \rho_\beta\right] = \int \rho(r)\,\varepsilon_{xc}\left(\rho_\alpha(r), \rho_\beta(r)\right)dr \end{cases} \tag{II.32}$$

It is the functional for which an exact form is almost known. The approximation of $E_{xc}[\rho]$ is based on the uniform electron gas model where the term $\varepsilon_{xc}\left(\rho(r)\right)$ is the exchange-correlation energy by particle of uniform electron gas of density $\rho(r)$. Moreover, $\varepsilon_{xc}\left(\rho(r)\right)$ can be considered as the sum of an exchange contribution and correlation:

$$\varepsilon_{xc}\left(\rho(r)\right) = \varepsilon_x\left(\rho(r)\right) + \varepsilon_c\left(\rho(r)\right) \tag{II.33}$$

The exchange term, commonly called "Dirac exchange" [73] (symbolized by S because that this expression was taken up by Slater) is known exactly:

$$\varepsilon_x^s\left(\rho(r)\right) = -\frac{3}{4}\left(\frac{3\rho(r)}{\pi}\right)^{1/3} \tag{II.34}$$

The correlation part $\varepsilon_c\left(\rho(r)\right)$ cannot be expressed exactly. The approximation of this term established by Vosko, Wilk and Nussair (VWN) [74] has been most successful. She is based on an interpolation of the results of very precise quantum Monte-Carlo calculations on the uniform electron gas made by Ceperley and Alder [75].

The basic idea of the LDA is that it is possible to estimate the exchange-correlation energy of an inhomogeneous system using on infinitesimal portions the results of an homogeneous electron gas density equal to the local density of the inhomogeneous system. This approximation is reasonable for a system where the density varies slowly but this condition is not met in practice. However, LDA is surprisingly effective and its application to atoms and molecules is justified by the success of its digital applications.

II.2.2 Approximation of the generalized gradient (GGA)

The most natural way to improve the LDA is to account for the inhomogeneity of the electron density by introducing into the exchange energy and correlation terms depending on the density gradient. The GGA (generalized gradient approximation) [76] allows the introduction of a combination between local terms and gradient-dependent terms. It gives good results and makes it possible to improve the cohesion energies and the mesh parameters. However, improvement over LDA is not always systematic as GGA sometimes overcorrects LDA [77,78]. This is why in the results part of this thesis we systematically compared the relative stabilities of the phases as well as the elastic constants obtained in GGA and in LDA.

At first, LDA was treated as the first term in a Taylor series development:

$$E_{xc}^{GEA}[\rho] = \int \varepsilon_{xc}^{GEA}\left(\rho(r)\right)\rho(r)\,dr + \int C_{xc}\left(\rho(r)\right)\frac{\left|\nabla\rho(r)\right|}{\rho^{4/3}(r)}\,dr + \ldots \tag{II.35}$$

This functional form is the gradient approximation (GEA or Gradient Expansion Approximation). Unfortunately, this gives worse results than the LDA. Indeed, the exchange-correlation hole does not satisfy the conditions which ensured LDA some physical sense. In

(II.36)

order to correct these problems, the above functional has been modified to force it to comply with the main boundary conditions. We then get the generalized gradient approximation (GGA) behind the success of the DFT:

$$E_{xc}^{GGA}[\rho;\nabla\rho]=\int \varepsilon_{xc}^{GGA}\left(\rho(r),\nabla\rho(r)\right)dr$$

Often the contributions for exchange and correlation are developed separately:

$$E_{xc}^{GGA}(\rho,\nabla\rho)=E_{x}^{GGA}(\rho,\nabla\rho)+E_{c}^{GGA}(\rho,\nabla\rho) \quad \text{(II.37)}$$

The major problem of the LDA coming from the exchange, a very particular attention was focus on the development of this part:

$$E_{x}^{GGA}(\rho,\nabla\rho)=E_{x}^{LDA}-\int F\left(s(r)\right)\rho^{4/3}(r)dr \quad \text{(II.38)}$$

Where F is a function of the reduced gradient density (dimensionless):

$$s(r)=\frac{\left|\vec{\nabla}\rho(r)\right|}{\rho^{4/3}(r)} \quad \text{(II.39)}$$

We can thus cite the functions of Becke (B88) [79], that of Perdew (PW86) [80] and that of Handy and Cohen (OPTX) [81].

- **B88**

The B88 exchange functional is based on a dimensional analysis and on a correct asymptotic behavior of the exchange energy density:

$$F^{B88}(s)=\frac{\beta s^{2}}{1+6\beta s\times\sinh^{-1}(s)} \text{ avec } \beta\text{=0.0042 u.a} \quad \text{(II.40)}$$

β is an empirical parameter determined by a least squares analysis of the exchange energies of the six gas rare atoms (from He to Rn). The functional of Perdew and Wang (PW91) [82] comes from a modification of this functional to meet certain scaling conditions.

- **PW86**

This functional is based on an analysis of the expansion of the hole correlation exchange gradient around its LSDA form.

$$F^{PW86}(s)=\left[1+1.296\left(\frac{s}{p}\right)^{2}+14\left(\frac{s}{p}\right)^{4}+0.2\left(\frac{s}{p}\right)^{6}\right]^{1/15} \quad \text{avec p=}\left(24\pi^{2}\right)^{1/3} \qquad \text{(II.41)}$$

The functional of Perdew, Burke and Ernzerhof (PBE) [83] is a modification of this functional. It is interesting to note that neither PW86 nor PBE contain empirical parameters.

- **OPTX**

This functional is an improvement of the exchange functional of Becke [84] in which the authors have not only optimized the enhancement factor F but also the Dirac exchange coefficient in the LDA part obtaining so:

$$E_{xc}^{GGA}(\rho,\nabla\rho)=1.051\times E_{x}^{LDA}-\int F^{OPTX}\left(s(r)\right)\rho^{4/3}(r)\,dr \qquad \text{(II.42)}$$

$$With:\ \mathrm{F}^{\mathrm{OPTX}}(s)=1.43169\left(\frac{\gamma s^{2}}{1+\gamma s^{2}}\right)^{2} \text{ with } \gamma=0.006 \qquad \text{(II.43)}$$

The three coefficients were obtained by reproducing the Hartree-Fock energy of the fundamental state of the first 18 atoms (H-Ar).

- **The correlation functionals**

Corrections to the correlation term are much more complex to formulate than those regarding the term of exchange. In addition, even if their influence on the structural and electronic properties of the systems studied is much less significant than that of the exchange, the fact remains that their taking into account turns out to be absolutely essential for obtaining quantitatively satisfactory results.

So the analytical expression of these corrections, particularly complicated, does nothing to help a better understanding of the physical principles on which they are based and cannot be understood using simple physical reasoning. These are mostly expressions satisfying known mathematical properties. We can cite, among others, the functional of Lee, Wang and Parr (LYP) [85], of Perdew (P86, counterpart of the functional exchange of PW86) [80] and that of Perdew and Wang (PW91) [82]. The exchange-correlation functional GGA represents a very significant improvement LDA, the main reason being the modification of the exchange part.

- **The functional meta-GGA**

In order to further improve the performance of GGAs, the exchange correlation functional meta-GGA (mGGA) consider the kinetic energy density of Kohn-Sham orbitals:

$$\tau = \frac{1}{2}\sum_{i}^{occ}\left|\nabla\Psi_i\right|^2 \tag{II.43}$$

In addition to the dependence on the density gradient already included in the GGAs.

The term of exchange E_x^{mGGA} can be written:

$$E_x^{mGGA} = -\frac{3}{4}\left(\frac{3}{4}\right)^{1/3}\int f\left(\rho,\nabla\rho,\tau\right)\rho^{4/3}\left(r\right)dr \tag{II.44}$$

The dependence of the exchange term on the Laplacian density greatly improves the accuracy of these functional. However, the dependence on the kinetic energy density poses implementation problems of these functionalities in a self-consistent scheme for the exchange-correlation potential, making the SCF procedure more time-consuming.

On the other hand, physical precision has not yet been achieved and the main part to improving is the exchange. The question is therefore: why use an exchange functional approximate when we know how to calculate the exchange exactly?

II.2.3 The hybrids Functional

When they proposed their approach in 1965, Kohn and Sham had already mentioned the interest of an exact processing of the exchange. They had already established an expression formal of the exchange-correlation energy based on the Hartree-Fock approximation for the exchange, the correlation term remaining unchanged from the LDA. They had also noted that the effective potential would have, through the use of this hybrid functional, a correct asymptotic behavior (in 1/r) far from the atom.

In the overwhelming majority of cases, the GGAs achieved better accuracy. The reason for this failure is the artificiality of the separation of exchange correlation terms: by combining a non-local exchange hole (Hartree-Fock) with a local correlation (LDA). Becke therefore chose to use the exact exchange differently by including only a part of it in the energy of exchange-correlation [86]. He proposed an expression to three parameters which will be designated by [87]:

(II.45)

$$E_{xc} = E_{xc}^{LDA} + a_0\left(E_x^{axact} - E_x^{LDA}\right) + a_x\Delta E_x^{B88} + a_c\Delta E_c^{PW91}$$

Where the a_0, ax and ac coefficients are determined semi-empirically by fitting to experimental data. E_{xc}^{exact} here represents the exact exchange energy obtained from Hartree-Fock calculation. In the first corrective term, the value of the a_0 coefficient can be linked to the "independent particles" character of the system. The following two terms allow to optimize gradient corrections, for the exchange and for the correlation. As such, the above equation represents the simplest way to take into account the exact exchange and find the limit of uniform electron gas. Because of this approximation, the accuracy of the energies is even better than when we use generalized gradient corrections.

A variation of this approach, calling the Lee's approximation, Yang and Parr (LYP) and Perdew and Wang [88], known as B3LYP, which is the most popular.

$$E_{xc}^{B3LYP} = a_0E_x^{LDA} + (1-a_0)E_x^{exact} + a_1\Delta E_x^{B88} + E_c^{LDA} + a_2\left(E_c^{LYP} + E_c^{LDA}\right) \quad \text{(II.46)}$$

Where a_0= 0.80, a_1= 0.72 and a_2= 0.81. The a_0, a_1 and a_2 parameters are semi-empirical quantities. This functional gives remarkably precise results for a large number of systems [89]. It has also been shown that she permits, unlike GGA, to correctly describe the magnetic properties of molecular compounds of transition metals and ligands. However, it is far from putting an end to the exchange and correlation problems in DFT [90, 91]. A number of avenues are currently being explored in order to get the most out of benefits of the exact exchange. On the one hand, Becke has built new functionalities taking into account both the exchange and the correlation. According to him, the functional based on GGAs and incorporating a fixed proportion of exact exchange has reached a limit.

Chapter III

Theoretical calculations of Oxide Perovskites ABO_3

III.1 Introduction

In the third chapter of this thesis, we present a theoretical investigation of electronic, structural, transport and optical properties of $LaGaO_3$ and $SrHfO_3$,

First in section III.2, we interested on the calculation of the electronic, optical and transport properties of the lanthanum gallate perovskite oxides compound, using the first-principles calculations based on the density functional theory. We determined the exchange and correlation effects by a generalized gradient approximation (GGA).,

Second in section III.3, we applied different percentage of doping $SrHfO_{3-x}S_x$ (x=0%, 8% and 16%) to reduce the gap value and we determine the electronic and optical properties of all percentage of S using density functional theory (DFT).

III.2 Study of $LaGaO_3$ compound

III.2.1 INRODUCTION

The perovskite materials have a lot of scientific interest because of their large and important applications in different area such as electrochromic [92], energy storage [93,94], solar cell [95,96], we can find the same material used in different domains due to their physical and chemical behaviors, such as density of states, fermi energy, dielectric function and phonon dispersion that have a unique nature. The perovskite-type oxides ABO_3 can be synthesized with a wide variety combinations of chemical elements, the A-site can be filled by cations M^{3+} (Fe, La, Gd), M^{2+} (Ca, Sr, Ba) or M^{+}(Na, K), and the B-site can be occupied by M^{3+} (Mn, Fe, Co, Ga), M^{4+} (Ce, Zr, Ti) or M^{5+} (Nb, W). The correlation between these sites gives us different structures, cubic, tetragonal, monoclinic, hexagonal and orthorhombic, it is known that cubic (Pm3m) is the ideal perovskite structure [97]. In this one the A cation is situated at the corner of the cube, while B cation is situated at the centre. This variety of ABO_3 combinations give us materials that can be used in various fields such as photovoltaic [98],

solid oxide fuel cells (SOFC) [99,100] and batteries [101,102]. The $LaAlO_3$, a typical perovskite with variety applications, has allured considerable interest as over layer in conventional thermal barrier coatings [103], as a Promotion of electrochemical performances of $LiNi_{0.8}Co_{0.1}Mn_{0.1}O_2$ cathode [104]. The pure lanthanum aluminate is a material with low ionic conductivity; doping $LaAlO_3$ with cations such as Sr^{2+} and Mg^{2+} results an excellent oxygen ionic conductor. $LaAlO_3$ has sparked renewal interest due to the discovery of two-dimensional electron gas at the interface between $LaAlO_3$ polar and non-polar $SrTiO_3$. The origin can be ascribed to oxygen vacancies [105], structural relaxation [106], polar discontinuity [107], intermixing at the interface [108] and cation nonstoichiometric [109]. Furthermore, the perovskite $LaGaO_3$ has a lot of scientific interest these last years because of its application in various field such as solid oxide fuel cells (SOFCs) [110], anode for rechargeable batteries [111] and also can be used as a substrate material for the epitaxial growth of high temperature superconducting thin films [112]. The $LaGaO_3$ perovskite oxide is crystallizes in orthorhombic structure with Pnma space group and transforms to rhombohedral symmetry at 145°C [113], the valence state of La and Ga is retain at (+3) in oxide, so when we doped $LaGaO_3$ [114] with cations that have a lower valence such as Mg or Ca, the concentration of oxygen vacancy can be substantially increased. And it has a band gap of 3.61 eV which is close to the experimental value of 4.4 eV [115] . However, to our best knowledge the transport properties of orthorhombic structure still have not been reported yet.

III.2.2 Structural properties

$LaGaO_3$ perovskite oxide with Pnma space group have a structure with four atoms of Lanthanum, four atoms of Gallium and twelve of Oxygen. The calculated and experimental lattice parameters are given in Table III.1. We used the experimental lattice parameters to do the optimization using a package developed by Tomas Kana. As a result of our calculation

from the standard DFT calculation we obtained a=5.580 Å, b=5.554 Å and c=7.874 Å, which gives results close to the experiment with in an error of 1%.

Table III.1 : The present work is calculated using the GGA-PBE sol method. The experimental and other theoretical lattice constants are listed for comparison.

Lattice parameters	Present work (Å)	Experiment (Å)[116]	Other theoretical (Å)
A	5.580	5.524	5.612[117], 5.477[117]
B	5.554	5.492	5.557[117], 5.463[117]
C	7.874	7.774	7.792[117], 7.735[117]

III.2.3 Electrical properties

We calculated the band structure of lanthanum gallate perovskite ($LaGaO_3$) using GGA-PBE density functional approximations. The results are illustrated in Figure III.1.

We have chosen the fermi level (E_F) to be zero at the top of the valence band. As shown in Figure III.1 the band gap of $LaGaO_3$ determined from GGA-PBE is 3.61 eV.

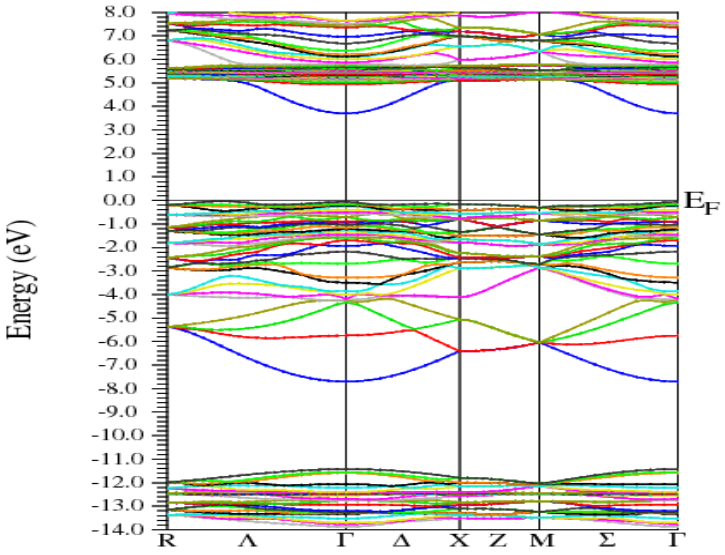

Figure III.1: Band structure of $LaGaO_3$ derived from GGA-PBEsol functional density

The total (DOS) and partial (PDOS) density of state of $LaGaO_3$ perovskite compound are shown in Figure III.2, where we observe that in the entire range La and Ga states hybridize

with O, inclusive of the conduction and valence bands, which indicate that La-O and Ga-O bonding are principally covalent. The electron charge was transferred from La and Ga to O due to the large difference between states, revealing the ionic bonding characteristic.

The band energy between -14.5 and -11.5 eV mainly consist of La(5p) and Ga(3d). According to Figure III.2.b we notice that the valence band with a width of 7.7 eV is consisting of O(2p), with small but no negligible contributions from La and Ga states. The conduction band located in the band energy between 5 and 10 eV with a width of 4.12 eV is consisting of La (4f).

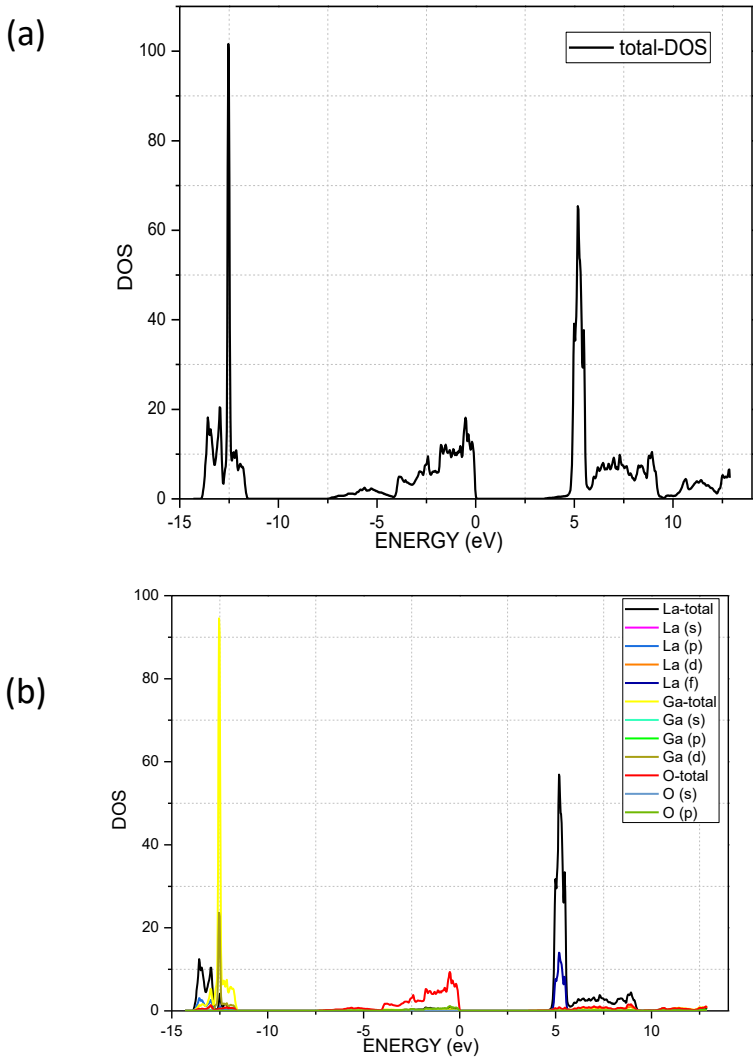

Figure III.2: DOS and PDOS of $LaGaO_3$ derived from various density functional approximation: (a) DOS with GGA-PBEsol functional; (b) PDOS with GGA-PBEsol.

III.2.4 Optical properties

To connect the electronic structures of a solid to the microscopic physical transitions between bands we use the dielectric function.

To calculate the complex part of this function we used the equation.

$$\varepsilon(w) = \varepsilon_1(w) + i\,\varepsilon_2(w) \quad \text{(III.1)}$$

The ε_2 and ε_1 are respectively the imaginary and real part of the dielectric function; we can determine the real part from the imaginary part using the Kramer-Kronig relations [118]. We can calculate the imaginary part by:

$$\varepsilon_{2(\omega)} = \frac{2\Pi e^2}{\Omega\varepsilon_0}\sum_{k,v,c} |\langle \Psi^c{}_k | u.r | \Psi^v{}_k \rangle|^2\, \delta(Eck - Evk - h\omega) \quad \text{(III.2)}$$

$$\varepsilon_1(\omega) = 1 + \left(\frac{2}{\Pi}\right) d\acute{\omega}\, \frac{\acute{\omega}^2 \varepsilon_{2(\acute{\omega})}}{\acute{\omega}^2 - \omega^2} \quad \text{(III.3)}$$

The c and v are the conduction and valence band, $\Psi^v{}_k$ and $\Psi^c{}_k$ are the wave function of valence and conduction band at k point, ε_0 is the vacuum dielectric constant, Ω is the volume, hw is the energy of the incident phonon, u is the vector defining the polarization of the incident electric field, u.r is the momentum operator.

From the real and imaginary part of the dielectric function we can determine all the optical proprieties such as the absorption α (ω), reflectivity *R* (ω), optical conductivity σ (ω), energy loss *L* (ω), refractive index *n* (ω) and the extinction coefficient *K* (ω).

$$\alpha(\omega) = \frac{2\omega}{c} k(\omega) \quad \text{(III.4)}$$

$$R(\omega) = \left| \frac{\sqrt{\varepsilon_1(\omega) + i\varepsilon_2(\omega)} - 1}{\sqrt{\varepsilon_1(\omega) + i\varepsilon_2(\omega)} + 1} \right|^2 \quad \text{(III.5)}$$

$$\sigma(\omega) = -i\frac{\omega}{4\Pi}[\varepsilon 1(\omega) + i\varepsilon(\omega) \quad \text{(III.6)}$$

$$L(\omega)=\mathrm{Im}\left[\frac{-1}{\varepsilon(\omega)}\right] \quad \text{(III.7)}$$

$$n(\omega)=\frac{1}{\sqrt{2}}\left\{\left[\varepsilon_1^2(\omega)+\varepsilon_2^2(\omega)\right]^{1/2}+\varepsilon_1(\omega)\right\}^{1/2} \quad \text{(III.8)}$$

$$K(\omega)=\frac{1}{\sqrt{2}}\left\{\left[\varepsilon_1^2(\omega)+\varepsilon_2^2(\omega)\right]^{1/2}-\varepsilon_1(\omega)\right\}^{1/2} \quad \text{(III.9)}$$

The dielectric function and all the optical proprieties are determined using GGA-PBE functional as shown in Figure III.3 According to the Figure III.3.a we notice that both the imaginary and real part of the dielectric function increased with energy and attained maximum at 7.8 and 5.1 eV, respectively. This peak is a result of the electron transition from O (2p) orbitals to La (4f) orbitals and Ga 4s4p orbitals, the real part of dielectric function start to decrease after the sharp peak and attained minimum at 9.8 eV. The absorption coefficient α (ω) of a material allows us to determine the penetration's degree of light into the material before being absorbed, As showing in Figure III.3.b we observe that the absorption decreases rapidly when the wavelength (λ) increases. The max value of the absorption 65×10^4 cm^{-1} is obtained at ultraviolet light (λ=200 nm). When we go over λ=200 nm, we notice a rapid decrease of the absorption as a function of λ, after that we obtain a stable value 0.2×10^4 cm^{-1} in the visible and infrared. According to Figure III.3.c the optical conductivity σ (ω) was zero when the energy is less than 3.6 eV, the optical conductivity increases with energy and reached a maximum value at 7.6 eV. The energy loss L (ω) in a fast electron passing through the material is described by the energy loss function. According to Figure III.3.d we notice that the largest energy loss peak occurs at about 12.8 eV, representing the characteristic affiliated with plasma oscillation. The refractive index n (ω) is a dimensionless size characteristic of a medium, describing the behavior of light in it, this depends on the measurement wavelength, but also the characteristics of the environment (in particular pressure and temperature). From the Figure III.3.e, we notice that the refractive index is 2.8 when the wavelength is equal to ~ 250 nm (ultraviolet). In the range of wavelength between

400 and 1000 nm, we observe that the refractive index is conserved at 2.1. The Figure III.3.f shows that the reflectivity R (ω) decreases with the wavelength, we observe that the highest value of R (0.26) is obtained in ultraviolet at 220 nm. For both approximation the reflectivity decreases as a function of λ. We notice that the reflectivity stabilizes at 0.12 in the visible and infrared.

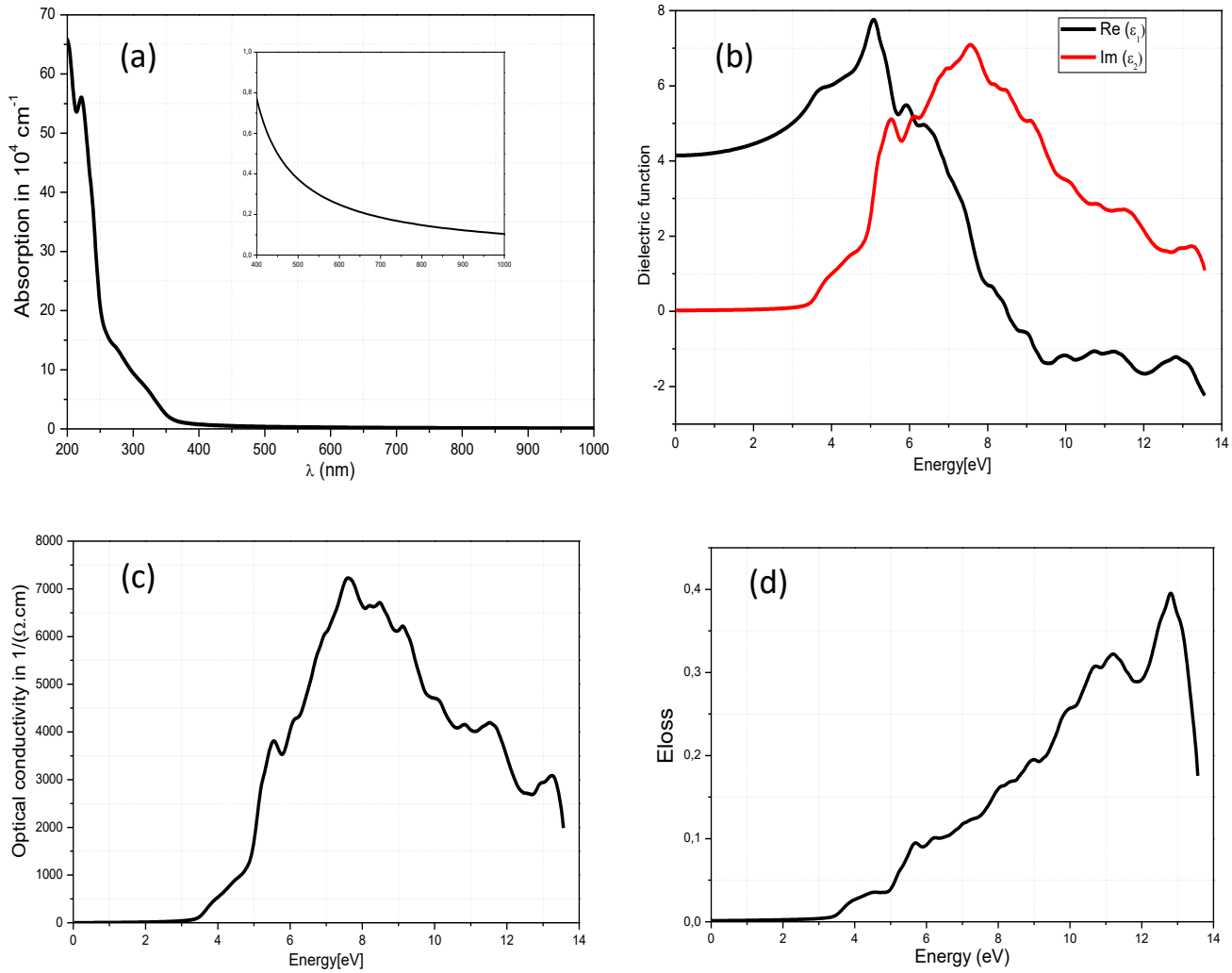

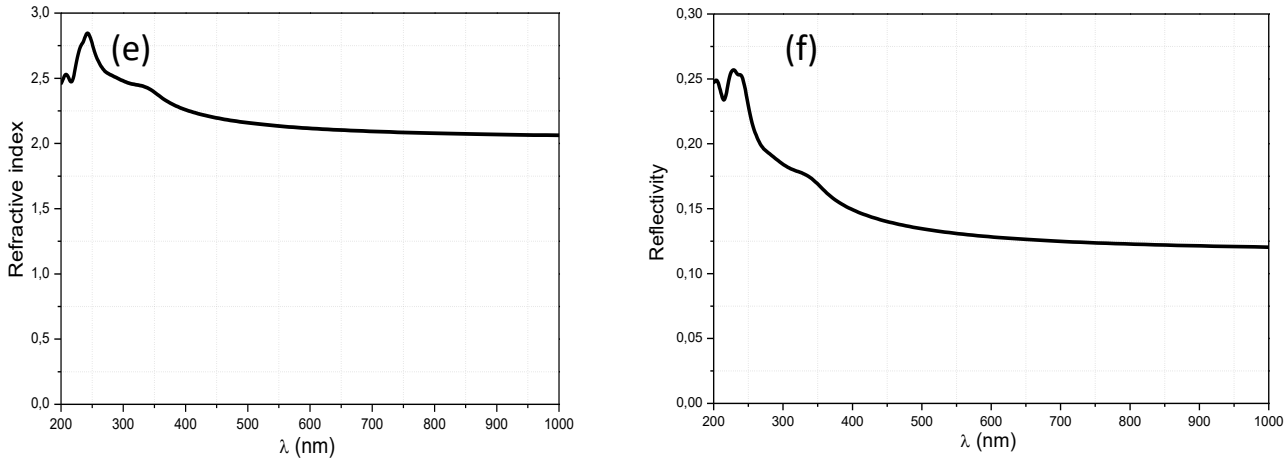

Figure III.3: The optical proprieties of $LaGaO_3$ derived from various density functional approximation: (a) Dielectric function; (b) absorption; (c) optical conductivity; (d) Energy loss; (e) refractive; (f) reflectivity

III.2.5 Transport properties

To calculate the transport proprieties, we used the semi-classical Boltzmann theory embedded in BoltzTraP code. The band-structure and the crystal structure determined by wien2k are used as an input to run the Bolztrap code, we had as results the electrical conductivity (σ/τ), Seebeck coefficient (S), electronic thermal conductivity (κ_e), and electronic power factor (P_F). The Seebeck coefficient (S) allows us to indicate if we have a domination of charge carrier, S with a negative sign represent n-type materials, positive sign p-type materials. According to Figure III.4.a we notice that we have a positive sign of S (p-type) in the entire range of temperature. We can conclude that our compound is a P-type material. The electrical conductivity (σ) of $LaGaO_3$ is illustrated in Figure III.4.b showing that the electrical conductivity increases rapidly by increasing temperature and reach a maximum at 800 °K with a value of ~ 10×10^{18} $(\Omega.m.s)^{-1}$. $P_F = S^2 \sigma/\tau$ represent the power factor, were P_F is proportional to the electrical conductivity (σ/τ) and the square of Seebeck coefficient (S^2). From the Figure III.4.d we observed that the power factor was almost zero at low temperature (<50 °K), then we had a rapid increase of power factor when the temperature increases to

reach a maximum value (3.7 10^{11} W/m.k².s) at 800 °K. The thermal conductivity *K* of any material depend on the molecular vibrations and the motion of the free electrons. From the Figure III.4.c, we notice that the electronic thermal conductivity increases with the temperature, so we can say that the molecular vibration increases.

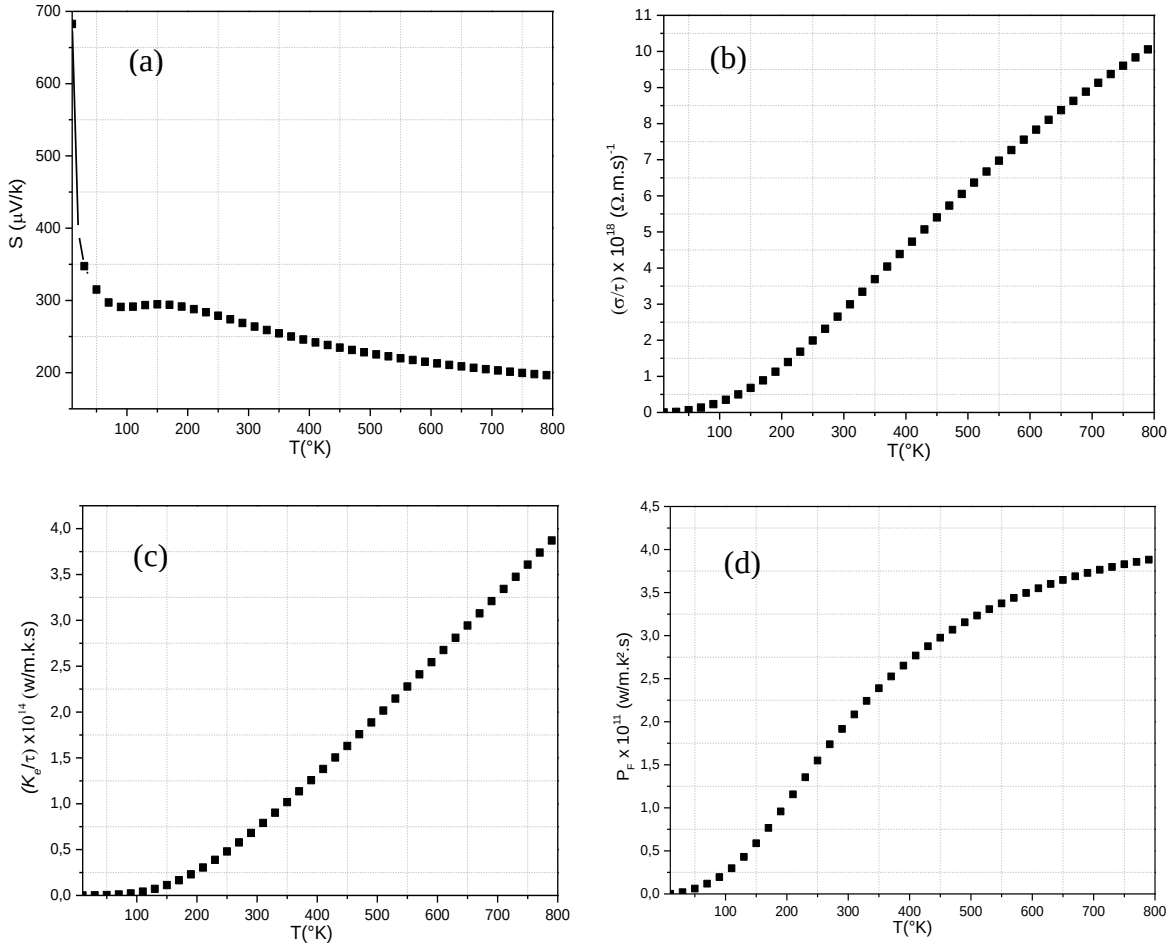

Figure III.4: The transport proprieties of $LaGaO_3$ derived from Bolztrap code: (a) Seebeck coefficient; (b) the electrical conductivity; (c) electronic thermal conductivity; (d) electronic power factor.

III.3 Study of $SrHfO_3$ doped S compound

III.3.1 Introduction

Mineral exploration was intense during the 18th and 19th centuries in the Ural Mountains in Russia. Which led to the appearance of numerous local mines. 1839 has experienced the discovered of $CaTiO_3$ perovskite in the Akhmatov mine by A.B. Kemmerer and the German

mineralogist, Gustav Rose, who first described it and named it after the Russian mineralogist Lev Aleksevich von Perovski [119,120]. Since then, all structures analogous to $CaTiO_3$ are described using the term perovskite. The oxide perovskite, with general chemical formula ABO_3, have three distinct crystallographic sites. A is occupied by a cation, generally wider than the cation occupying the site B and the oxygen draws an octahedron around B. Another type of perovskite is the halide perovskite which has been intensively studied. Similar to oxides, the general formula of halide perovskite is ABX_3. This time, site A is occupied by a monovalent cation, often alkaline. Site B can accommodate a divalent metal cation (for example Pb^{2+}). The X halides can be Cl, Br and I and we have also chalcogenide perovskite with a general formula of ABX_3 similar to the other type of perovskites, the X site is occupied by S or Se, and we have also double perovskites ABX_6 [121,122]. Halide perovskite solar cells had a huge scientists' attention these last years due to the rapid increase of the power conversion efficiency (PCE) form 3.8% in 2009 [123] to now over 23% [124]. The PCE of this halide perovskite becomes comparative to the commercial silicon. While these perovskites materials show potential in the photovoltaic field, more research indicates that these materials could also be used for other applications such as light emitting diodes (LEDs), lasers, photo-detection and biomedical imaging [125–135]. The major inconvenient of these materials is the chemical instability under ambient conditions, the stability for the organic halide perovskite, the toxicity, the probable carcinogenicity of lead and lead halides [136-138]. The perovskite $SrHfO_3$ compound is a promising candidate for the next generation of CMOS devices, due to its good electrical and physical properties [139]. This compound adopts the orthorhombic structure which conforms to Pbmn space group under ambient conditions and at higher temperatures the structure is the ideal cubic perovskite which conforms to Pm3m space group [140-142].

In this paper, we determined the electronic and optical properties of perovskite $SrHfO_3$ compound using the density functional theory (DFT). Which indicate that it has an indirect gap with value of 5.60 eV, that's why the aim of our work is to reduce the gap value and for that we used a different percentage of doping with S atom. As a result we obtained a direct band gap and we reduced the gap value from 5.60 eV to 4.06 eV and 2.09 eV equivalents to 8% and 16% of S, respectively.

III.3.2 Structural properties

As showing in **Figure III.5** $SrHfO_3$ perovskite oxide with Pbmn space group have a structure with four atoms of Strontium, four atoms of Hafnium and twelve of Oxygen. The calculated

and experimental lattice parameters are given in **Table III.2**. The optimization of lattice parameters is determined using the experimental lattice parameters using a package developed by Tomas Kana as showing in **Figure III.6**. As a result of our calculation from the standard DFT calculation we obtained a=5.580 Å, b=5.554 Å and c=7.874 Å. These parameters are in good agreement with experimental data [143].

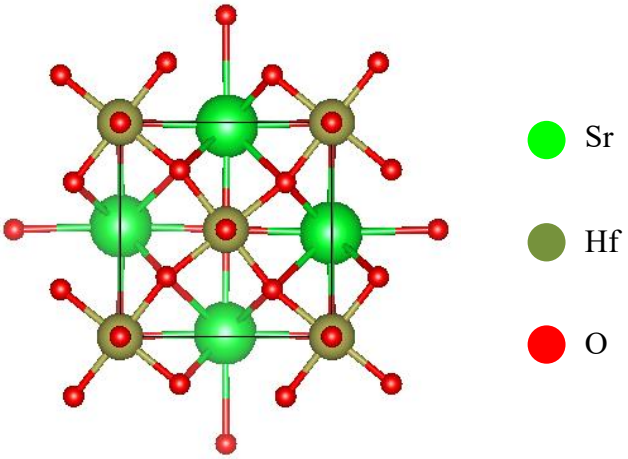

Figure III.5: $SrHfO_3$ Orthorhombic structure.

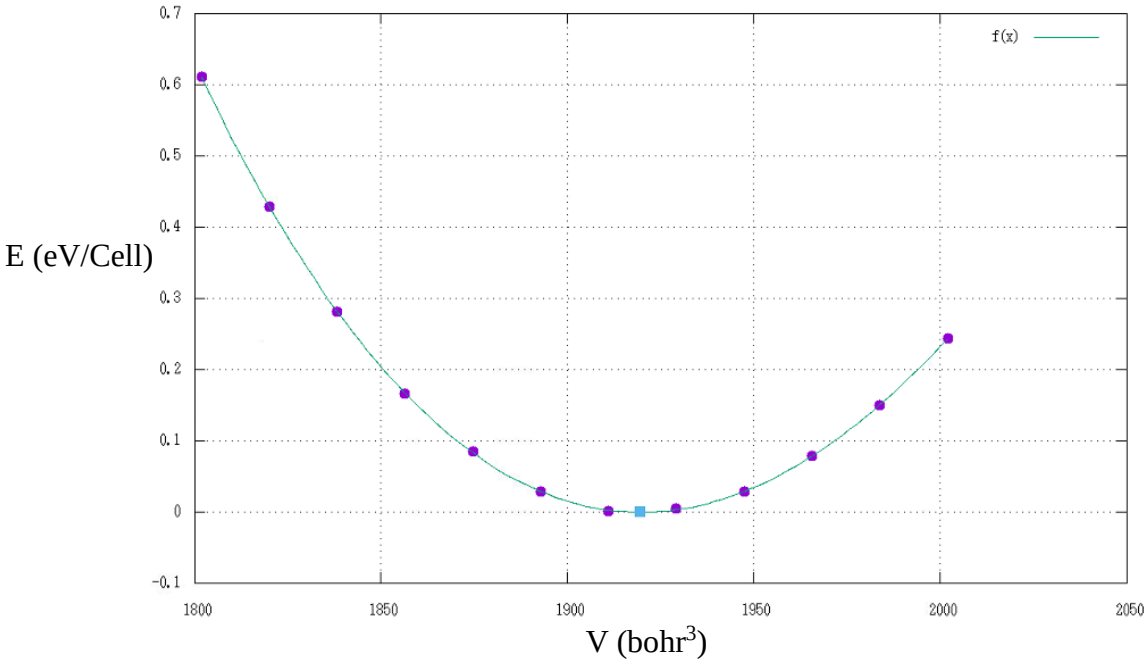

Figure III.6: $SrHfO_3$ Orthorhombic E as function of V.

Table III.2: Lattice parameters of perovskite $SrHfO_3$ compound.

Lattice parameters	Present work (Å)	Experiment (Å)[143]	Other theoretical (Å)[143]
a	5.7690	5.7516	5.6887
b	5.8035	5.7646	5.7016
c	8.2758	8.1344	8.0455

III.3.3 Electrical properties

Table III.3 shows the evolution of the gap value as function of the percentage of doping. The value of the gap reduces from 5.69 eV (0% of S) to 2.13 eV (16% of S) for Optical gap and from 5.60 eV (0% of S) to 2.09 ev (16% of S) for gap energy. From **Figure III.7** we notice that the band gap is indirect for the bulk $SrHfO_3$, and become direct band gap for the 8% and 16% of S.

Table III.3: Energy and optical gaps for different concentration of S: 0%, 8% and 16%.

compound	Present work			Experimental [144]
	Gap energy (eV)		Optical Gap (eV)	
	GGA-PBE	GGA-MBJ		
$SrHfO_3$	3.99	5.60	5.69	6.1
8% of S	2.77	4.06	4.24	----
16% of S	1.11	2.09	2.13	----

(a)

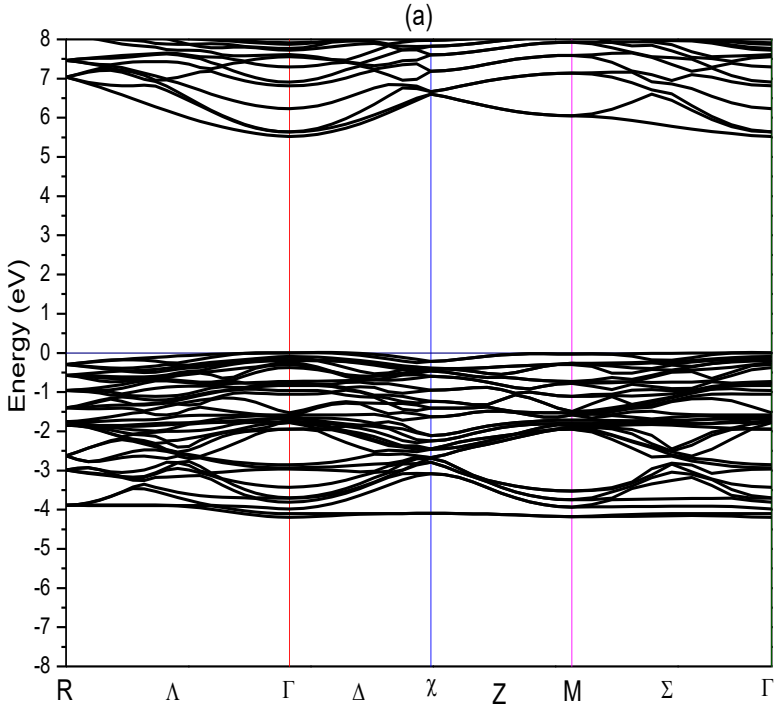
Energy (eV)
8
7
6
5
4
3
2
1
0
-1
-2
-3
-4
-5
-6
-7
-8
R
Λ
Γ
Δ
χ
Z
M
Σ
Γ

(b)

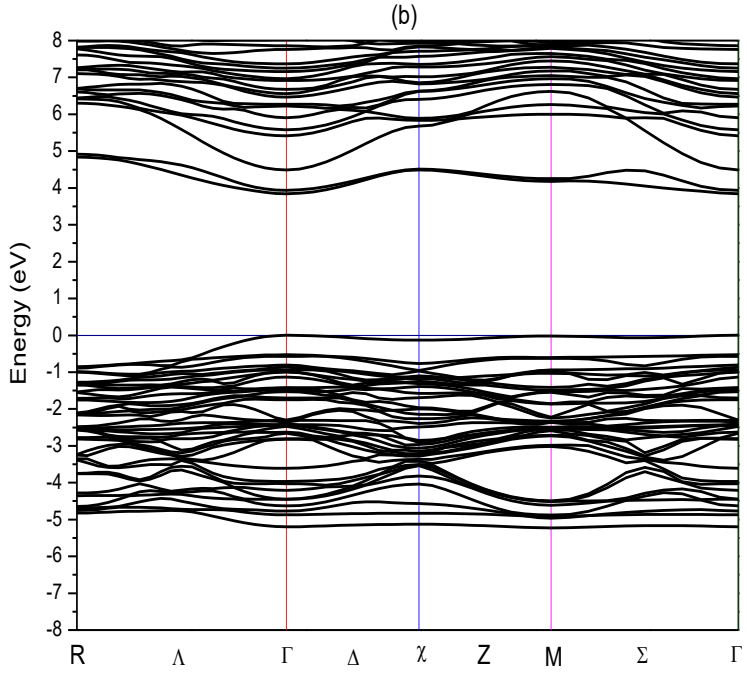
Energy (eV)
8
7
6
5
4
3
2
1
0
-1
-2
-3
-4
-5
-6
-7
-8
R
Λ
Γ
Δ
χ
Z
M
Σ
Γ

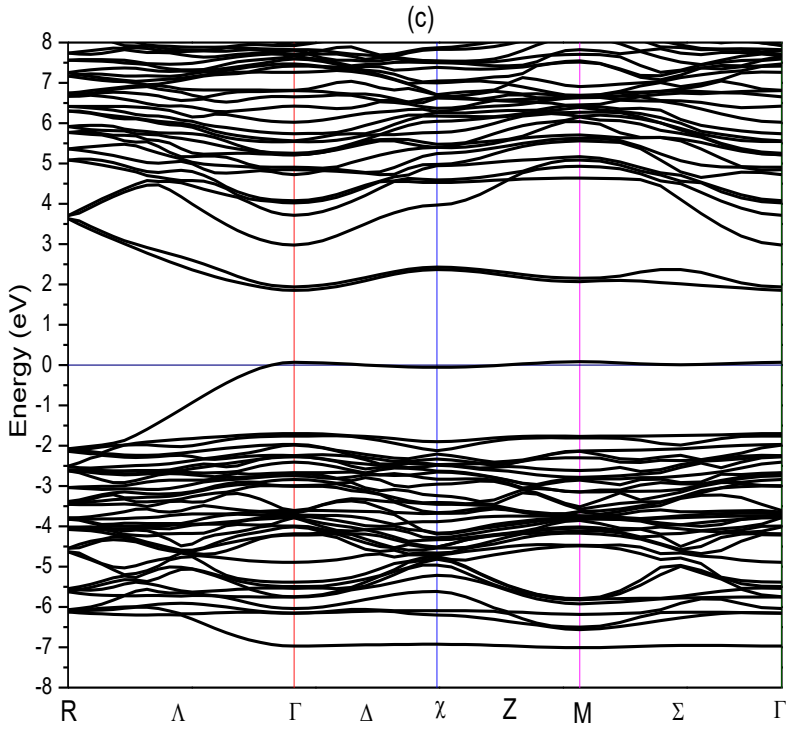

Figure III.7: Band structure of $SrHfO_{3-x}S_x$ compound: a) 0% of S b) 8% of S c) 16% of S

As showing in **Figure III.8(a-f),** we notice that Sr and Hf states hybridize with O and S in the entire range, inclusive of the conduction and valence bands, which indicate that Sr-O, Hf-O, Sr-S and Hf-S bonding are principally covalent. In addition, the electron charge was transferred from Sr and Hf to O and S due to the large difference between states, revealing the ionic bonding characteristic. **Figure III.8.b** shows that the valence band consists of O (2p) and a small contribution from Hf and Sr states with a width of 4.05 eV. The conduction band is consisting of Sr (3d), Hf (5d) and O (2p). From **Figure III.8.d** we observe that the length of the valence band of doped $SrHfO_3$ with 8% of S is 5 eV consisting of O (2p) and S (2p) with a small contribution from Hf and Sr states, and the conduction band is consisting of of Sr (3d), Hf (5d), O (2p) and S (2p). From **Figure III.8.f** we observe that the length of the valence band of doped $SrHfO_3$ with 16% of S is 6 eV consisting of O (2p) and S (2p) with a small contribution from Hf and Sr states, and the conduction band is consisting of of Sr (3d), Hf (5d), O (2p) and S (2p).

(a)

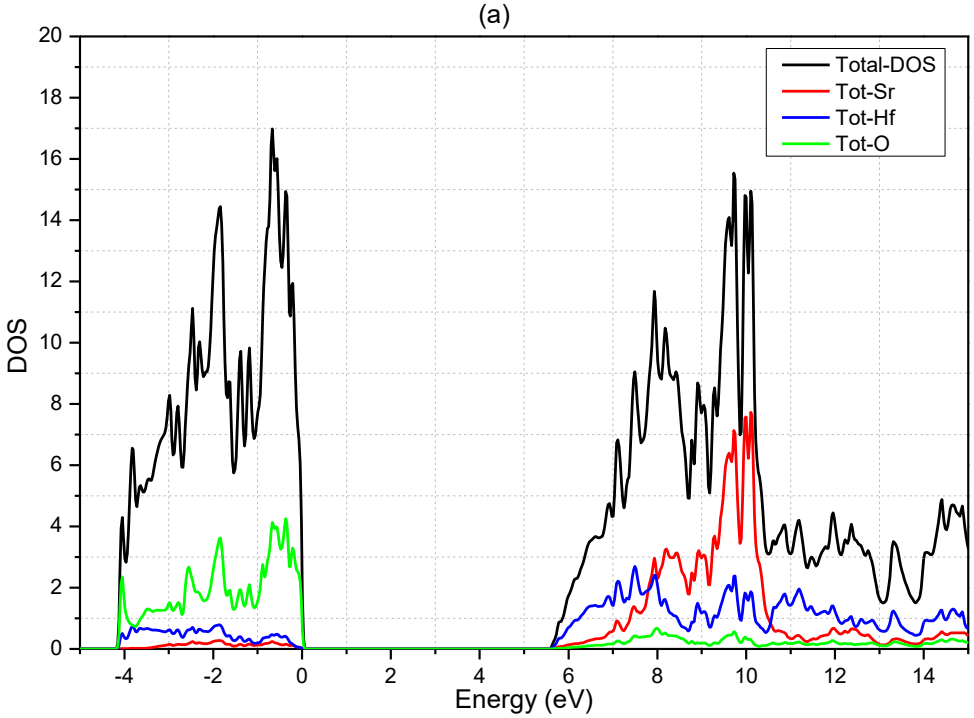
Total-DOS
Tot-Sr
Tot-Hf
Tot-O
DOS
Energy (eV)

(b)

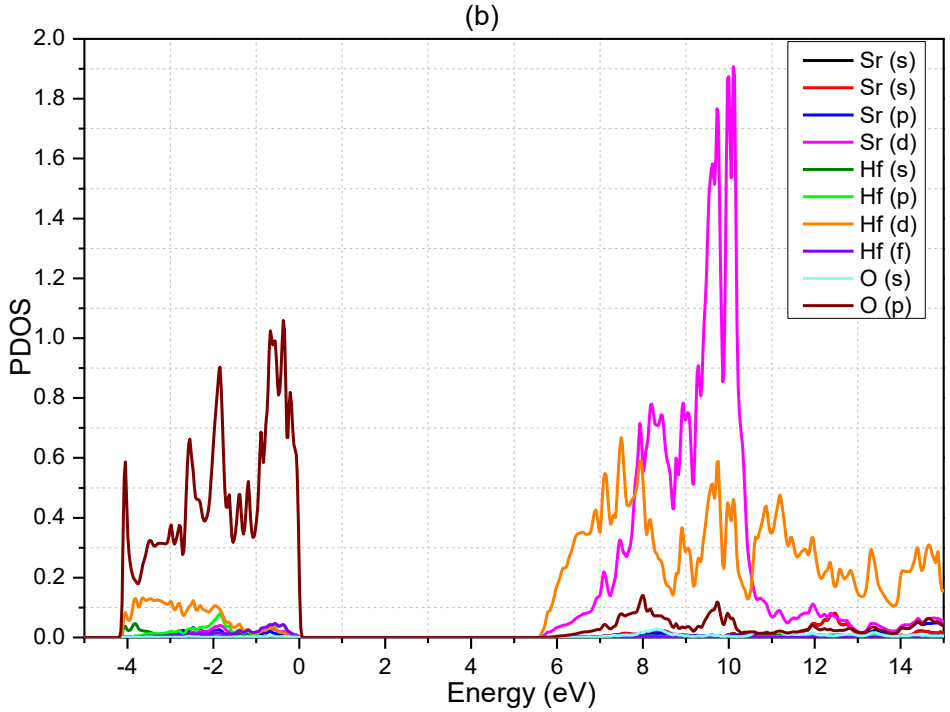
Sr (s)
Sr (s)
Sr (p)
Sr (d)
Hf (s)
Hf (p)
Hf (d)
Hf (f)
O (s)
O (p)
PDOS
Energy (eV)

(c)

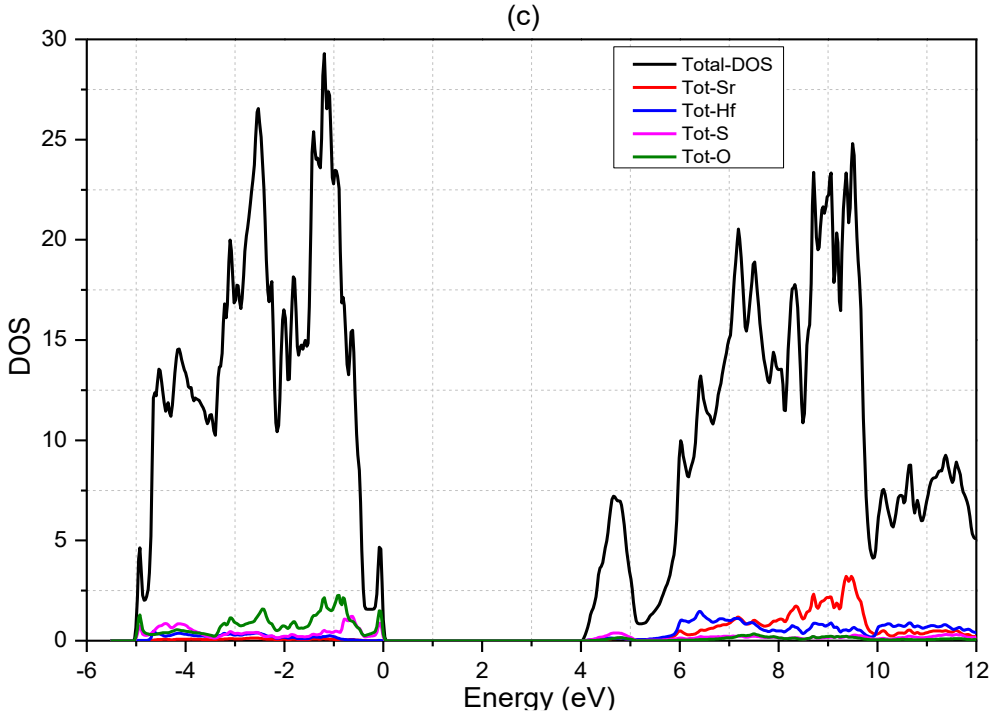
Total-DOS
Tot-Sr
Tot-Hf
Tot-S
Tot-O
DOS
Energy (eV)

(d)

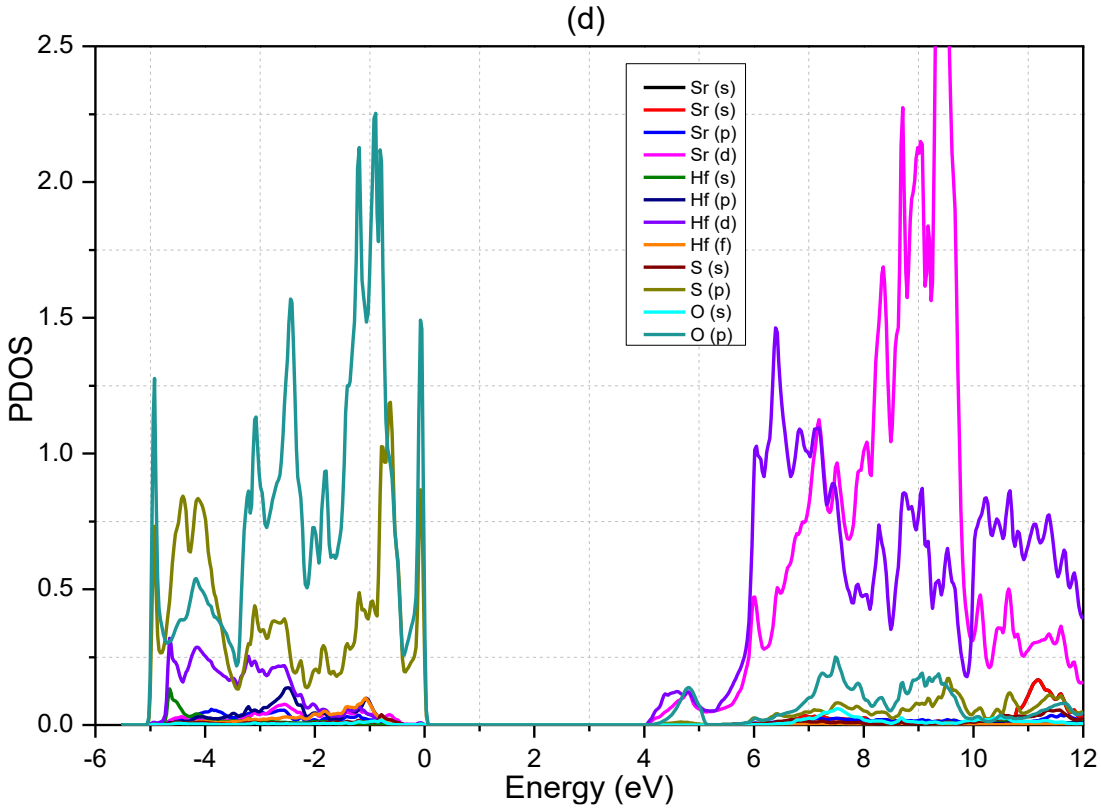
Sr (s)
Sr (s)
Sr (p)
Sr (d)
Hf (s)
Hf (p)
Hf (d)
Hf (f)
S (s)
S (p)
O (s)
O (p)
PDOS
Energy (eV)

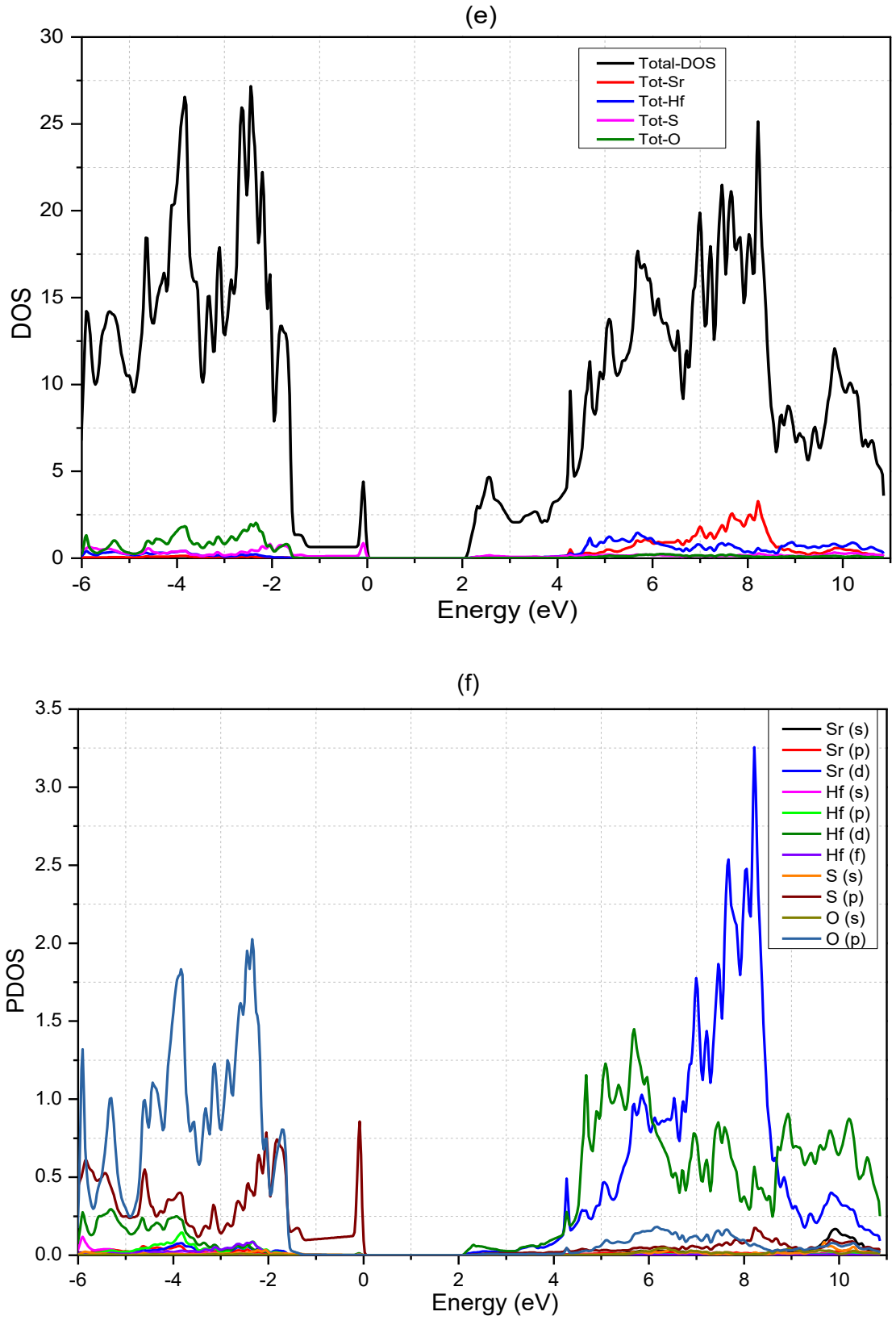

Figure III.8: Density of states of $SrHfO_3$ compound doped with S: a) bulk DOS b) bulk PDOS c) DOS of 8% of S d) PDOS of 8% of S e) DOS of 16% of S f) PDOS of 16% of S.

III.3.4 Optical properties

The absorption coefficient α (ω) of a material allows us to determine the penetration's degree of light into the material before being absorbed. **Figure III.9.a** shows that the absorption increases as function of photon energy (decreases of wavelength (λ)). The max value of absorption for the bulk $SrHfO_3$ is 8.45×10^4 cm^{-1} obtained at ultraviolet light (λ=200 nm), 58.14×10^4 cm^{-1} for 8% of S obtained at ultraviolet light (λ=213 nm) and 92.15×10^4 $cm^{-1}$for 16% of S obtained at ultraviolet light (λ=229 nm). When we go over this peak, we notice a rapid decrease of the absorption as a function of λ. As showing in **Figure III.9.b** we notice that the reflectivity R (ω) increases with increasing the photon energy, the highest value of reflectivity for bulk $SrHfO_3$ is 0.135 (13.5%) obtained in ultraviolet at 200 nm, 0.219 (21.9%) for 8% of S obtained at ultraviolet (λ=226 nm), 0.329 (32.9%) for 16% of S obtained at ultraviolet at (λ=235 nm).

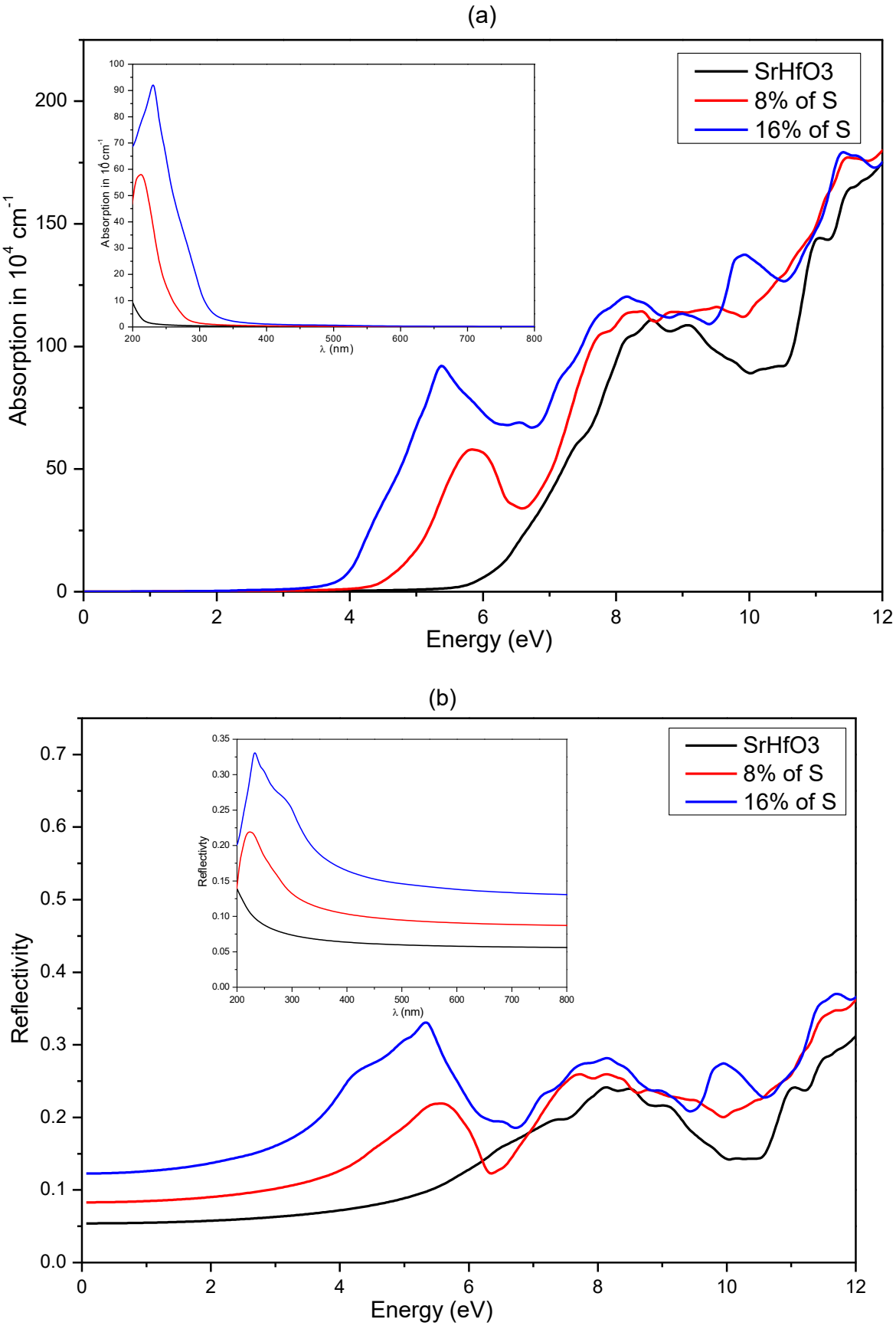

Figure III.9: Optical properties of $SrHfO_3$ compound doped with S: a) absorption b) reflectivity.

Chapter IV

Theoretical calculations of Chalcogenide perovskite ABS_3

IV.1 Introduction

In the fourth chapter of this thesis, we present a theoretical investigation of electronic, structural, transport and optical properties of $BaZrS_3$,

In this work we applied a different percentage of doping $BaZrS_{3-x}Se_x$ (x=0%, 10%, 15% and 20%) to reduce the gap value of $BaZrS_3$ and we calculated the electronic, optical and transport properties of all percentage of Se using density functional theory (DFT).

IV.2 Study of $BaZrS_3$ compound

IV.2.1 INRODUCTION

Historically, mineral exploration for metallurgy was intense during the 18th and 19th centuries in the Ural Mountains in Russia. This prospecting led to the appearance of numerous local mines. In 1839, the $CaTiO_3$ perovskite was discovered in the Akhmatov mine by A.B. Kemmerer and the German mineralogist, Gustav Rose, who first described it and named it after the Russian mineralogist Lev Aleksevich von Perovski [145,146]. Since then, the term perovskite is used to describe all structures analogous to $CaTiO_3$. These oxides, of general chemical formula AMO_3, have three distinct crystallographic sites. The site A is occupied by a cation, generally wider than the cation occupying the site M and the oxygen draws an octahedron around M. The structural diversity in the family of perovskite is due to the numerous atoms which can play each of these roles. Another family of perovskite, halides perovskite, has been intensively studied since 2012. Like oxides, the general formula describing halides perovskite is AMX_3. This time, site A is occupied by a monovalent cation, often alkaline. Site M can accommodate a divalent metal cation (for example Pb2 +). The oxygen is replaced by X halides, the most common being Cl, Br and I. Halide perovskite solar cells attracted scientists' attention these last years due to the rapid increase of the power conversion efficiency (PCE) form 3.8% in 2009 [147] to now over 23% [148]. The PCE of this halide perovskite is comparative to the commercial silicon, but the major inconvenient is

the chemical instability under ambient conditions, the toxicity, the stability for the organic halide perovskite and the probable carcinogenicity of lead and lead halides [149-151]. Recently, chalcogenide perovskite is considered as a new class of semiconductor, with general formula ABX3 where A = Mg, Ca, Sr, Ba, Zn, Cd, Sn, Pb, B = Ti, Zr, Hf, Si, Ge, Sn, Pb and X = S, Se. They are more ionic than conventional semiconductors but less than oxides or halides. These types of perovskite were synthesized more than a half century ago but have received little attention [152-156] that's why there is limited knowledge of their physical properties [157, 158]. The situation changed, after the theory work that screened [159] 18 ABX_3 chalcogenide materials, the mentioned study revealed a several compounds with direct bandgap, very high absorption and good carrier mobility, allowing them to be considered prospective materials for optoelectronic applications. The experimental efforts have succeeded the synthesizing of several chalcogenide perovskite as example $BaZrS_3$, $CaZrS_3$, $SrTiS_3$, $SrZrS_3$ [160], and SrHfS3 [161, 162]. Chalcogenide perovskite $BaZrS_3$ crystallizes in orthorhombic structure with Pnma space group as showing in Figure IV.1 with unit-cell parameters a=7.04 Å, b=9.98 Å and c=7.05 Å [161] and a good light absorption, in good agreement with our theory. The material was found to be stable against moisture, oxidation [161] and pressure [163].

The aim of our work is to study the $BaZrS_3$ properties using density functional theory (DFT), as a result we found that this compound has a high absorption and gap value of 1.62 eV, that's why we focused on the reduce of the gap value by applying different percentage of doping using Se atoms $BaZrS_{3-x}Se_x$ with (x=0.1, 0.15, 0.2). We calculate electrical and optical properties. As a result, the gap value reduces from 1.62 eV for the bulk $BaZrS_3$ to 1.37 eV corresponding to 20% of Se.

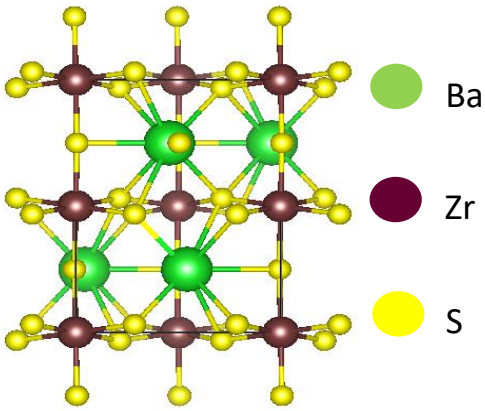

Figure IV.1: $BaZrS_3$ structure

- **Computational Methods**

All calculations illustrated in this work are based on DFT, we used Wien2k ab initio simulation program to obtain the solution of Kohn-Sham equations [164]. We determined the exchange and correlation effects by a generalized gradient approximation of Perdew−Burke−Ernzerhof for solid (GGA-PBE) and to improve the band structure we used (GGA-MBJ) approximation. The electronic and optical properties have been calculated in stable orthorhombic phase which conforms to Pnma space group. In these calculations we had a 9×6×4 Monkhorst−Pack set of k-point mesh of Brillouin zone integration generated automatically, the Rmt*Kmax value was fixed to 7 (RMT presents the small radius of the muffin-tin sphere, while Kmax present the size of the largest vector in the plane wave expansion).

The transport properties are calculated using Bolztrap code.

IV.2.2 Electrical properties

Table IV.1 and Figure IV.2 show the evolution of the gap value as a function of the percentage doping.

The value of the gap reduces from 1.62 eV (0% of Se) to 1.37 eV (20% of Se) for Optical gap and from 1.59 eV (0% of Se) to 1.35 ev (20% of Se) for gap energy. The gap energy calculated from GGA-Mbj (1.59 eV) is almost equal to the experimental value (1.7 eV).

Table IV.1. energy and optic Gaps for different concentration of Se: (x=0, 0.1, 0.15 and 0.2)

	Gap energy (eV)			**Optical Gap (eV)**
	Theoretical		experimental	
	GGA-PBE	GGA-MBJ		
$BaZrS_3$	1.16	1.59	1.7 [161]	1.62
10% of Se	1.04	1.47	-------	1.49
15% of Se	1.00	1.41	-------	1.42
20% of Se	0.95	1.35	-------	1.37

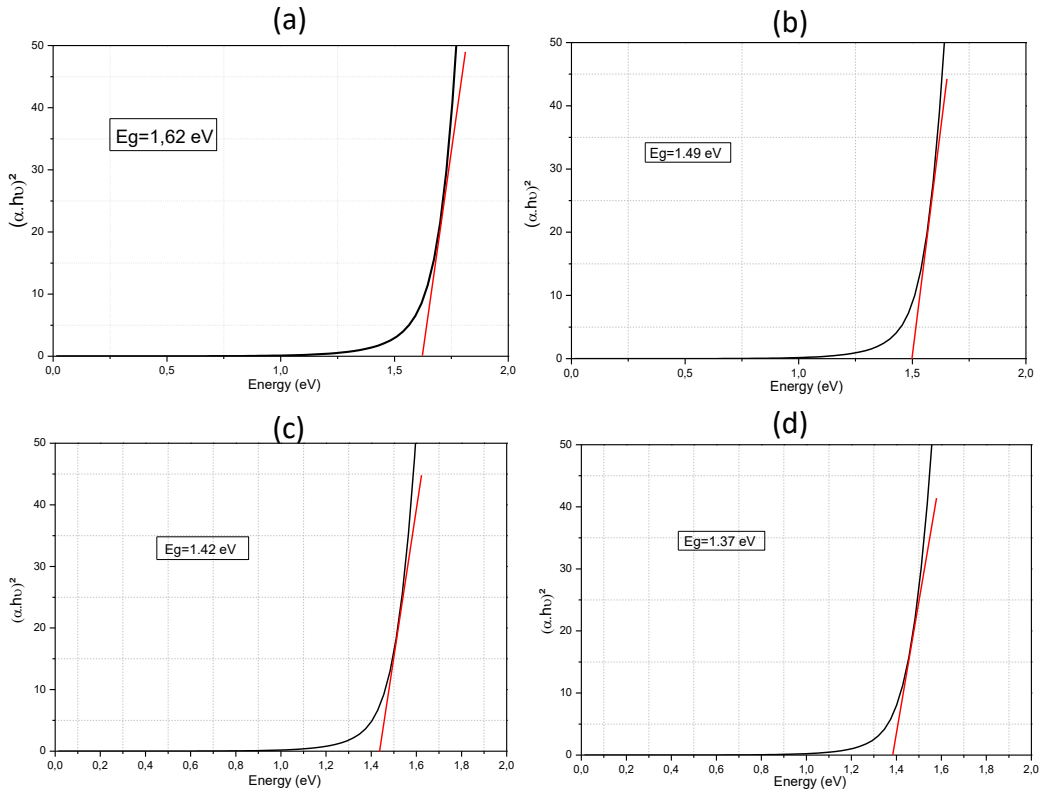

Figure IV.2: Optical band gap of BaZrS3 doped with Se: a) bulk b) 10% of Se c) 15% of Se d) 20% of Se.

According to Figure IV.3 we notice that Ba and Zr states hybridize with S and Se states in the entire valence band range indicating that Ba-S, Zr-S, Ba-Se and Zr-Se bonds are principally covalent. In addition, the electron charge was transferred from Ba and Zr to S and Se due to the large difference between states, revealing the ionic bonding characteristic. From Figure IV.3.b we notice that the valence band with a width of 4.12 eV is consisting of S (2p), with small but no negligible contributions from Ba and Zr states and the conduction band with a width of 2.6 eV is consisting of Zr (4d) and S (2p). We observe from Figure IV.3.c, d and e that the length of the valence band of doped $BaZrS_{3-x}Se_x$ (x=0.1, 0.15 and 0.2) is 4.36 eV consisting of S(2p) and Se (4p), and The conduction band with a width of 2.55 eV is consisting of Zr (4d), S (2p) and Se (4p). Furthermore, as can be seen from Figure IV.3, the principal contributors to the valence band of chalcogenide perovskites BaZrS3 are p-states associated with the chalcogen atom that give the main input in the upper and central portions of the valence band, this peculiarity is completely the same as it is detected for p states associated with halide atoms in related halide perovskites ABX_3 [164-168].

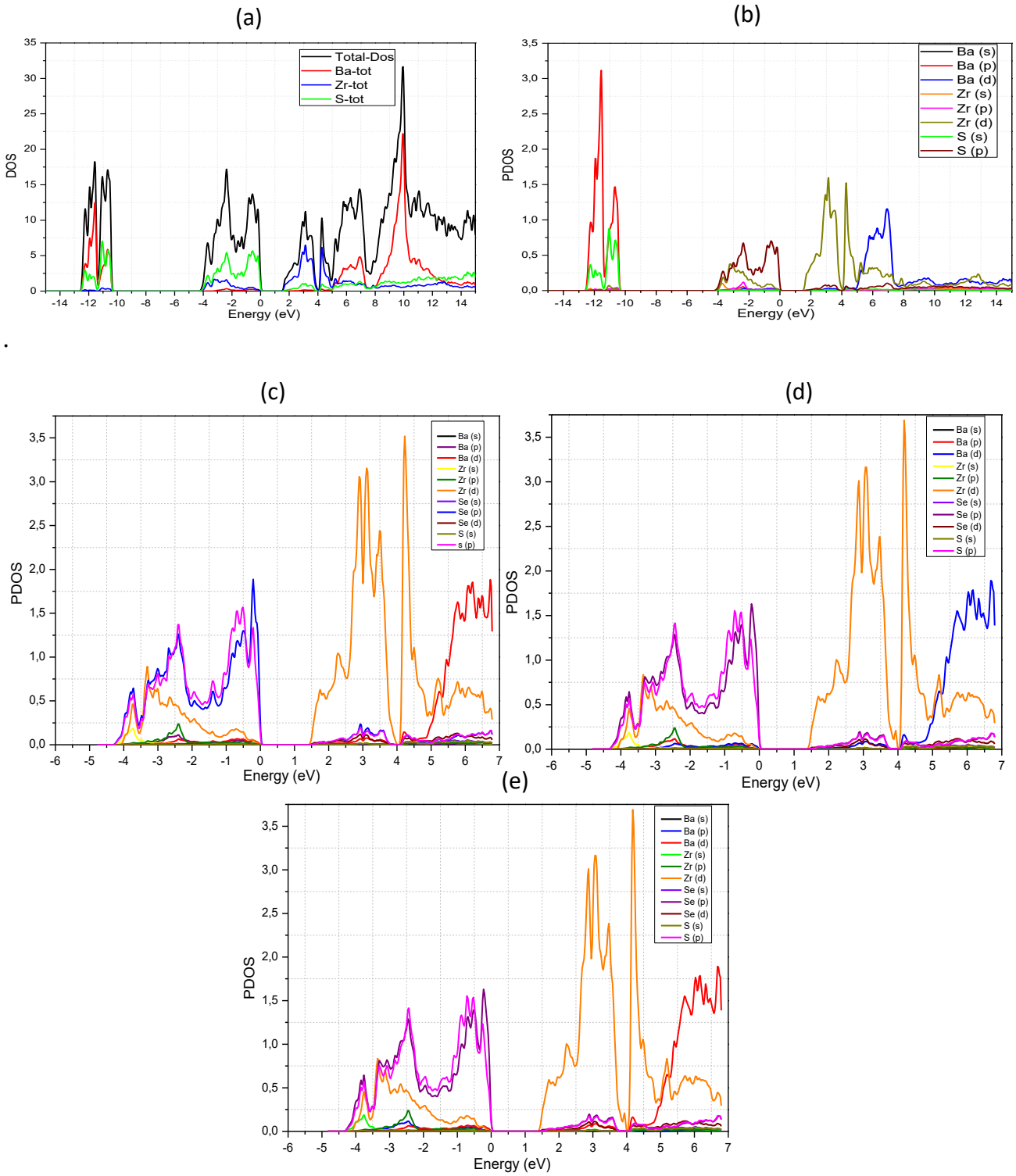

Figure IV.3**:** Density of states of $BaZrS_3$ Doped Se : a) bulk DOS b) bulk PDOS c) 10% of Se d) 15% of Se e) 20% of Se.

IV.2.3 Optical properties

The absorption coefficient α (ω) of a material allows us to determine the penetration's degree of light into the material before being absorbed, As showing in Figure IV.4.a we observe that the absorption decreases rapidly when the wavelength (λ) increases. The maximum absorption value for BaZrS3 is 59.29×10^4 cm^{-1} obtained at ultraviolet light (λ=276 nm), 59.76×10^4 cm^{-1} for 10% of Se obtained at ultraviolet light (λ=281 nm), 60.58×10^4 $cm^{-1}$for 15% of Se obtained at ultraviolet light (λ=284 nm) and 60.87×10^4 $cm^{-1}$for 20% of Se obtained at ultraviolet light (λ=288 nm), after that we observe another peak 69.70×10^4 at ultraviolet light (λ=323 nm), 70.04×10^4 at ultraviolet light (λ=324 nm), 70.31×10^4 at ultraviolet light (λ=326 nm) and 70.68×10^4 at visible light (λ=328 nm) for bulk $BaZrS_3$, 10% of Se, 15% of Se and 20% of Se, respectively. When we go over the second peak, we notice a rapid decrease of the absorption as a function of λ.

The Figure IV.4.b shows that the reflectivity R (ω) decreases with the wavelength, we observe that the highest value of reflectivity for bulk $BaZrS_3$ is 0.356 (35.6%) obtained in ultraviolet at 349 nm, 0.354 obtained in ultraviolet at 338 nm for 10% of Se, 0.357 obtained in ultraviolet at 340 nm for 15% of Se and 0.359 obtained in ultraviolet at 340 nm for 20% of Se. The reflectivity decreases as a function of λ.

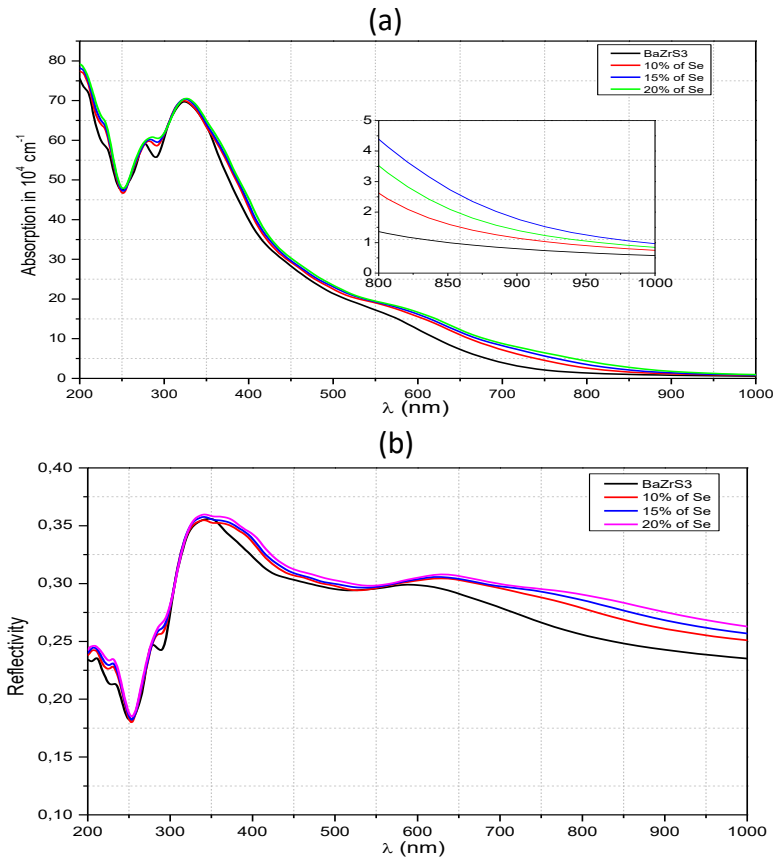

Figure IV.4**:** Optical properties of BaZrS3 doped with Se: (a) absorption coefficient, (b) optical reflectivity.

IV.2.4 Transport properties

To calculate the transport proprieties, we used the semi-classical Boltzmann theory embedded in BoltzTraP code. The band-structure and the crystal structure determined by wien2k are used as an input to run the BoltzTraP code, we had as results the electrical conductivity (σ/τ), Seebeck coefficient (S), electronic thermal conductivity (κ_e), and electronic power factor (P_F). The Seebeck coefficient (S) allows us to indicate if we have a domination of charge carrier, if we have negative sign of S we say that our compound is n-type materials, positive sign p-type materials. Figure IV.5.a shows that all compounds have a positive sign of S (p-type) in the entire range of temperature. We can conclude that our compounds are a P-type material. The electrical conductivity (σ) is illustrated in Figure IV.5.b showing that the electrical conductivity varies depending on the temperature, when the T= 10°K the maximum value of σ

is 2.77×10^{18} $(\Omega.m.s)^{-1}$ corresponding to 20% of Se, above this temperature we notice a small decrease until T~30°K, after that the the electrical conductivity increases rapidly and reach a maximum at 300°K with a value of ~4.4×10^{18} $(\Omega.m.s)^{-1}$ for bulk $BaZrS_3$, 2.79×10^{18} for 10% of Se, 2.30×10^{18} for 15% of Se and 1.63×10^{18} for 20% of Se. The thermal conductivity K_e of any material depends on the motion of the free electrons and the molecular vibrations. Figure IV.5.c shows that the electronic thermal conductivity increases with the temperature, so we can say that the molecular vibration increases.

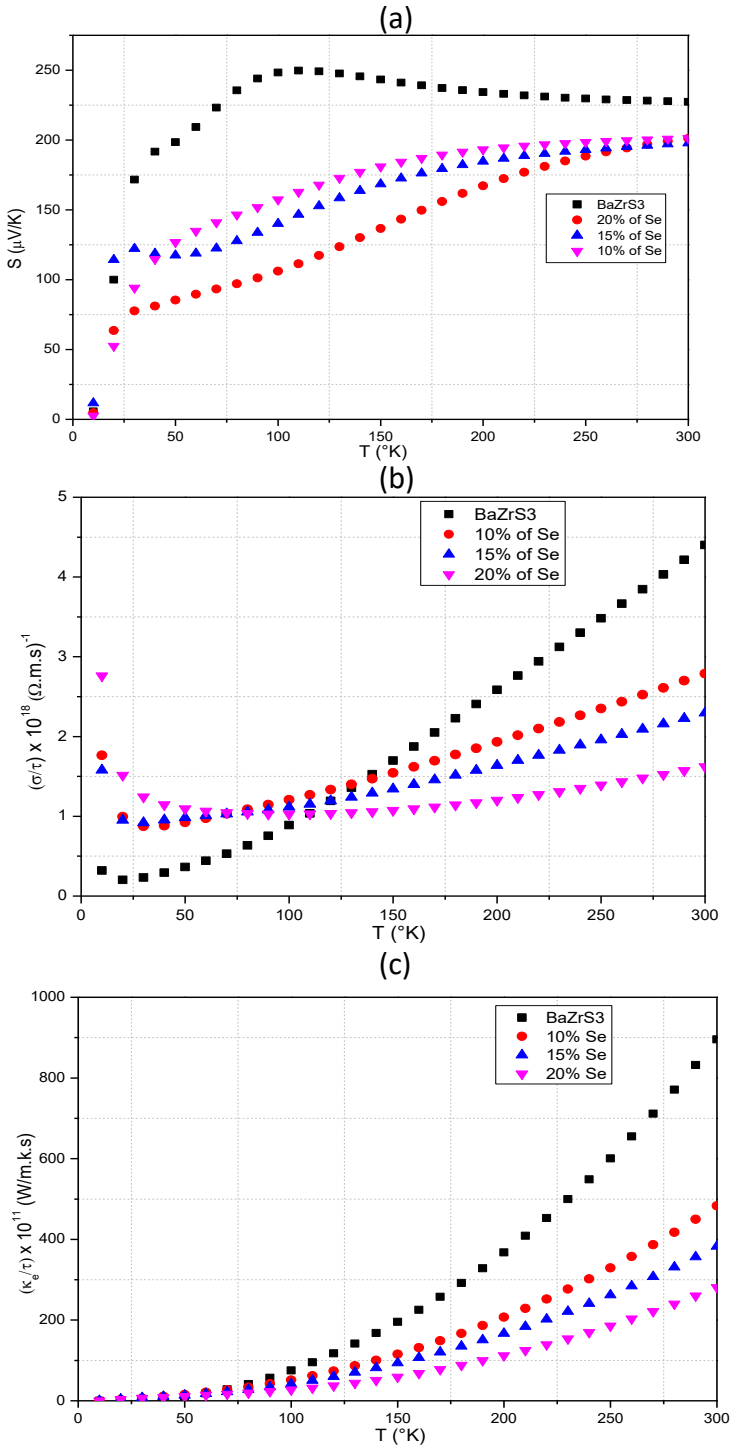

Figure IV.5**:** The transport properties of $BaZrS_3$ doped with Se: (a) Seebeck coefficient; (b) the electrical conductivity; (c) electronic thermal conductivity.

Chapter V

Theoretical calculations of Halide Perovskites ABX_3 (X: Br, Cl or I)

V.1 INTRODUCTION

In the fifth chapter of this thesis, we present a theoretical investigation of electronic, structural, and optical properties of $CsPbX_3$,

First in section V.2, we interested on the study of $CsPbX_3$ compounds, we determine the structural, electronic and optical properties of the bulk $CsPbX_3$ (X = Br, Cl and I) are studied, using density functional theory (DFT). In order to use these compounds in photovoltaic applications, the only inconvenient of these materials is that they have a slightly high gap energy value such as : 2.57 eV, 2.16 eV and 1.88 eV for $CsPbCl_3$, $CsPbBr_3$ and $CsPbI_3$ compounds, respectively. It is known that the efficiency of the solar cells varied with the band gap of the materials used. Moreover, by applying 3% of strain on the perovskite $CsPbX_3$, we have reducing the gap energy value of these materials.

Second in section V.3, we applied a different percentage of Iodine doping in $CsPbBr_{3-x}$ (x=0%, 22% and 33% of I) to reduce the gap value. The electronic and optical properties of this compound are investigated using ab initio calculation for several concentration of I.

V.2 Study of $CsPbX_3$ compounds

V.2.1 Introduction

Solar energy become one of the most attractive renewable energy sources across the globe. It is an alternative energy source that can replace the conventional energy resources and satisfy our energy needs [169], we have a variety of solar technology, and one of the most utilized its photovoltaic, which produce electricity directly from the sunlight with minimum losses and greenhouse gas emission [170]. The photovoltaic technologies are classified into three generation of cells, the first one is wafer-based, second generation conventional thin film (copper indium selenide (CIS), cadmium telluride, etc), third generation emerging thin film (quantum dot PV, organic PV and perovskite), currently Silicon-based solar panels are the most used panels in the market (almost 90% of the market), followed by the cadmium-based panels, but this domination will be reduced with the appearance of new generation of panels based on perovskite [171]. The Perovskite is a naturel mineral of calcium titanate ($CaTiO_3$) [172], in addition, the general chemical formula is ABX_3 where: A cation is encircled by twelve of X anions in dodecahedral environment, the B cations is octahedral coordinated by 6

X anions and the X anions are coordinated by 4 A cations and 2 B cations, we describe the perovskite structure by a three-dimensional cubic network of corner-sharing BX6 octahedra, while A cations is situated at the corner of the cube [173], we can have another structures with a lower symmetric phase such as tetragonal or orthorhombic by partially distorting the BX6 octahedral. One of the factors that allowed materials scientists to be interested in perovskite because it's abundantly available in nature [174], and due to their versatile applications in transistors [175], light-emitting diodes [176], optics [177], magnetics [178], electronics [179], and superconductors [180], and specially as a solar cell for photovoltaic [181-183]. Perovskite has the ability to absorb light and uses less than 1 μm of material to capture the same amount of sunlight as other solar cells, and it's a semiconductor used to carry electric charge whenever light hits the material. Perovskite-based solar cells are considered to be one of the most remarkable cells in terms of efficiency. Therefore, researchers have shown considerable interest for perovskite solar cells. Flexibility, lightness and semi-transparency are part of the precious proportion of perovskite [184], and the efficiency of the perovskite-based solar cells has demonstrated unprecedented, rising from 3.8% to nearly 23% between 2009 and 2018 [185,186]. Moreover, the hybrid organic-inorganic perovskite (HOIP) characterized by his different properties like optical, electronic, magnetic properties which can be applied in different applications, the structure of this materials can be described in general by a formula ABX_3, where A is an organic ammonium cation ($CH_3NH_3^+$, $NH = CHNH_3^+$, etc.), B is a divalent metal cation (Fe^{2+}, Cd^{2+}, Pb^{2+}, Cu^{2+}, Sn^{2+}, etc.), and X is a halide ions (Br^-, Cl^-, or I^-). In the recent year HOIP have substantial attraction in the solar cell applications [187, 188]. The first three-dimensional (3D) organic-inorganic hybrid solar cell was generated by Weber [189, 190] which replaced cesium (Cs) with methylammonium (CH_3NH_3) cations. Hybrid organic-inorganic perovskite show good light absorption and semiconducting properties, which allows them to be good applicant for opto-electronic devices applications especially in photovoltaic with efficiency beyond 20% [191, 192]. Furthermore, the perovskite cesium lead

halides, with the general formula $CsPbX_3$ (X= Br, Cl, I) are direct band gap semiconductors that absorb ultraviolet and visible light, therefore these materials are used in optoelectronic and photovoltaic devices such as solar cells, photonic crystals [193, 194], radiation detectors [195], and light emitting diodes (LEDs) [196, 197]. These compounds are characterized by their flexibility to change the structure at different temperatures [198], according to Moller [199] who studied the structural properties of $CsPbX_3$ (X= Br, Cl, I), he indicates that $CsPbX_3$ exist in three different phases. The phase transition of this compounds depends on the temperature, $CsPbBr_3$ is in the orthorhombic phase at room temperature, change to tetragonal structure at 373 K and the last transition is the cubic phase at 403 K [200, 201], for $CsPbCl_3$ below 315 K, it is in the orthorhombic phase, in the tetragonal structure in the range of 315 K to 320 K and in the cubic phase above 320 K [200,202], $CsPbI_3$ appears in the orthorhombic structure at room temperature [203], then goes to the tetragonal phase but there is no clearly defined temperature range in the literature and at 634 K it becomes a cubic structure.

We started this work by studying the structural, optical and electronic properties of the bulk $CsPbX_3$ (X = Br, Cl, I) using density functional theory (DFT), in order to use them in photovoltaic applications. These compounds are direct gap materials with a high visible light absorption and low reflectivity, which allowed them to be good candidate for solar cells, the only inconvenient of these compounds is that they have a slightly high gap value such as: , 2.57 eV, 2.16 eV and 1.88 eV for $CsPbCl_3$, $CsPbBr_3$ and $CsPbI_3$, respectively. It is known that the efficiency of the solar cells varied with the band gap of the materials used. Thus in this work we focused on reducing the gap value of these materials, by applying different stress value from 0 to 3% for the three compounds.

- ## COMPUTATIONAL METHODS

In this work all calculations are based on the density functional theory (DFT), the solution of Kohn-Sham equations are obtained by using Wien2k ab initio simulation program [204]. We determined the exchange and correlation effects by a generalized gradient approximation of

Perdew−Burke−Ernzerhof for solid (GGA-PBE). The electronic and optical properties have been calculated in stable cubic phase for the three compounds which conforms to Pm3m space group. In these calculations we had a 6×6×6 Monkhorst−Pack set of k-point mesh of Brillouin zone integration generated automatically, the $R_{mt}*K_{max}$ value was fixed to 7 (R_{mt} present the small atomic radius in the unit cell, while K_{max} present the size of the largest vector in the plane wave expansion) [204].

V.2.2 Bulk $CsPbX_3$ calculation

V.2.2.1 structurals properties

$CsPbX_3$ (X= Br, Cl and I) perovskite with Pm3m space group have a structure with one atom of cesium, one atom of lead and three of Bromine, Chlorine or Iode as showing in **Figure V.1**. The calculated and experimental lattice parameters are given in **Table V.1**. We used the experimental lattice parameters to do the optimization. As a result of our calculation from the standard DFT calculation we obtained results close to experimental lattice with an error of 1.9% for $CsPbBr_3$, 2% for $CsPbCl_3$ and 1.4% for $CsPbI_3$.

Table V.1: Comparison between experimental and theoretical results .

	$CsPbBr_3$		$CsPbCl_3$		$CsPbI_3$	
Lattice parameters	a (Å)	V ($Å^3$)	a (Å)	V ($Å^3$)	a (Å)	V ($Å^3$)
Present work	5.987	214.493	5.725	187.680	6.289	248.787
Experiment [205]	5.870	202.262	5.605	176.087	6.380	259.670

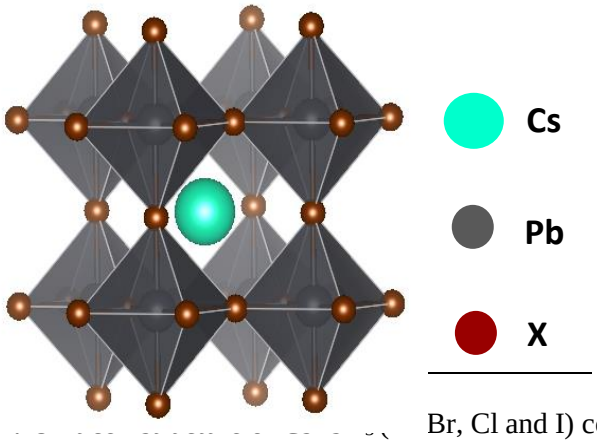

Figure Br, Cl and I) compound.

V.2.2.2 Electrical properties

The calculated band structure of $CsPbX_3$ using GGA-PBE density functional approximations is shown in **Figure V.2**. The Fermi level is fixed to zero at the top of the valence band. The maximum of the valence band and the minimum of the conduction band are located at the M point, which indicates that the $CsPbX_3$ is direct band gap materials with the value of about 2.16 eV for $CsPbBr_3$ (see **Figure V.2.a**), 2.57 eV for $CsPbCl_3$ (see **Figure V.2.b**) and 1.88 eV for $CsPbI_3$ (see **Figure V.2.c**).

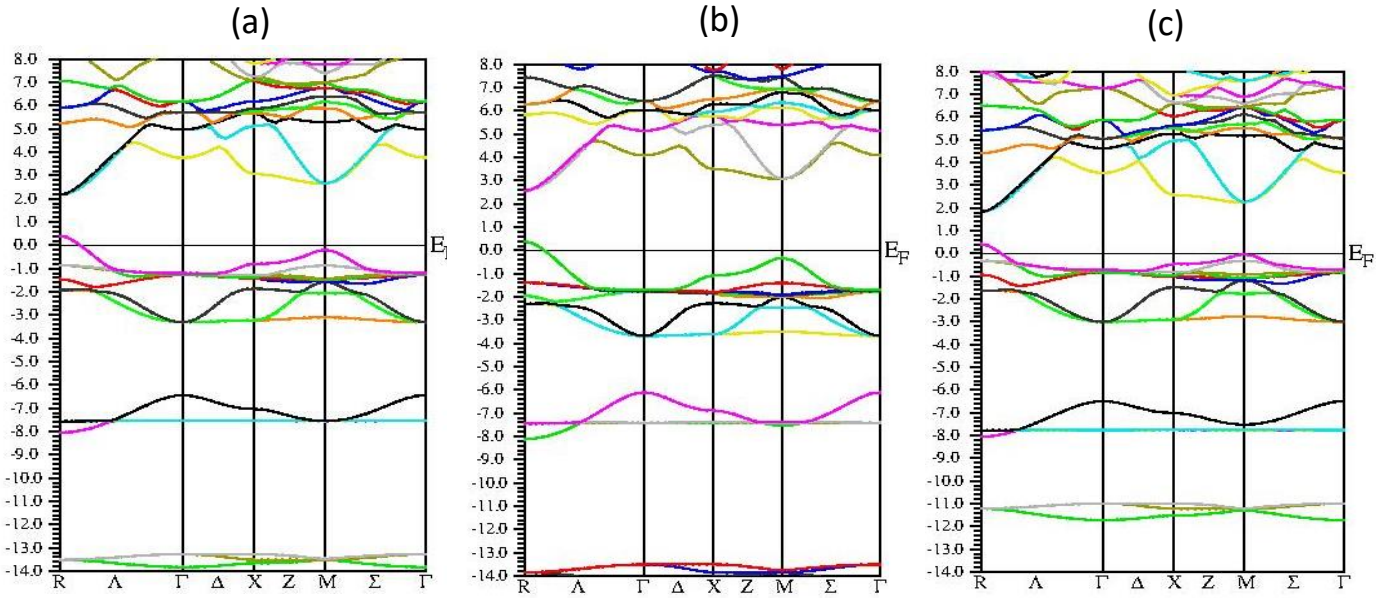

Figure V.2: Band structure of $CsPbX_3$: a) $CsPbBr_3$ b) $CsPbCl_3$ c) $CsPbI_3$.

The total (DOS) and partial (PDOS) density of state of $CsPbX_3$ perovskite compound are shown in **Figure V.3**. We observe that in the entire range Cs and Pb states hybridize with Br for $CsPbBr_3$, with Cl for $CsPbCl_3$ and with I for $CsPbI_3$, inclusive of the conduction and valence bands, which indicate that Cs-Br, Pb-Br, Cs-Cl, Pb-Cl, Cs-I and Pb-I bonding are principally covalent. In addition, the electron charge was transferred from Cs and Pb to Br for $CsPbBr_3$, to Cl for $CsPbCl_3$ and to I for $CsPbI_3$ due to the large difference between states, revealing the ionic bonding characteristic, see Figure V.**3(a)**, **3(c)** and **3(e)**. From **Figure V.3.b**, we notice that the band energy between -5 and 0 eV mainly consist of Br (4p) and Pb (5d), the valence band with a width of 3.54 eV is consisting of Br (4p), with small but no negligible contributions from Pb and Cs states. The conduction band is consisting of Cs (4d) Pb (6p) Br (3d). From **Figure V.3.d**, we notice that the band energy between -5 and 0 eV mainly consist of Cl (3p) and Pb (6p), the valence band with a width of 3.67 eV is consisting of Cl (3p), with small but no negligible contributions from Pb and Cs states. The conduction band is consisting of Cs (4d) Pb (6p) Cl (3p). From **Figure V.3.f**, we notice that the band energy between -15 and 0 eV mainly consist of Cs (5p), I (5s) and Pb (4f), the valence band with a width of 3.07 eV is consisting of I (5p) and Pb (6p) , with small but no negligible contributions from Cs state. The conduction band is consisting of Cs (4d) Pb (6p) I (4d).

(a)

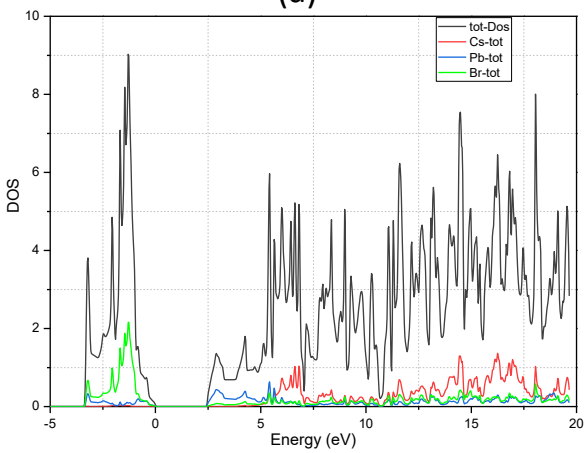
tot-Dos
Cs-tot
Pb-tot
Br-tot
DOS
Energy (eV)

(b)

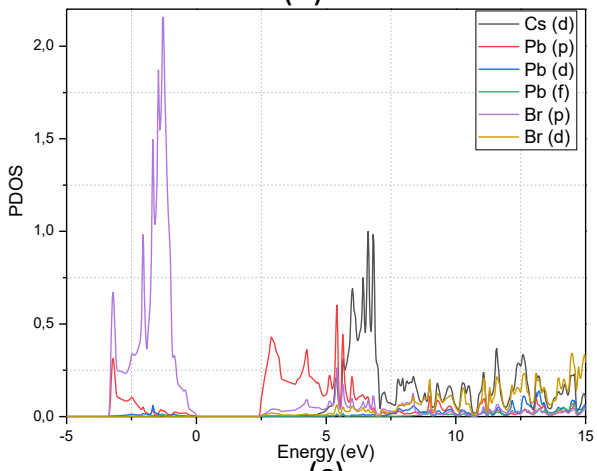
Cs (d)
Pb (p)
Pb (d)
Pb (f)
Br (p)
Br (d)
PDOS
Energy (eV)

(c)

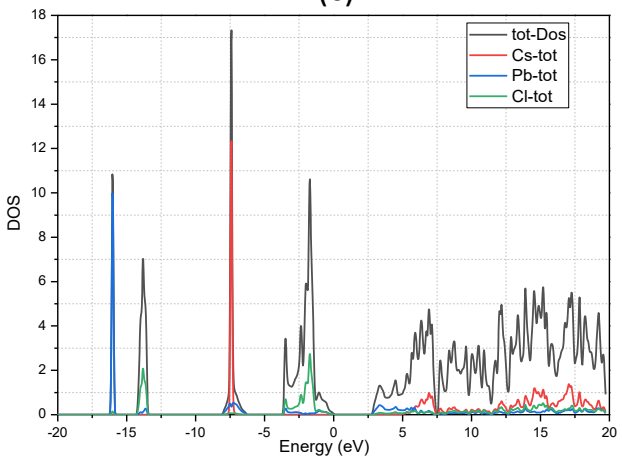
tot-Dos
Cs-tot
Pb-tot
Cl-tot
DOS
Energy (eV)

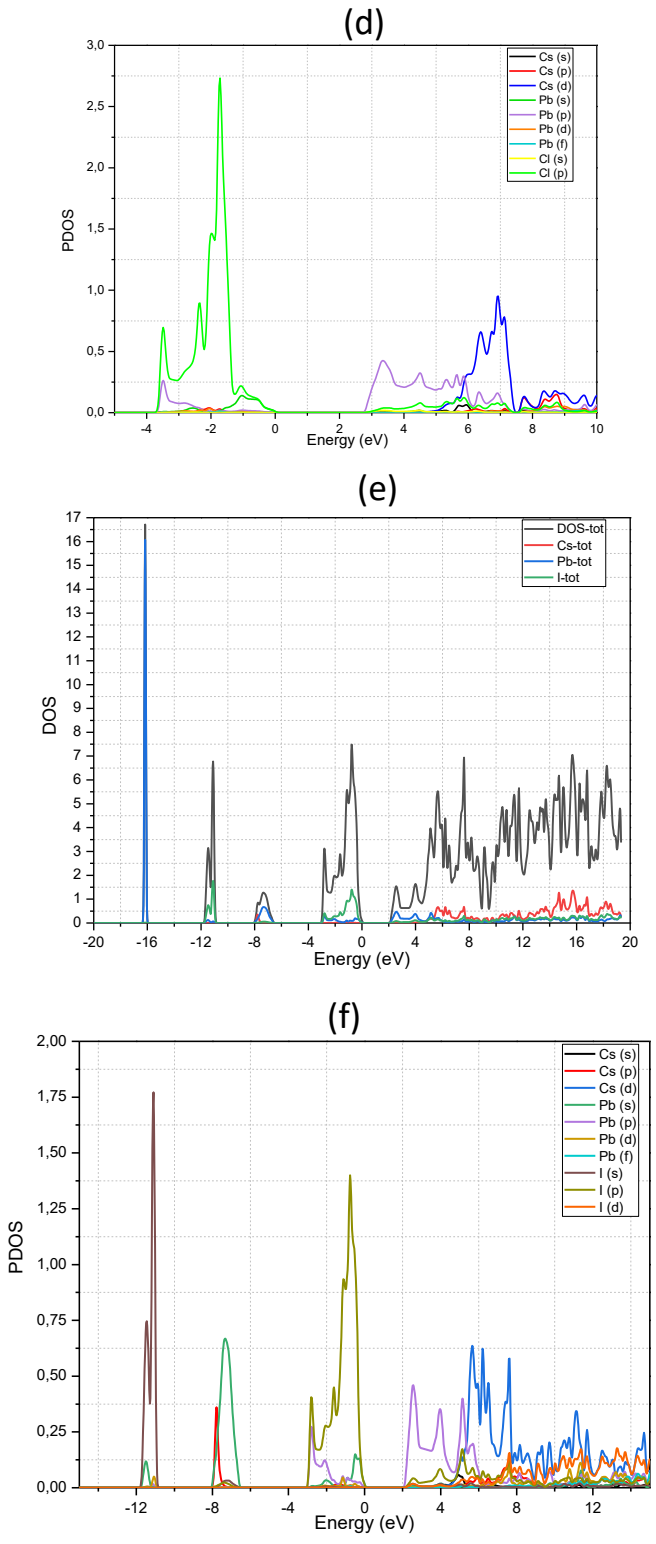

Figure V.3: Total DOS and Partial DOS of $CsPbX_3$: a and b) $CsPbBr_3$, c and d) $CsPbCl_3$, e and f) $CsPbCl_3$.

V.2.2.3 Optical properties

To connect the electronic structures of a solid to the microscopic physical transitions between bands, we use the dielectric function. To calculate the complex part of this function we used the same previous methods.

$$\varepsilon(\omega) = \varepsilon_1(\omega) + i\,\varepsilon_2(\omega) \qquad \text{(V.1)}$$

where ε_2 and ε_1 are respectively the imaginary and real part of the dielectric function, we can determine the real part from the imaginary part using the Kramer-Kronig relations. We can calculate the imaginary part by:

$$\varepsilon_1(\omega) = 1 + \left(\frac{2}{\Pi}\right) d\omega' \frac{\omega'^2 \varepsilon_2(\omega')}{\omega'^2 - \omega^2} \qquad \text{(V.2)}$$

$$\varepsilon_2(\omega) = \frac{2\Pi e^2}{\Omega \varepsilon_0} \sum_{k,v,c} |\langle \Psi^c{}_k | u.r | \Psi^v{}_k \rangle|^2 \, \delta(Eck - Evk - h\omega) \qquad \text{(V.3)}$$

where c and ν are the conduction and valence band, $\Psi^{\nu}{}_k$ and $\Psi^{c}{}_k$ are the wave function of valence and conduction band at k point, ε_0 is the vacuum dielectric constant, Ω is the volume, hω is the energy of the incident phonon, u is the vector defining the polarization of the incident electric field, u.r is the momentum operator.

From the real and imaginary part of the dielectric function we can determine all the optical proprieties such as the absorption α (ω), reflectivity *R* (ω), optical conductivity σ (ω), energy loss *L* (ω), refractive index *n* (ω) and the extinction coefficient *K* (ω).

$$\alpha(\omega) = \frac{2\omega}{c} k(\omega) \qquad \text{(V4)}$$

$$R(\omega) = \left| \frac{\sqrt{\varepsilon_1(\omega) + i\varepsilon_2(\omega)} - 1}{\sqrt{\varepsilon_1(\omega) + i\varepsilon_2(\omega)} + 1} \right|^2 \qquad \text{(V.5)}$$

$$\sigma(\omega) = -i \frac{\omega}{4\Pi} [\varepsilon 1(\omega) + i\varepsilon(\omega) \qquad \text{(V.6)}$$

$$L(\omega)=\mathrm{Im}[\frac{-1}{\varepsilon(\omega)}] \quad (V.7)$$

$$n(\omega) = \frac{1}{\sqrt{2}}\{[\varepsilon_1{}^2(\omega) + \varepsilon_2{}^2(\omega)]^{1/2}+\varepsilon_1(\omega)\}^{1/2} \quad (V.8)$$

$$K(\omega) = \frac{1}{\sqrt{2}}\{[\varepsilon_1{}^2(\omega) + \varepsilon_2{}^2(\omega)]^{1/2}-\varepsilon_1(\omega)\}^{1/2} \quad (V.9)$$

The dielectric function and all the optical proprieties are determined using GGA-PBE functional as shown in **Figure V.4**. According to the **Figure V.4.a** we notice that both the imaginary and real part of the dielectric function increased with energy and attained maximum at 3.89 and 3.01 eV for $CsPbBr_3$, 5.15 and 3.50 eV for $CsPbCl_3$ and 3.165 and 2.55 eV for $CsPbI_3$, respectively. This peak is a result of the electron transition.

The absorption coefficient α (ω) of a material allows us to determine the penetration's degree of light into the material before being absorbed. As showing in **Figure V.4.b** we observe that the absorption decreases rapidly when the wavelength (λ) increases. The maximum value of the absorption for $CsPbBr_3$ is 58.01×10^4 cm^{-1} obtained at ultraviolet light (λ=300 nm), 56.01×10^4 cm^{-1} for $CsPbCl_3$ obtained at ultraviolet light (λ=236 nm) and for $CsPbI_3$ 82.98×10^4 cm^{-1} obtained at λ =200 nm, after that we obtained another peak 57.27×10^4 at ultraviolet light (λ=340 nm). When we go over λ=300 nm, we notice a rapid decrease of the absorption as a function of λ, after that we obtain a stable value 0.19×10^4 cm^{-1} for $CsPbBr_3$, 0.14×10^4 cm^{-1} for $CsPbCl_3$ and 0.34×10^4 cm^{-1} for $CsPbI_3$ in the visible and infrared. Moreover, the refractive index n (ω) is a dimensionless size characteristic of a medium, describing the behavior of light in it, this depends on the measurement wavelength, but also the characteristics of the environment (in particular pressure and temperature). From the **Figure.4.c**, we notice that the maximum of the refractive index for $CsPbBr_3$ is 2.53 when the wavelength is equal to ~ 400 nm (visible), for $CsPbCl_3$ is 2.27 when the wavelength is equal to ~ 353 nm (visible) and for $CsPbI_3$ is 2.99 when the wavelength is equal to ~ 475 nm (visible). In the range of wavelength between 600 and 1000 nm, we observe that the refractive

index is conserved at 2.03 for $CsPbBr_3$, 1.842 for $CsPbCl_3$ and 2.32 for $CsPbI_3$. The **Figure.4.d** shows that the reflectivity R(ω) decreases with the wavelength, we observe that the highest value of reflectivity for $CsPbBr_3$ is 0.24 (24%) obtained in ultraviolet at 280 nm, for $CsPbCl_3$ is 0.19 (19%) obtained in ultraviolet at 239 nm and for $CsPbI_3$ is 0.29 (29%) obtained in ultraviolet at 346 nm. The reflectivity decreases as a function of λ. We notice that the reflectivity stabilizes at 0.115 for $CsPbBr_3$, 0.09 for $CsPbCl_3$ and 0.15 for $CsPbI_3$ in the visible and infrared.

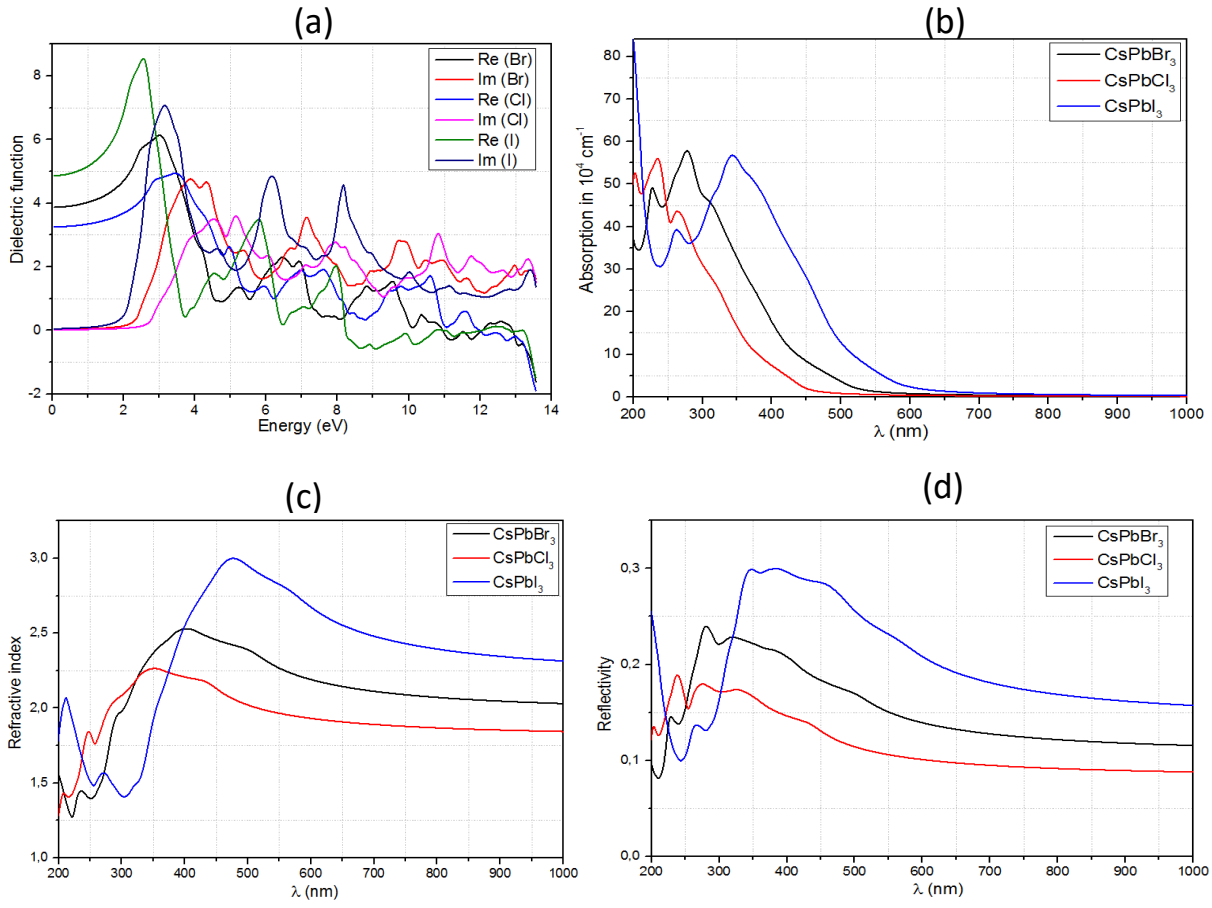

Figure V.4: Optical properties of $CsPbX_3$: a) The dielectric function, b) absorption, c) refractive index and d) reflectivity.

V.2.3 The effect of strain on $CsPbX_3$ compounds

V.2.3.1 Electrical properties

We applied the strain to the cubic structure of $CsPbBr_3$ compound along the axis z, and we determined the volume of each percentage (%) to determine the effect of the pressure on the CsPbBr3 properties. The **Table V.2** allows us to determine the pressure, the volume, the c parameter and the band gap energy of each percentage of strain (%). From this table it is found that the pressure decrease with increasing the volume. Moreover, The value of the gap energy decrease when increase the stain, and as we can see the gap decrease from 2.16 eV (0%) up to 1.87 eV (3%), 2.57 eV (0%) up to 2.28 eV (3%) and 1.88 eV (0%) up to 1.60 eV (3%) for $CsPbBr_3$, $CsPbCl_3$ and $CsPbI_3$, respectively (see **Table V.2**). We observed that the two compounds $CsPbBr_3$ and $CsPbI_3$ perovskite can be considered a good candidate for photovoltaic applications.

Table V.2: Strain effect on pressure, volume, c parameter and band gap energy.

	$CsPbBr_3$				**$CsPbCl_3$**				**$CsPbI_3$**			
Strain (%)	0	1	2	3	0	1	2	3	0	1	2	3
Pressure (GPa)	0	0.17	0.40	0.63	0	0.09	0.35	0.62	0	0.13	0.29	0.49
Volume (Br^3)	1450.99	1436.48	1421.97	1407.46	1266.52	1253.85	1241.18	1228.52	1752.31	1734.79	1717.26	1699.74
Value of c (Br)	11.32	11.20	11.09	10.98	10.81	10.71	10.60	10.49	6.37	6.31	6.25	6.18
Band Gap (eV)	2.16	2.11	2.06	1.87	2.57	2.52	2.46	2.28	1.88	1.84	1.79	1.60

The calculated band structure of $CsPbX_3$ (X=Br, Cl and I) with strain is shown in **Figure V.5**. The Fermi level is fixed to zero at the top of the valence band. The maximum of the valence band and the minimum of the conduction band are located at the M point, which indicates that the $CsPbX_3$ with different strain value are direct band gap materials, whereas, the band gap

energy values are about 1.87 eV, 2.28 eV and 1.60 eV for $CsPbBr_3$ $CsPbCl_3$ and $CsPbI_3$, respectively, at 3% of strain (see, **Figure V.5**).

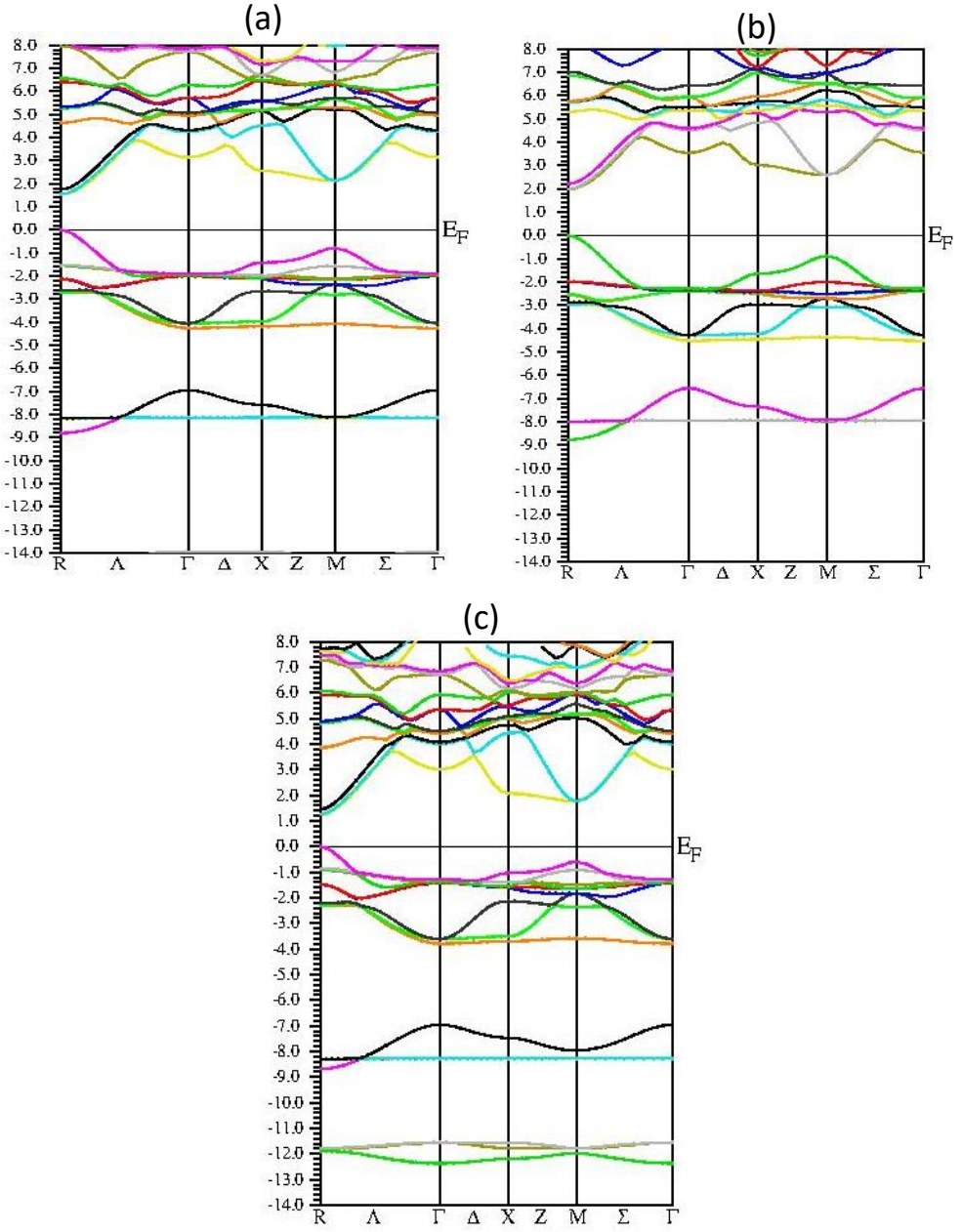

Figure V.5: Band structure of $CsPbX_3$ compound with 3% of strain: a) $CsPbBr_3$, b) $CsPbCl_3$ and c) $CsPbI_3$.

V.2.3.2 Optical properties

Furthermore, we have calculated the energy dependent optical properties including dielectric function, absorption coefficient, reflectivity and refractive index using DFT within the GGA-PBE functional for different strain values, see **Figures V.6, 7 and 8**. The energy dependent

dielectric function can be written by Eq. (1). In **Figures V.6a, 7a and 8a**, it is found that the real (ε_1) and imaginary (ε_2) parts of the dielectric function increase with increasing the energy, and attained a maximum value at (2.99 eV and 4.39 eV), (3.44 eV and 5.15 eV) and (2.54 eV and 3.19 eV) for $CsPbBr_3$, $CsPbCl_3$ and $CsPbI_3$, respectively. The observed peak (maximum dielectric value) is due to the electron transition. These values are obtained for 1% of strain. We notice that the strain effect on dielectric function is negligible. **Figures V.6b, 7b and 8b,** we shown that the absorption coefficient decreases rapidly in visible region when increasing the wavelength (λ). When increasing the strain value, the absorption coefficient of $CsPbX_3$ (X= Br, Cl and I) compound increase in visible region, this is very important for photovoltaic application. Moreover, in **Figures V.6c, 7c and 8c** it is clear that the reflectivity decreases with increasing the wavelength (λ) in visible range. We observed that for different strain values, the reflectivity stabilizes in the visible range for CsPbX3 (X= Br, Cl and I) compound. Finally, from the **Figures V.6d, 7d and 8d**, the maximum values of the refractive index are 2.53, 2.26 and 3.01 for $CsPbBr_3$, $CsPbCl_3$ and $CsPbI_3$, respectively, when the wavelength is in the range 380-550 nm. After this range, we observe that the refractive index is conserved for different value of strain.

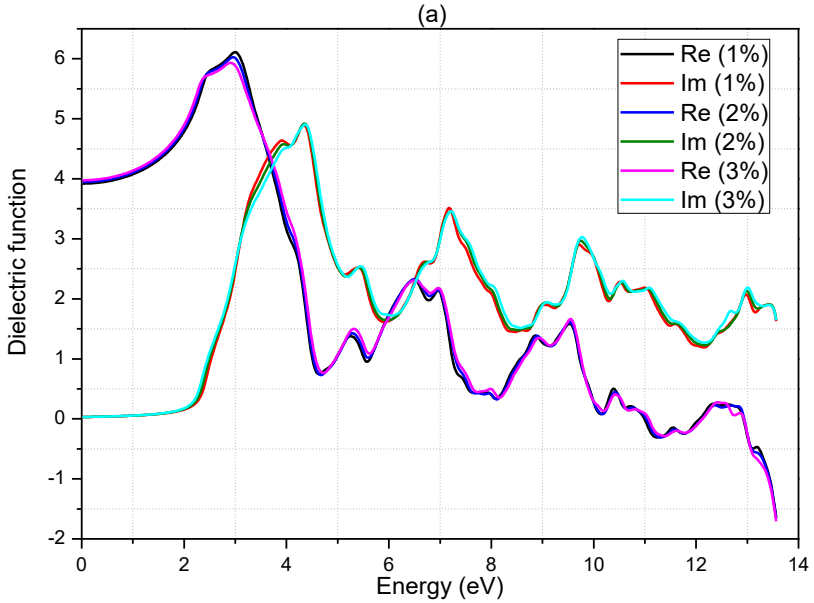

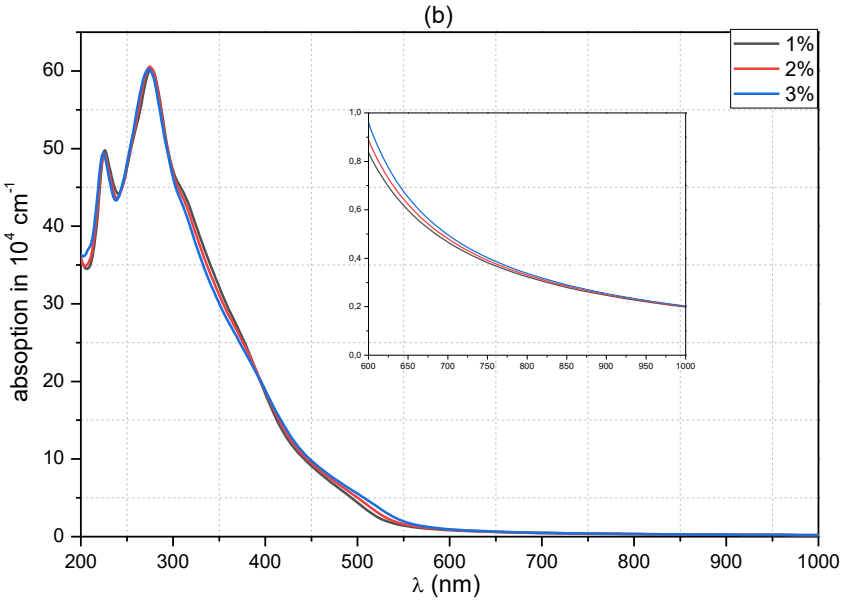
(b)
1%
2%
3%
absoption in 10^4 cm^{-1}
λ (nm)

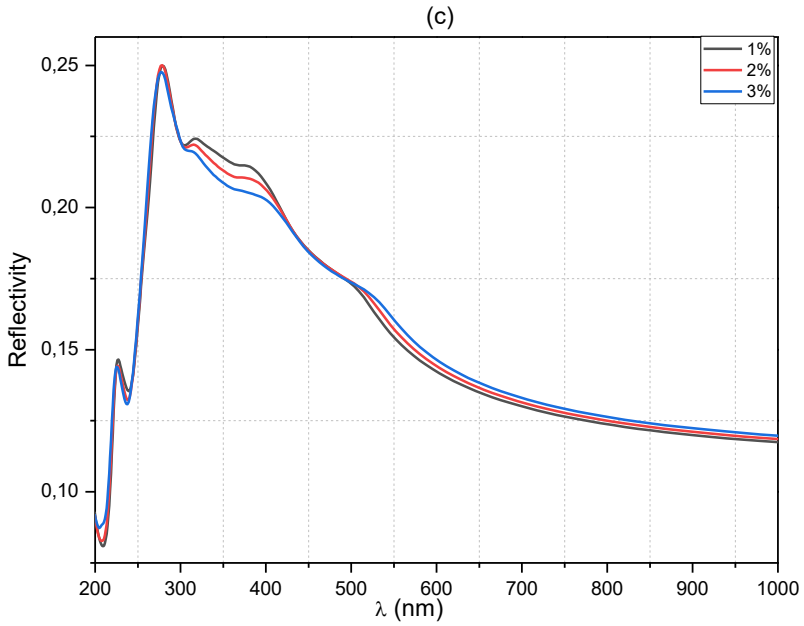
(c)
1%
2%
3%
Reflectivity
λ (nm)

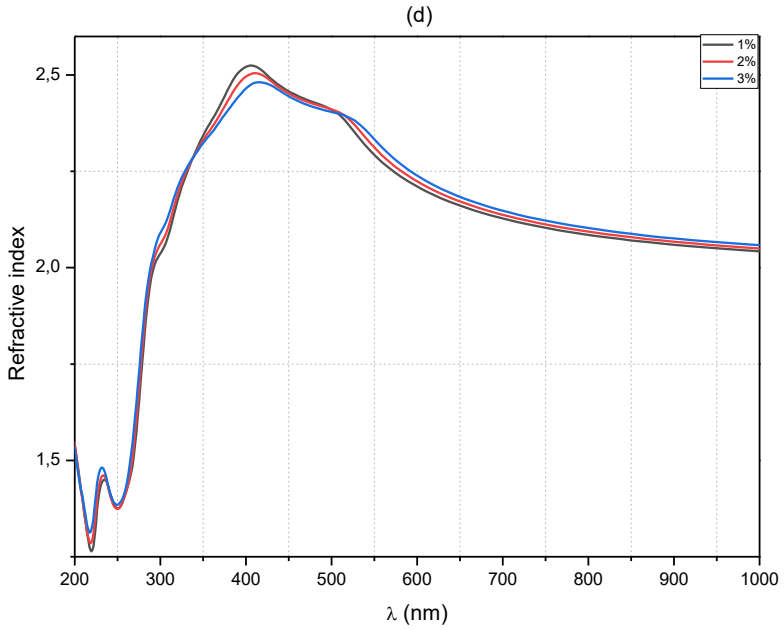

Figure V.6: a) Dielectric function, b) absorption, c) reflectivity and d) refractive index of $CsPbBr_3$ compound for different values of strain.

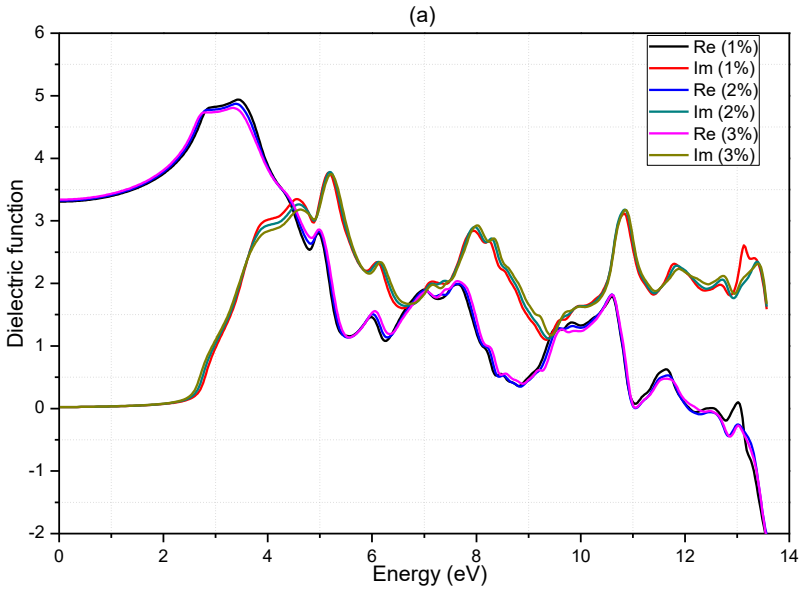

(b)

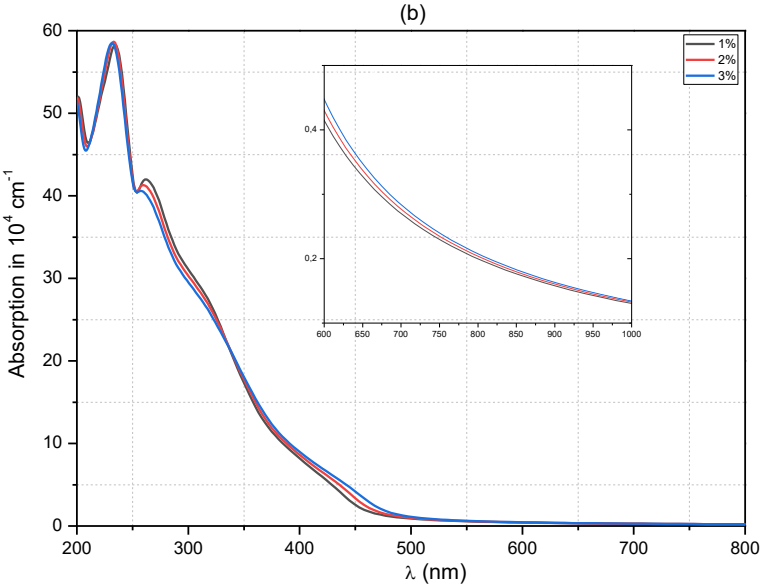

(c)

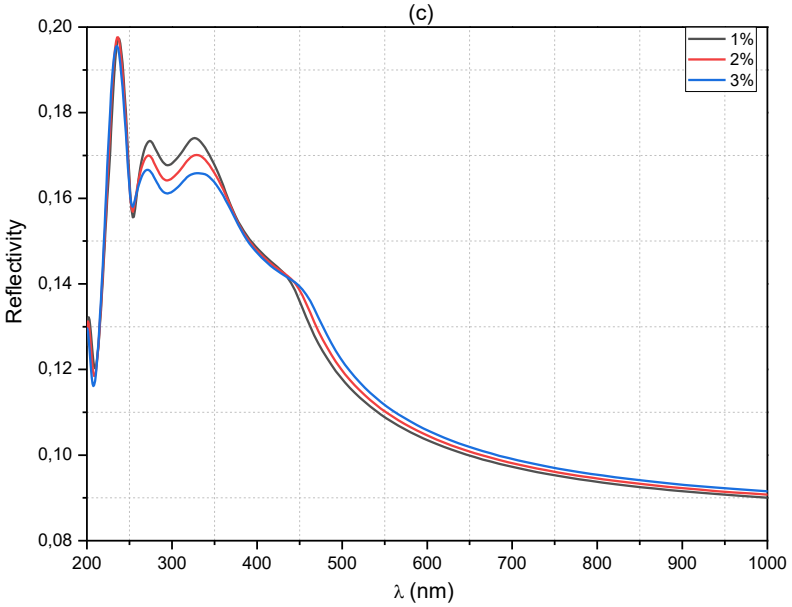

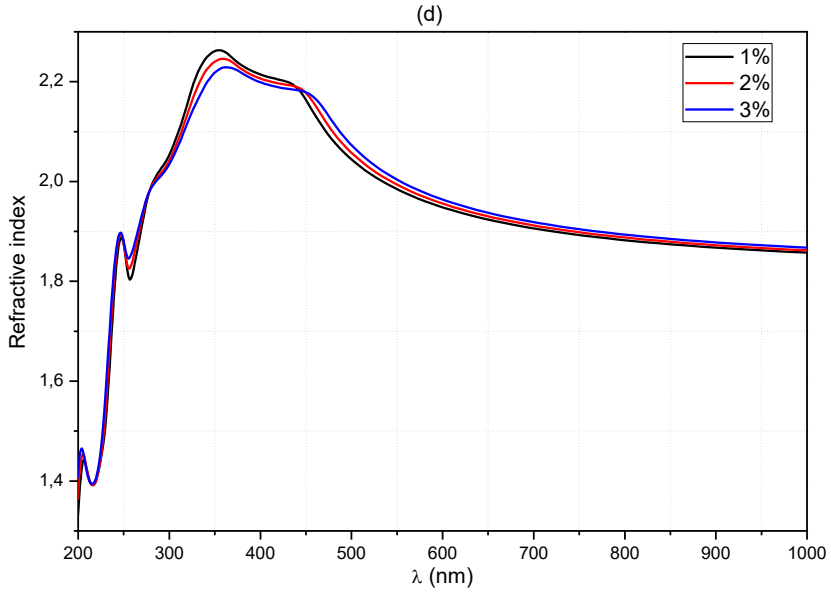

Figure V.7: a) Dielectric function, b) absorption, c) reflectivity and d) refractive index of $CsPbCl_3$ compound for different values of strain.

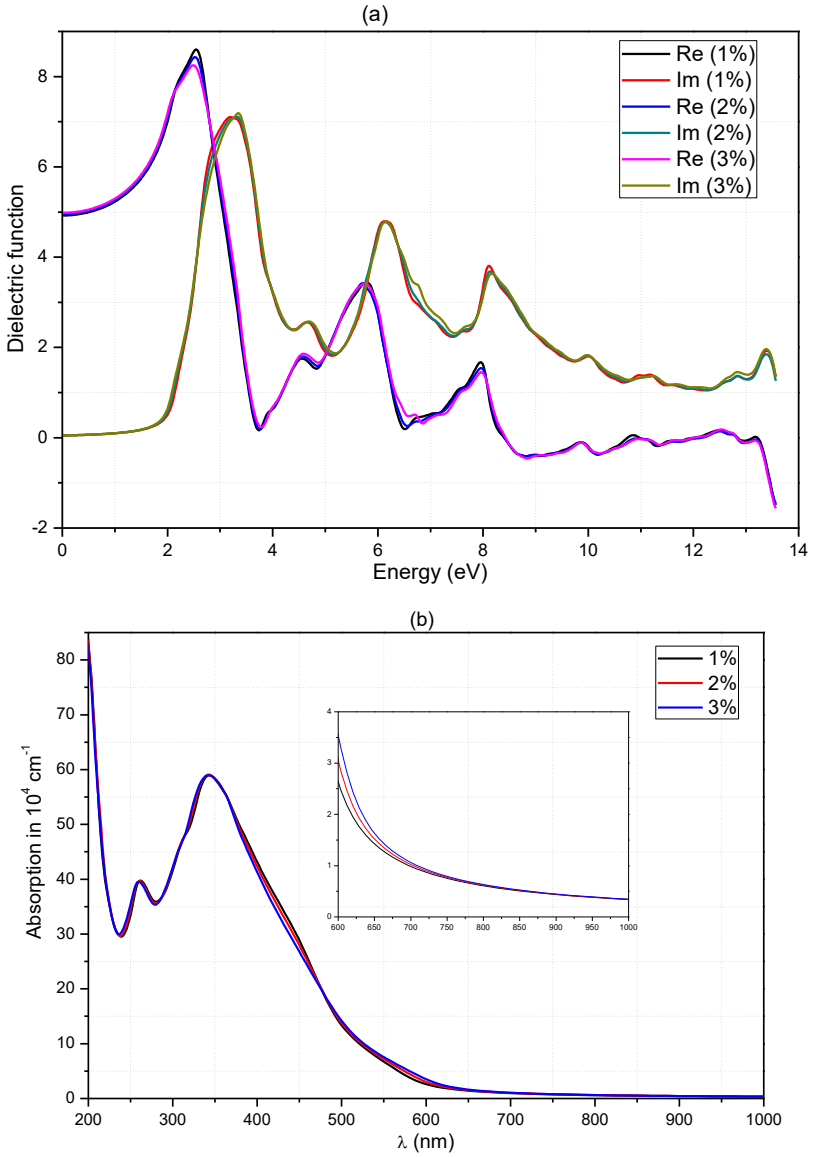

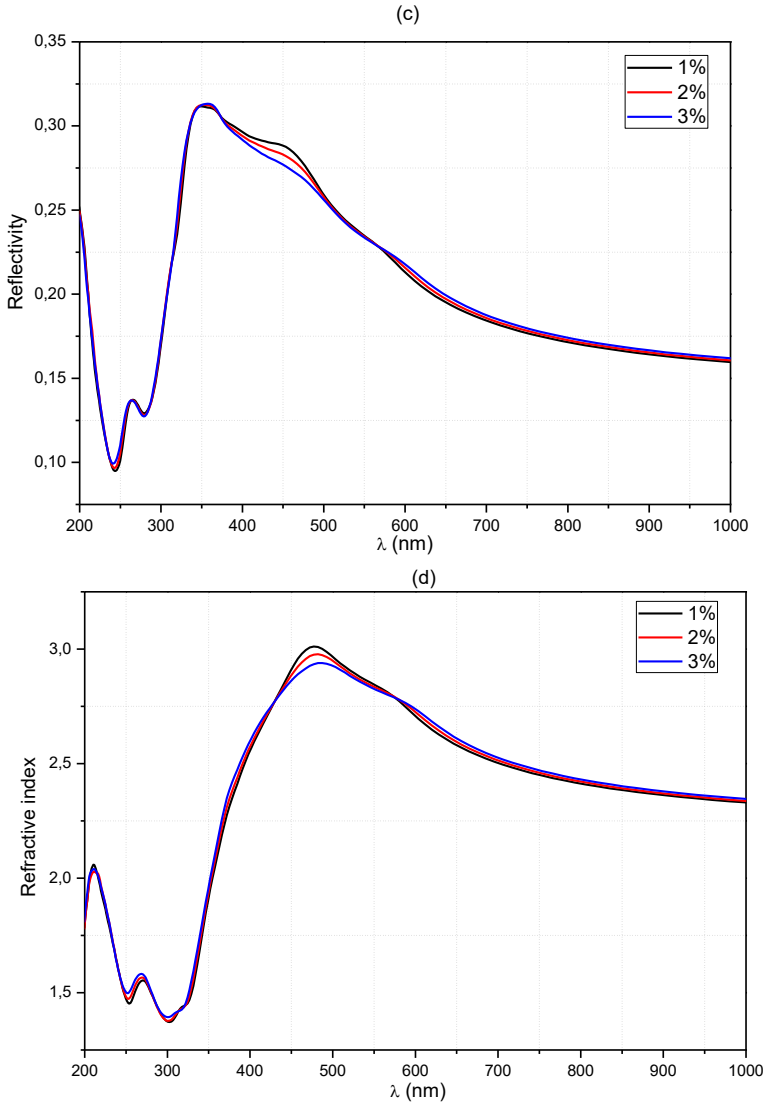

Figure V.8: a) Dielectric function, b) absorption, c) reflectivity and d) refractive index of $CsPbI_3$ compound for different values of strain.

V.3 Doping effect on $CsPbBr_3$

V.3.1 Introduction

Photovoltaic technologies experienced a great development these last years due the new generation of absorbent materials based on halide perovskite, that showing a rapid increase of the power conversion efficiency (PCE) from 3.8% in 2009 [206] to now over 22% [207]. This development is due to the outstanding properties of halide perovskite presenting high absorption coefficient, high charge carrier motilities, a equilibrate electron and hole transport and direct band gap. Theoretically the PCEof the halide perovskite can reach 31% [208] but the experimental study is still rather far away from this number and it is still difficult to

improve the PCE of these perovskite solar cells because of different issues, the major issue that should be resolved is the poor environmental stability which is related to the crystallization properties of the perovskite layers and the interfacial charge transfer.

The organic-inorganic halide perovskite with the composition ABX_3 where A is ($CH_3NH_3^+$, $CH(NH_2)_2^+$) for the organic cation and (Cs^+, K^+, Rb^+) for the inorganic cation, B is (Fe^{2+}, Cd^{2+}, Pb^{2+}, Cu^{2+}, Sn^{2+}, etc.) and X is a halide ions (Br^-, Cl^-, or I^-), have a PCE close to the commercial silicon, but the constraints that prevents the commercialization of halide-based perovskite-based solar cells are the chemical instability under ambient conditions, the toxicity, the stability for the organic halide perovskite and the probable carcinogenicity of lead and lead halides [209-211].

In recent years, scientists have given great interest to lead halide perovskite $CsPbBr_3$ because of its diverse applications in different fields, as promising light emitters for light-emitting diodes (LEDs) [212,213], photocatalysis [214,215], photodetector [216,217] and especially as absorber for photovoltaic [218-220]. Cesium lead bromide ($CsPbBr_3$) is characterized by its flexibility to change the structure at different temperatures, according to Moller [221], who studied the structural properties of CsPbX3 (X = Br, Cl, I). He demonstrated that $CsPbBr_3$ exists in three different phases. We have the orthorhombic phase at room temperature, when the temperature is equal to 373 K, the phase changes to tetragonal and the last transition is the cubic phase at 403 K [222-223].

The variety of CsPbBr3 properties allows it to be one of the most promising materials for photovoltaic application with a PCE reaches 20.46% [224] and good stability of solar cells, but the inconvenience is the value of the band gap.

The aim of our work is to reduce the value of the gap by applying different percentage of doping using I atoms $CsPbBr_{3-x}I_x$ with (x=22% and 33%). We calculate electrical and optical properties using ab initio. As a result the gap value reduces from 2.16 eV for the bulk

$CsPbBr_3$ to 1.43 eV corresponding to 33% of I. Also, the I atoms improve the absorption coefficient at the visible light and shows a peak corresponding to 33% of I.

- **Computational Methods**

In this work all calculations are based on the density functional theory (DFT), the solution of Kohn-Sham equations are obtained by using Wien2k ab-initio simulation program. We determined the exchange and correlation effects by a generalized gradient approximation of Perdew−Burke−Ernzerhof for solid (GGA-PBE) and we used the GGA-MBJ approximation to improve the gap value. In other work ABO_3 perovskites are calculated by means of the hybrid exchange-correlation functional B3LYP and found to be in an excellent agreement with experiments [225,226]. The electronic and optical properties have been calculated in stable cubic phase for the three compounds which conforms to Pm3m space group.

In these calculations we had a 6×6×6 Monkhorst−Pack set of k-point mesh of Brillouin zone integration generated automatically, the $R_{mt}*K_{max}$ value was fixed to 7 (R_{MT} present the small atomic radius in the unit cell, while Kmax present the size of the largest vector in the plane wave expansion).

V.3.2 Electrical properties

According to **Figure V.9,** we notice that Cs and Pb states hybridize with Br and I in the entire range, inclusive of the conduction and valence bands, which indicate that Cs-Br, Pb-Br, Cs-I and Pb-I bonding are principally covalent. In addition, the electron charge was transferred from Cs and Pb to Br and I, this is due to the large difference between states, revealing the ionic bonding characteristic. From **Figure V.9.a** we observe that the length of the valence band is 3.43 eV, however, from **Figure V.9.b** we see that length of the valence band is 4.12 eV and from **Figure V.9.c** we observe that the length of the valence band is 4.33 eV.

(a)

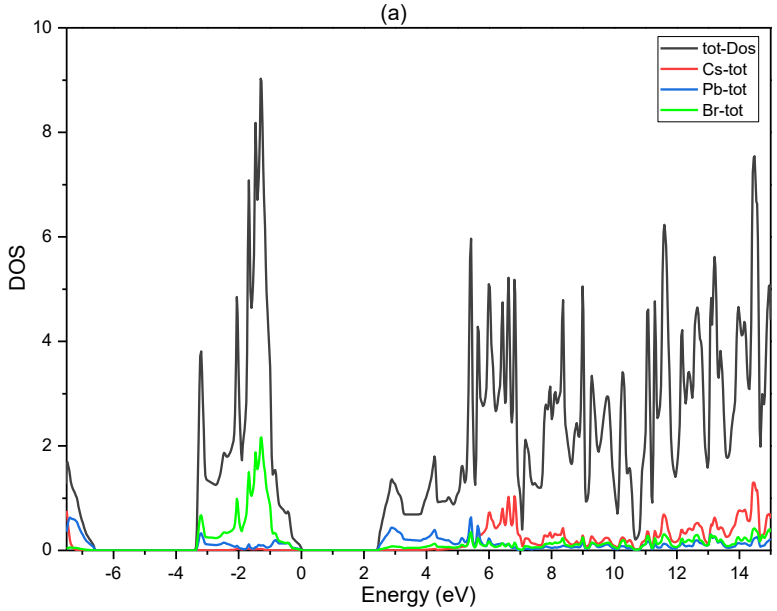
tot-Dos
Cs-tot
Pb-tot
Br-tot
DOS
Energy (eV)

(b)

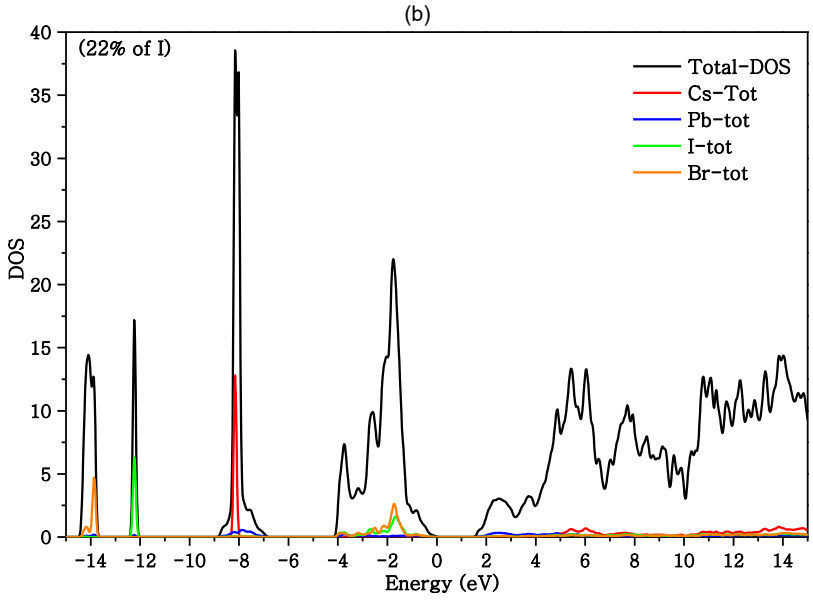
(22% of I)
Total-DOS
Cs-Tot
Pb-tot
I-tot
Br-tot
DOS
Energy (eV)

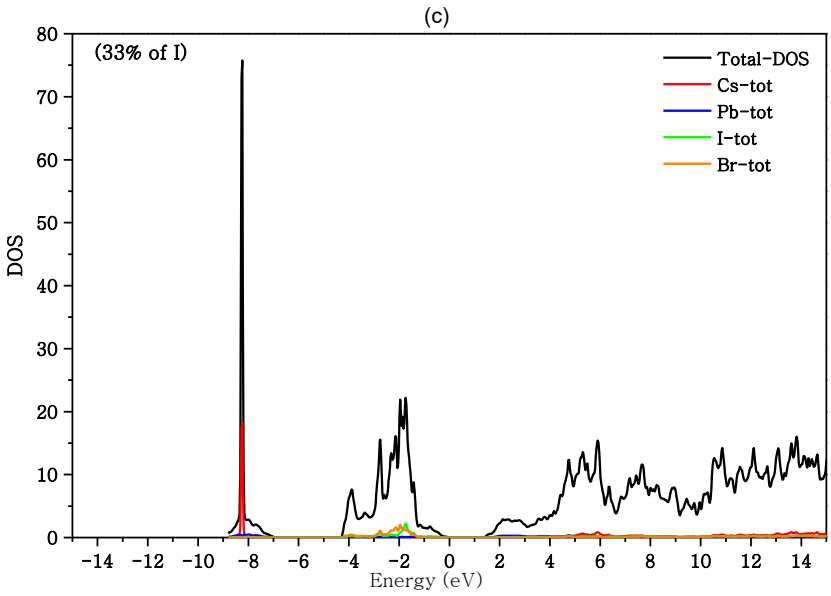

Figure V.9. Total DOS and PDOS of $CsPbBr_3$ doped with Iodine : a) bulk, b) 22% and c) 33%.

The **Table V.3** shows the evolution of the gap value as function of Iodine doping concentration. It is found that the gap energy decreases when increasing the doping concentration of Iodine from 2.16 eV (0%) to 1.43 eV (33%) for GGA-PBE approximation and from 2.318 eV (0%) to 1.589 eV (33%) for GGA-MBJ approximation, and similar the optical Gap decrease from 2.23 eV (0%) to 1.47 eV (33%).

Table V.3. Energy and optic gaps for different concentration of Iodine: a) 0% b) 22% and c) 33%.

	Gap energy (eV)			**Gap optic (eV)**
	Theoretical		experimental	
	GGA-PBE	GGA-MBJ		
0%	2.16	2.318	2.38 [227]	2.23
22%	1.60	1.830	-------	1.61
33%	1.43	1.589	-------	1.47

V.3.3 Optical properties

To connect the electronic structures of a solid to the microscopic physical transitions between bands, we use the dielectric function. To calculate the complex part of this function we used the same previous methods.

$$\varepsilon\,(\mathrm{w}) = \varepsilon_1\,(\mathrm{w}) + i\varepsilon_2 \qquad \text{(V.7)}$$

The ε_2 and ε_1 are respectively the imaginary and real part of the dielectric function; we can determine the real part from the imaginary part using the Kramer-Kronig relations. We can calculate the imaginary part by:

$$\varepsilon_{2(\omega)} = \frac{2\Pi e^2}{\Omega\varepsilon_0} \sum_{k,v,c} |\langle \Psi^c{}_k | u.r | \Psi^v{}_k \rangle|^2 \, \delta(Eck - Evk - h\omega) \qquad \text{(V.8)}$$

$$\varepsilon_1(\omega) = 1 + (\frac{2}{\Pi})\, \mathrm{d}\acute{\omega}\, \frac{\acute{\omega}^2 \varepsilon_{2(\acute{\omega})}}{\acute{\omega}^2 - \omega^2} \qquad \text{(V.9)}$$

The c and v are the conduction and valence band, $\Psi^v{}_k$ and $\Psi^c{}_k$ are the wave function of valence and conduction band at kpoint, ε_0 is the vacuum dielectric constant, Ω is the volume, hν is the energy of the incident phonon, u is the vector defining the polarization of the incident electric field, u.r is the momentum operator.

From the real and imaginary part of the dielectric function, we can determine the optical proprieties such as the absorption α(ω), reflectivity *R* (ω), refractive index *n* (ω) and dielectric function.

$$\alpha(\omega) = \frac{2\omega}{c} k(\omega) \qquad \text{(V.10)}$$

$$R(\omega) = \left| \frac{\sqrt{\varepsilon_1(\omega) + i\varepsilon_2(\omega)} - 1}{\sqrt{\varepsilon_1(\omega) + i\varepsilon_2(\omega)} + 1} \right|^2 \qquad \text{(V.11)}$$

$$\sigma(\omega) = -i\frac{\omega}{4\Pi}[\varepsilon 1(\omega) + i\varepsilon(\omega) - 1] \qquad \text{(V.12)}$$

$$L(\omega)=\mathrm{Im}[\frac{-1}{\varepsilon(\omega)}] \qquad \text{(V.13)}$$

$$n(\omega) = \frac{1}{\sqrt{2}}\{[\varepsilon_1{}^2(\omega) + \varepsilon_2{}^2(\omega)]^{1/2} + \varepsilon_1(\omega)\}^{1/2} \qquad \text{(V.14)}$$

$$K(\omega) = \frac{1}{\sqrt{2}}\{[\varepsilon_1{}^2(\omega) + \varepsilon_2{}^2(\omega)]^{1/2} - \varepsilon_1(\omega)\}^{1/2} \qquad \text{(V.15)}$$

The dielectric function and the optical proprieties are determined using GGA-PBE functional as shown in **Figure V.10**. According to the **Figure V.10.a** and **10.b,** we notice that both the imaginary and real part of the dielectric function increased with energy and attained a maximum value at 3.05 and 3.86eV for bulk $CsPbBr_3$, 2.37 and 3.97eV for 22% of I, 2.25 and 3.97eV for 33% of Iodine, respectively. This peak is a result of the electron transition.

The absorption coefficient α (ω) of a material allows us to determine the penetration's degree of light into the material before being absorbed. As showing in **Figure V.10.c**, we observe that the absorption decreases rapidly when the wavelength (λ) increases. The maximum value of the absorption for bulk $CsPbBr_3$ is 59.18×10^4 cm^{-1} obtained at ultraviolet light (λ=276 nm), 63.43×10^4 $cm^{-1}$for 22% of Iodine obtained at ultraviolet light (λ=295 nm), 64.45×10^4 $cm^{-1}$for 33% of I obtained at ultraviolet light (λ=296 nm). After that, we observed another peak 51.27×10^4 at ultraviolet light (λ=340 nm), 59.75×10^4 at ultraviolet light (λ=360 nm) and 63.86×10^4 at visible light (λ=386 nm) for 0%, 22% and 33% of Iodine doping, respectively. When we go over the second peak, we notice a rapid decrease of the absorption as a function of λ.

The refractive index n (ω) is a dimensionless size characteristic of a medium, describing the behavior of light in it, this depends on the measurement wavelength, but also the characteristics of the environment (in particular pressure and temperature). From the **Figure**

V.10.d, we notice that the maximum of the refractive index for bulk $CsPbBr_3$ is 2.53 when the wavelength is equal to ~ 400 nm (visible), 2.46 for 22% when the wavelength is equal to ~ 500 nm (visible) and 2.49 for 33% when the wavelength is equal to ~ 350 nm (ultraviolet) of Iodine. In the range of wavelength between 600 and 1000 nm, we observe that the refractive index is conserved at 2.03, 2.23 and 2.28 for 0%, 22% and 33% of Iodine, respectively.

The **Figure V.10.e** shows that the reflectivity R (ω) decreases with the wavelength, we observe that the highest value of reflectivity for bulk is 0.24 obtained in ultraviolet at 280 nm and for all concentration of doping the reflectivity is equal to 2.26 obtained in ultraviolet at 312 nm. The reflectivity decreases as a function of λ. We notice that the reflectivity stabilizes at 0.115 for bulk, 0.146 for 22% and 0.152 for 33% of Iodine.

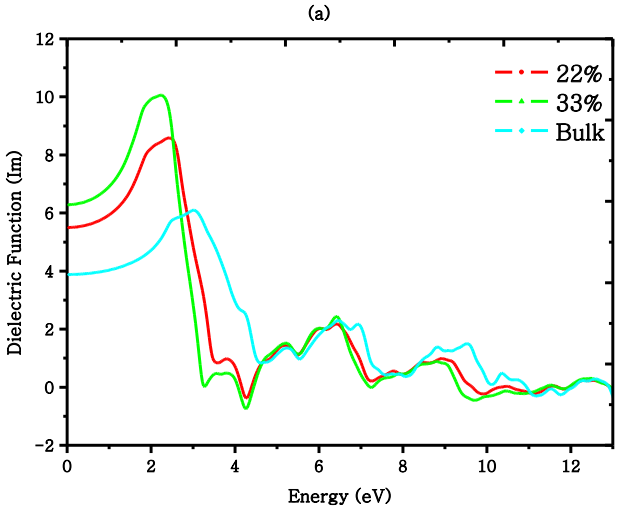

(b)

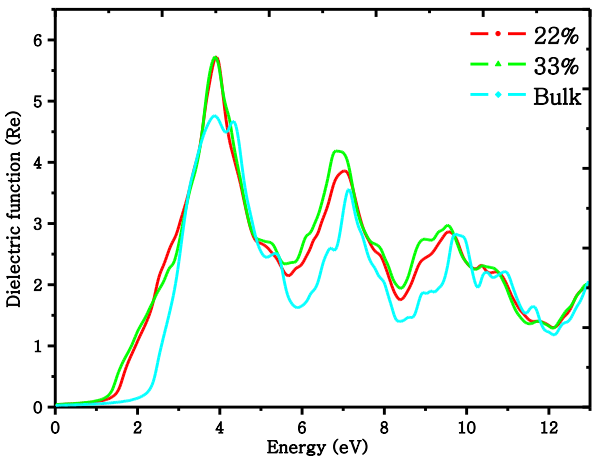
22%
33%
Bulk
Dielectric function (Re)
Energy (eV)
0
1
2
3
4
5
6
0
2
4
6
8
10
12

(c)

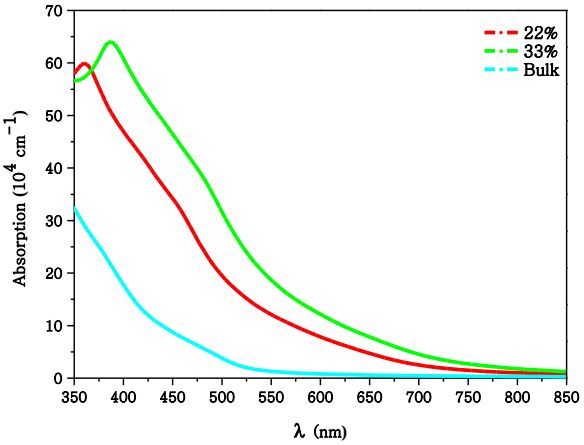
22%
33%
Bulk
Absorption (10^4 cm^-1)
λ (nm)
0
10
20
30
40
50
60
70
350
400
450
500
550
600
650
700
750
800
850

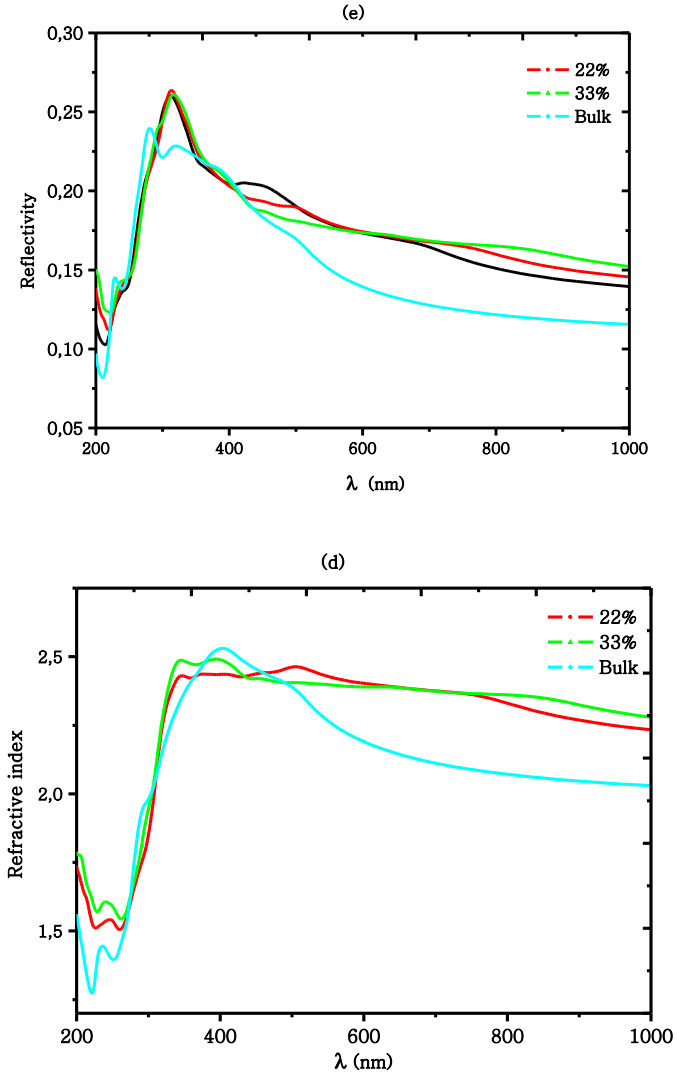

Figure V.10: Optical properties of $CsPbBr_3$ derived from density functional approximation : a and b) Dielectric function, c) Absorption, d) Refraction index and e) Reflectivity.

Conclusions

This theoretical work is based on the density functional theory applied to three different types of perovskites compounds; we determined the physical properties of these compounds. The aim of these studies is to show the best candidate for photovoltaic applications.

The chapter III is divided in two sections, in the first section we determined the electronic, optical and transport proprieties of $LaGaO_3$ perovskite compound using GGA-PBE

approximation. The transport proprieties are investigated using BoltzTraP code. According to the electronic band structure calculated with GGA-Pbe approximation, we conclude that we have an indirect gap, the value of the band gap determined from GGA-Pbe 3.61 eV. From the density of states we notice that we have a covalent and ionic hybridization between La and O and also between Ga and O in the entire range of energy. All optical properties are calculated and illustrated in details, showing that our materiel is a good absorber at ultraviolet, and the reflectivity don't exceed 20% in the entire range of wavelength. From the transport properties we notice that $LaGaO_3$ is P-type materials with electrical conductivity varied from 0 $(\Omega.m.s)^{-1}$ at 0°K to 10×10^{20} $(\Omega.m.s)^{-1}$ at 800 °K. In the second section we calculated the electrical and optical properties of doped $SrHfO_3$ perovskite compound using DFT. According to the electronic band structure we notice that the band structure changes from an indirect gap equivalent to 0% of S to a direct band gap equivalent to 8% and 16% of S, the value of the band gap reduced from 5.6 eV equivalent to 0% of S to 2.09 eV equivalent to 16% of S. From the density of states we notice that we have a covalent and ionic hybridization between Sr and O, Sr and S also between Hf and O, Hf and S in the entire range of energy. The optical properties are determined and illustrated in details, showing that $SrHfO_3$ doped S is a good absorber at ultraviolet light, and the reflectivity don't exceed 33% in the entire range of wavelength for all percentage of doping.

In Chapter IV we focus on determining the electrical, optical and transport properties of $BaZrS_3$ doped Se using the density functional theory. As a result we conclude that the gap decreases as a function of the percentage of Se and the value reduces from 1.59 eV for 0% of Se to 1.37 eV for 20% of Se. From the DOS we notice that we have a covalent and ionic hybridization between Ba and S, Se and also between Zr and S, Se in the entire range of energy. The optical properties are calculated in details, indicating that our materiels are a good absorber and from the transport proprieties we notice that $BaZrS_{3-x}Se_x$ is a P-type materiel.

Chapter V is divided in two sections. The first section focuses on determining the electrical and optical properties of $CsPbBr_3$doped I using the density functional theory. As a result we found that the gap decreases as a function of the percentage of I and the value reduces from 2.16 eV for 0% of I to 1.288 eV for 44% of I. the optical properties are calculated in details, indicating that the absorption coefficient changes as function of I showing a peak at the visible light corresponding to 33% and 44% of I. As a conclusion we can say that $CsPbBr_3$ doped I especially 33% of I with a direct gap equal to 1.439 eV and a good absorption showing a peak at the visible light is a best candidate for photovoltaic application waiting of

course the confirmation of the experimental study. In the second section we investigated the electronic, dielectric function and optical properties of the perovskite CsPbX3 (X=Br, C and I) compound using ab initio calculations. This perovskite has proposed for photovoltaic applications on account of their visible light absorption and direct band gap semiconductors. Moreover, by applying the strain effect, the gap energy decreases when increasing the strain, whereas, the absorption coefficient increases. The technique proposed is a good method to reduce the gap energy. Finally, the present compounds are one of the promising candidates for photovoltaic applications.

References

[1] Rose, G. De Novis Quibusdam Fossilibus, Quae in Montibus Uraliis Inveniuntur, Scripsit. Ann. Phys. 1839, 558.

[2] Popov, V. A. The Akhmatov Mine in the South Urals: Notes on Mineralogy. Mineral. Alm. 2012, 17, 8.

[3] Becquerel, A. E. Comptes Rendus Des Séances de l'académie Des Sciences. *Académie des Sci.* 1839, 145.

[4] Adams, W. G.; Day, R. E. The Action of Light on Selenium. *Phil. Trans. R. Soc. Lond.* 1877, 313.

[5] Einstein, A. Concerning an Heuristic Point of View toward the Emission and Transformation of Light. *Ann. Phys.* 1905, *17*, 1905.

[6] Chapin, D. M.; Fuller, C. S.; Pearson, G. L. A New Silicon P-n Junction Photocell for Converting Solar Radiation into Electrical Power. *J. Appl. Phys.* 1954, *25* (5), 676–677.

[7] Reynolds, D. C.; Leies, L. W.; Antes, L. L.; Marburger, R. E.; Leies, G.; Antes, L. L.; Marburger, R. E. Photovoltaic Effect in Cadmium Sulfide. *Phys. Rev.* 1954, *96* (2), 533.

[8] Andreev, V. M.; Kagan, M. B.; Protasov Alferov, I. I.; I, Z.; Trofim, V. G. Solar- Energy Converters Based on p-n AlxGa1-x As-GaAs Heterojunctions. *Sov. Phys. Semocond.* 1971, No. 4, 2047.

[9] Woodall, J. M.; Hovel, H. J. High-efficiency Ga1-x Alx As–GaAs Solar Cells. *Appl. Phys. Lett.* 1972, *21* (8), 379–381.

[10] Carlson, D. E.; Wronski, C. R. Amorphous Silicon Solar Cell. *Appl. Phys. Lett.* 1976, *28* (11), 671–673.

[11] Shockley, W.; Queisser, H. J. Detailed Balance Limit of Efficiency of P-n Junction Solar Cells. *J. Appl. Phys.* 1961, *32* (3), 510–519.

[12] Wang, A.; Zhao, J.; Green, M. A. 24% Efficient Silicon Solar Cells. *Appl. Phys. Lett.* 1990, *57* (6), 602–604.

[13] Tang, C. W. Two-Layer Organic Photovoltaic Cell. *Appl. Phys. Lett.* 1986, *48* (2), 183–185.

[14] O'Regan, B.; Gratzel, M. A Low-Cost, High-Efficiency Solar-Cell Based on Dye-Sensitized Colloidal TiO2 Films. *Nature* 1991, *353* (6346), 737–740.

[15] Akihiro Kojima; Teshima, K.; Shirai, Y.; Miyasaka, T. Organometal Halide Perovskites as Visible- Light Sensitizers for Photovoltaic Cells. *J Am Chem Soc* 2009, *131* (October), 6050–6051.

[16] Yoshikawa K, Kawasaki H, Yoshida W, et al. Silicon heterojunction solar cell with interdigitated back contacts for a photoconversion efficiency over 26%. Nat Energy. 2017;2(5):17032

[17] Kayes BM, Nie H, Twist R, Spruytte SG, Reinhardt F, Kizilyalli IC, Higashi GS. 27.6% conversion efficiency, a new record for single-junction solar cells under 1 sun illumination. Proceedings of the 37th IEEE Photovoltaic Specialists Conference, 2011.

[18] Kato T, Handa A, Yagioka T, Matsuura T, Yamamoto K, Higashi S, Wu J-L, Tai KF, Hiroi H, Yoshiyama T, Sakai T, Sugimoto H. Enhanced efficiency of Cd-free Cu(In,Ga)(Se,S)2 minimodule via (Zn,Mg)O second buffer layer and alkali post treatment. 44th IEEE Photoovltaic Specialists Conference, Washington DC, 25–30 June 2017

[19] Yang WS, Noh JH, Jeon NJ, et al. High-performance photovoltaic perovskite layers fabricated through intramolecular exchange. Science. 2015;348(6240):1234-1237.

[20] Mori S, Oh-oka H, Nakao H, Gotanda T, Nakano Y, Jung H, Iida A, Hayase R, Shida N, Saito M, Todori K, Asakura T, Matsui A, Hosoya M. Organic photovoltaic module

development with inverted device structure. MRS Proceedings, Vol. 1737, 2015 (DOI: https://doi.org/ 10.1557/opl.2015.540).

[21] Komiya R, Fukui A, Murofushi N, Koide N, Yamanaka R and Katayama H. Improvement of the conversion efficiency of a monolithic type dye-sensitized solar cell module. Technical Digest, 21st International Photovoltaic Science and Engineering Conference, Fukuoka, November 2011; 2C-5O-08

[22] Chiu PT, Law DL, Woo RL, Singer S, Bhusari D, Hong WD, Zakaria A, Boisvert JC, Mesropian S, King RR, Karam NH. 35.8% space and 38.8% terrestrial 5J direct bonded cells. Proc. 40th IEEE Photovoltaic Specialist Conference, Denver, June 2014; 11–13.

[23] Sasaki K, Agui T, Nakaido K, Takahashi N, Onitsuka R, Takamoto T. Proceedings, 9th International Conference on Concentrating Photovoltaics Systems. Japan: Miyazaki; 2013.

[24] Essig S, Allebé C, Remo T, et al. Raising the one-sun conversion efficiency of III–V/Si solar cells to 32.8% for two junctions and 35.9% for three junctions. Nature Energy. 2017;2(9):17144. https://doi.org/ 10.1038/nenergy.2017.144

[25] Green MA, Keevers MJ, Concha Ramon B, Jiang Y, Thomas I, Lasich JB, Verlinden, PJ, Yang Y, Zhang X, Emery K, Moriarty T, King RR, Bensch W. Improvements in sunlight to electricity conversion efficiency: above 40% for direct sunlight and over 30% for global. Paper 1AP.1.2, European Photovoltaic Solar Energy Conference 2015, Hamburg, September 2015.

[26] Özen, Y., Akın, N., Kınacı, B., & Özçelik, S. (2015). Performance evaluation of a GaInP/GaAs solar cell structure with the integration of AlGaAs tunnel junction. Solar Energy Materials and Solar Cells, 137, 1-5.

[27] SASAKI, Kazuaki, AGUI, Takaaki, NAKAIDO, Katsuya, et al. Development of InGaP/GaAs/InGaAs inverted triple junction concentrator solar cells. In : AIP conference proceedings. American Institute of Physics, 2013. p. 22-25.

[28] Essig, S., Allebé, C., Remo, T. et al. Raising the one-sun conversion efficiency of III–V/Si solar cells to 32.8% for two junctions and 35.9% for three junctions. Nat Energy 2, 17144 (2017). https://doi.org/10.1038/nenergy.2017.144

[29] Rajkanan, K.; Singh, R.; Shewchun, J. Absorption Coefficient of Silicon for Solar Cell Calculations. *Solid. State. Electron.* **1979**, *22* (9), 793.

[30] Hoppe, H.; Sariciftci, N. S. Organic Solar Cells: An Overview. *J. Mater. Res.* **2004**, *19* (7), 1924–1945.

[31] Green, M. A. Improved Value for the Silicon Free Exciton Binding Energy. *AIP Adv.* **2013**, *3* (11).

[32] Servaites, J. D.; Ratner, M. A.; Marks, T. J. Organic Solar Cells: A New Look at Traditional Models. *Energy Environ. Sci.* **2011**, *4* (11), 4410.

[33] Shockley, W. The Theory of P-n Junctions in Semiconductors and p-n Junction Transistors. *Bell Labs Tech. J.* **1949**, *28* (3), 435.

[34] Lindholm, F. A.; Fossum, J. G.; Burgess, E. L. Application of the Superposition Principle to Solar-Cell Analysis. *IEEE Trans. Electron Devices* **1979**, *26* (3), 165–171.

[35] Kojima, A.; Teshima, K.; Shirai, Y.; Miyasaka, T. Organometal Halide Perovskites as VisibleLight Sensitizers for Photovoltaic Cells. Journal of the American Chemical Society 2009, 131, 6050–6051

[36] Kim, H.-S.; Lee, C.-R.; Im, J.-H.; Lee, K.-B.; Moehl, T.; Marchioro, A.; Moon, S.-J.; Humphry-Baker, R.; Yum, J.-H.; Moser, J. E.; Grätzel, M.; Park, N.-G. Lead Iodide

Perovskite Sensitized All-Solid-State Submicron Thin Film Mesoscopic Solar Cell with Efficiency Exceeding 9%. Scientific Reports 2012, 2, 591.

[37] Lee, M. M.; Teuscher, J.; Miyasaka, T.; Murakami, T. N.; Snaith, H. J. Efficient Hybrid Solar Cells Based on Meso-Superstructured Organometal Halide Perovskites. Science 2012, 338, 643–647.

[38] Tan, Z.-K.; Moghaddam, R. S.; Lai, M. L.; Docampo, P.; Higler, R.; Deschler, F.; Price, M.; Sadhanala, A.; Pazos, L. M.; Credgington, D.; et al. Bright Light-Emitting Diodes Based on Organometal Halide Perovskite. *Nat. Nanotechnol.* **2014**, *9* (9), 687–692.

[39] Stranks, S. D.; Snaith, H. J. Metal-Halide Perovskites for Photovoltaic and LightEmitting Devices. *Nat. Nanotechnol.* **2015**, *10* (5), 391–402.

[40] Zuo, C.; Bolink, H. J.; Han, H.; Huang, J.; Cahen, D.; Ding, L. Advances in Perovskite Solar Cells. *Adv. Sci.* **2016**, *3* (7), 1–16.

[41] Deschler, F.; Price, M.; Pathak, S.; Klintberg, L. E.; Jarausch, D. D.; Higler, R.; Hüttner, S.; Leijtens, T.; Stranks, S. D.; Snaith, H. J.; et al. High Photoluminescence Efficiency and Optically Pumped Lasing in Solution-Processed Mixed Halide Perovskite Semiconductors. *J. Phys. Chem. Lett.* **2014**, *5* (8), 1421–1426.

[42] Denk, W.; Strickler, J. H.; Webb, W. W. Two-Photon Laser Scanning Fluorescence Microscopy. *Science* **1990**, *248* (4951), 73–76.

[43] Wang, H.; Kim, D. H. Perovskite-Based Photodetectors: Materials and Devices. *Chem. Soc. Rev.* **2017**, *46* (17), 5204–5236.

[44] Saidaminov, M. I.; Adinolfi, V.; Comin, R.; Abdelhady, A. L.; Peng, W.; Dursun, I.; Yuan, M.; Hoogland, S.; Sargent, E. H.; Bakr, O. M. Planar-Integrated Single-Crystalline Perovskite Photodetectors. *Nat. Commun.* **2015**, *6*, 1–7.

[45] Zhang, W.; Eperon, G. E.; Snaith, H. J. Metal Halide Perovskites for Energy Applications. *Nat. Energy* **2016**, *1* (6).

[46] Tian, W.; Zhou, H.; Li, L. Hybrid Organic–Inorganic Perovskite Photodetectors. *Small* **2017**, *13* (41).

[47] Petrović, M.; Chellappan, V.; Ramakrishna, S. Perovskites: Solar Cells & Engineering Applications - Materials and Device Developments. *Sol. Energy* **2015**, *122*, 678–699.

[48] Chen, J.; Zhou, S.; Jin, S.; Li, H.; Zhai, T. Crystal Organometal Halide Perovskites with Promising Optoelectronic Applications. *J. Mater. Chem. C* **2016**, *4* (1), 11–27.

[49] Era, M.; Morimoto, S.; Tsutsui, T.; Saito, S. Organic-Inorganic Heterostructure Electroluminescent Device Using a Layered Perovskite Semiconductor (C6H5C2H4NH3)2PbI4. *Appl. Phys. Lett.* **1994**, *65* (6), 676–678.

[50] Mitzi, D. B.; Chondroudis, K.; Kagan, C. R. Organic – Inorganic Electronics. *IBM J. RES. DEV.* **2001**, *45* (1), 29–45.

[51] Kumawat, N. K.; Dey, A.; Narasimhan, K. L.; Kabra, D. Near Infrared to Visible Electroluminescent Diodes Based on Organometallic Halide Perovskites: Structural and Optical Investigation. *ACS Photonics* **2015**, *2* (3), 349–354.

[52] Kim, Y. H.; Cho, H.; Heo, J. H.; Kim, T. S.; Myoung, N. S.; Lee, C. L.; Im, S. H.; Lee, T. W. Multicolored Organic/Inorganic Hybrid Perovskite Light-Emitting Diodes. *Adv. Mater.* **2015**, *27* (7), 1248–1254.

[53] Kumawat, N. K.; Dey, A.; Kumar, A.; Gopinathan, S. P.; Narasimhan, K. L.; Kabra, D. Band Gap Tuning of CH3NH3Pb(Br1-XClx)3Hybrid Perovskite for Blue Electroluminescence. *ACS Appl. Mater. Interfaces* **2015**, *7* (24), 13119–13124.

[54] Jaramillo-Quintero, O. A.; Sanchez, R. S.; Rincon, M.; Mora-Sero, I. Bright Visible-Infrared Light Emitting Diodes Based on Hybrid Halide Perovskite with SpiroOMeTAD as a Hole-Injecting Layer. *J. Phys. Chem. Lett.* **2015**, *6* (10), 1883–1890.

[55] Li, G.; Tan, Z. K.; Di, D.; Lai, M. L.; Jiang, L.; Lim, J. H. W.; Friend, R. H.; Greenham, N. C. Efficient Light-Emitting Diodes Based on Nanocrystalline Perovskite in a Dielectric Polymer Matrix. *Nano Lett.* **2015**, *15* (4), 2640–2644.

[56] Gao, J. Polymer Light-Emitting Electrochemical Cells—Recent Advances and Future Trends. *Curr. Opin. Electrochem.* **2018**, *7* (d), 87–94.

[57] Meier, S. B.; Tordera, D.; Pertegás, A.; Roldán-Carmona, C.; Ortí, E.; Bolink, H. J. Light-Emitting Electrochemical Cells: Recent Progress and Future Prospects. *Mater. Today* **2014**, *17* (5), 217–223.

[58] Aygüler, M. F.; Weber, M. D.; Puscher, B. M. D.; Medina, D. D.; Docampo, P.; Costa, R. D. Light-Emitting Electrochemical Cells Based on Hybrid Lead Halide Perovskite Nanoparticles. *J. Phys. Chem. C* **2015**, *119* (21), 12047–12054.

[59] Kondo, T.; Azuma, T.; Yuasa, T.; Ito, R. Biexciton Lasing in the Layered Perovskite-Type Material (C6H13NH3)2PbI4. *Solid State Commun.* **1998**, *105* (4), 253–255.

[60] Zhu, H.; Fu, Y.; Meng, F.; Wu, X.; Gong, Z.; Ding, Q.; Gustafsson, M. V.; Trinh, M. T.; Jin, S.; Zhu, X. Y. Lead Halide Perovskite Nanowire Lasers with Low Lasing Thresholds and High Quality Factors. *Nat. Mater.* **2015**, *14* (6), 636–642.

[61] Dou, L.; Yang, Y. M.; You, J.; Hong, Z.; Chang, W. H.; Li, G.; Yang, Y. SolutionProcessed Hybrid Perovskite Photodetectors with High Detectivity. *Nat. Commun.* **2014**, *5*,1–6.

[62] Yakunin, S.; Mykhailo, S.; Dominik, K.; Shrestha, S.; Richter, M.; Matt, G. J.; Hamed, A.; Christoph J., B.; Julian, S.; Masksym V., K.; et al. Detection of X-Ray Photons by Solution-Processed Lead Halide Perovskites. *Nat. Photonics* **2015**, *9* (7), 444.

[63] Kasap, S. O. X-Ray Sensitivity of Photoconductors: Application to Stabilized aSe. *J. Phys. D. Appl. Phys.* **2000**, *33* (21), 2853–2865.

[64] Wei, H.; Fang, Y.; Mulligan, P.; Chuirazzi, W.; Fang, H. H.; Wang, C.; Ecker, B. R.; Gao, Y.; Loi, M. A.; Cao, L.; et al. Sensitive X-Ray Detectors Made of Methylammonium Lead Tribromide Perovskite Single Crystals. *Nat. Photonics* **2016**, *10* (5), 333–339.

[65] Kagan, C. R.; Mitzi, D. B.; Dimitrakopoulos, C. D. Organic-Inorganic Hybrid Materials as Semiconducting Channels in Thin- Film Field-Effect Transistors. *Science (80-.).* **1999**, *286* (5441), 945–947.

[66] Chin, X. Y.; Cortecchia, D.; Yin, J.; Bruno, A.; Soci, C. Lead Iodide Perovskite Light-Emitting Field-Effect Transistor. *Nat. Commun.* **2015**, *6* (May), 1–9.

[67] P. Hohenberg and W. Kohn, Phys. Rev. 136, B864 (1964).

[68] W. Kohn and L. Sham, Phys. Rev. 140, A1133 (1965).

[69] R. Dreizler and E. Gross, Density Functional Theory (Spinger-Verlag, Berlin Heidelberg, 1990).

[70] D. M. Ceperley and B. J. Adler, Phys. Rev. Lett. 45, 566 (1980).

[71] R. O. Jones and O. Gunnarsson, Reviews of Modern Physics 61, 689 (1989).

[72] J. Kübler and V. Eyert, Electronic structure calculations dans : Electronic and Magnetic Properties of Metals and Ceramics (K. H. J. Buschow (VCH Verlagsgesellschaft), Weinheim, 1992).

[73] J. C. Slater, Phys. Rev. 81, 385 (1951).

[74] S. J. Vosko, L. Wilk, et M. Nussair, Can. J. Phys. 58, 1200 (1980).

[75] D. M. Ceperley et B. J. Alder, Phys. Rev. Lett. 45, 566 (1980).

[76] J.P.Perdew, K.Burke, and M.Ernzerhof, Phys. Rev. Lett. 77, 3865 (1996).

[77] G. Garcia, C. Elsässer, S. Louie, and M. Cohen, Phys. Rev. B 46, 9829 (1992).

[78] A. Zupan, P. Blaha, K. Schwartz, and J. P. Perdew, Phys. Rev. B 58, 11266 (1998).

[79] A. D. Becke, Phys. Rev. A 38, 3098 (1988).

[80] J. P. Perdew et Y. Wang, Phys. Rev. B 33, 8800 (1986).

[81] N. C. Handy et A. J. Cohen, Mol. Phys. 99, 403 (2001).

[82] J. P. Perdew et Y. Wang, Phys. Rev. B 45, 244 (1992).

[83] J. P. Perdew, K. Burke, et M. Ernzerhof, Phys. Rev. Lett. 77, 3865 (1996).

[84] A. D. Becke, J. Chem. Phys. 84, 4524 (1986).

[85] C. Lee, W. Yang, et R. G. Parr, Phys. Rev. B 37, 785 (1988).

[86] A. D. Becke, J. Chem. Phys. 98, 5648 (1993).

[87] A. D. Becke, J. Chem. Phys. 98, 1372 (1993).

[88] P. J. Stephens, F. J. Devlin, C. F. Chabalowski, et M. J. Frisch, J. Phys. Chem. 98, 11623 (1994).

[89] V. Barone, Chem. Phys. Lett. 226, 392 (1994).

[90] M. D. Wodrich, C. Corminboeuf, et P. von Ragué Schleyer, Org. Lett. 8, 3631 (2006).

[91] E. M. Sproviero, J. A. Gascon, J. P. McEvoy, G. W. Brudvig, et V. S. Batista, J. Inorg. Biochem. 100, 786 (2006).

[92] Xinhui Xia et al., « Perovskite Solar Cell Powered Electrochromic Batteries for Smart Windows », Mater. Horiz 3, nº 6 (2016): 588-95, https://doi.org/10.1039/C6MH00159A.

[93] Letao Yang et al., « Perovskite Lead-Free Dielectrics for Energy Storage Applications », Prog. Mater. Sci 102 (mai 2019): 72-108, https://doi.org/10.1016/j.pmatsci.2018.12.005.

[94] Jiyue Wu et al., « Perovskite Sr x (Bi 1−x Na 0.97−x Li 0.03) 0.5 TiO 3 Ceramics with Polar Nano Regions for High Power Energy Storage », Nano Energy 50 (août 2018): 723-32, https://doi.org/10.1016/j.nanoen.2018.06.016

[95] Chunqing Ma et al., « 2D Perovskites with Short Interlayer Distance for High-Performance Solar Cell Application », Adv. Mater 30, no 22 (mai 2018): 1800710, https://doi.org/10.1002/adma.201800710.

[96] Hua Dong et al., « Pseudohalide-Induced Recrystallization Engineering for CH 3 NH 3 PbI 3 Film and Its Application in Highly Efficient Inverted Planar Heterojunction Perovskite Solar Cells », Adv. Funct. Mater 28, no 2 (janvier 2018): 1704836, https://doi.org/10.1002/adfm.201704836.

[97] Emery, A. A. & Wolverton, C. High-throughput DFT calculations of formation energy, stability and oxygen vacancy formation energy of ABO3 perovskites. Sci. Data 4:170153 doi: 10.1038/sdata.2017.153 (2017).

[98] Chao Zheng et Oleg Rubel, « Aziridinium Lead Iodide: A Stable, Low-Band-Gap Hybrid Halide Perovskite for Photovoltaics », J. Phys. Chem. Lett 9, no 4 (15 février 2018): 874-80, https://doi.org/10.1021/acs.jpclett.7b03114.

[99] Ryan Jacobs et al., « Material Discovery and Design Principles for Stable, High Activity Perovskite Cathodes for Solid Oxide Fuel Cells », Adv. Energy Mater 8, no 11 (avril 2018): 1702708, https://doi.org/10.1002/aenm.201702708.

[100] Feng Zhou et al., « Pd-Doped La0.6Sr0.4Co0.2Fe0.8O3−δ Perovskite Oxides as Cathodes for Intermediate Temperature Solid Oxide Fuel Cells », Solid State Ionics 319 (juin 2018): 22-27, https://doi.org/10.1016/j.ssi.2018.01.044.

[101] Lung-Chien Chen et al., « Perovskite CsPbBr3 Quantum Dots Prepared Using Discarded Lead–Acid Battery Recycled Waste », Energies 12, no 6 (22 mars 2019): 1117, https://doi.org/10.3390/en12061117.

[102] Taiye J. Salami et al., « Amorphous Glass-Perovskite Composite as Solid Electrolyte for Lithium-Ion Battery », Mater. Lett 254 (novembre 2019): 294-96, https://doi.org/10.1016/j.matlet.2019.07.084.

[103] I. Georgiopoulos et al., « LaAlO3 as Overlayer in Conventional Thermal Barrier Coatings », Procedia Structural Integrity 10 (2018): 280-87, https://doi.org/10.1016/j.prostr.2018.09.039.

[104] Yong-Chun Li et al., « Promoting the Electrochemical Performance of LiNi0.8Co0.1Mn0.1O2 Cathode via LaAlO3 Coating », J. Alloys Compd 766 (octobre 2018): 546-55, https://doi.org/10.1016/j.jallcom.2018.06.364.

[105] S. Thiel, « Tunable Quasi-Two-Dimensional Electron Gases in Oxide Heterostructures », *Science* 313, n° 5795 (29 septembre 2006): 1942-45, https://doi.org/10.1126/science.1131091.

[106] U. Schwingenschlögl et C. Schuster, « Exponential Decay of Relaxation Effects at LaAlO3/SrTiO3 Heterointerfaces », Chem. Phys. Lett 467, n° 4-6 (janvier 2009): 354-57, https://doi.org/10.1016/j.cplett.2008.11.054.

[107] Naoyuki Nakagawa, Harold Y. Hwang, et David A. Muller, « Why Some Interfaces Cannot Be Sharp », Nat. Mater 5, n° 3 (mars 2006): 204-9, https://doi.org/10.1038/nmat1569.

[108] P. R. Willmott et al., « Structural Basis for the Conducting Interface between LaAlO 3 and SrTiO 3 », Phys. Rev. Lett 99, n° 15 (9 octobre 2007), https://doi.org/10.1103/PhysRevLett.99.155502.

[109] M. P. Warusawithana et al., « LaAlO3 Stoichiometry Is Key to Electron Liquid Formation at LaAlO3/SrTiO3 Interfaces », Nat. Commun 4, n° 1 (décembre 2013), https://doi.org/10.1038/ncomms3351.

[110] H. Boysen et al., « Structure and Ionic Conductivity in Doped LaGaO<Subscript>3</Subscript> », Appl. Phys *A* 74, n° 1 (1 décembre 2002): s966-68, https://doi.org/10.1007/s003390101168.

[111] A. Kaabi et al., « Influence of Electrolyte Concentration on the Electrochemical Characteristics of LaGaO 3 Perovskite Oxide as Novel Anode Material for Ni/MH Batteries », *Ceramics International* 43, n° 17 (décembre 2017): 15743-46, https://doi.org/10.1016/j.ceramint.2017.08.136.

[112] Minna Nieminen, Sari Lehto, et Lauri Niinistö, « Atomic Layer Epitaxy Growth of LaGaO3 Thin Films », J. Mater. Chem 11, n° 12 (23 novembre 2001): 3148-53, https://doi.org/10.1039/B105978P.

[113] Y Wang et al., « High Temperature Transmission Electron Microscopy and X-Ray Diffraction Studies of Twinning and the Phase Transition at 145 °C in LaGaO3 », s. d., 9.

[114] Bo Wu et al., « Ab Initio Structural and Energetic Study of (, Ga) Perovskites », J. Phys. Chem. Solids 68, nº 4 (avril 2007): 570-75, https://doi.org/10.1016/j.jpcs.2007.01.031.

[115] Song, Q-G., Du, Q., Song, L., Zhao, H. and Guo, Y. (2014) 'The structural stabilities and electronic properties of orthorhombic and rhombohedral LaGaO3: a first-principles study', Int. J. Nanomanufacturing, Vol. 10, Nos. 1/2, pp.13–25

[116] AytaçErkişi, GökhanGökoğlu, GökhanSürücü, RecaiEllialtıoğlu&ErdemKamilYıldırım (2016): First-principles investigation of LaGaO3 and LaInO3 lanthanum perovskite oxides, Philosophical Magazine.

[117] B. Wu, M. Zinkevich, F. Aldinger, W. Zhang, Ab initio structural and energetic study of (, Ga) perovskites, J. Phys. Chem. Solids. 68 (2007) 570–575. doi:http://dx.doi.org/10.1016/j.jpcs.2007.01.031.

[118] V. Lucarini, éd., Kramers-Kronig Relations in Optical Materials Research, Springer Series in Optical Sciences, v. 110 (Berlin ; New York: Springer, 2005).

[119] G. Rose, De Novis Quibusdam Fossilibus, Quae in Montibus Uraliis Inveniuntur. Ann. Phys. 48, 558 (1839).

[120] V. A Popov, The Akhmatov Mine in the South Urals: Notes on Mineralogy. Mineral. Alm. 8, 17 (2012).

[121] Berri Saadi, First-principles study on half-metallic properties of the Sr2GdReO6 double perovskite. Journal of Magnetism and Magnetic Materials 385, 124-128 (2015).

[122] Berri Saadi, Nadir Bouarissa and Mourad Attallah, First-Principles Predictions on Half-Metallic Results of RBaMn2O6-δ (R= Nd, Pr, La and δ= 0, 1) Double Perovskite Compounds. Journal of Superconductivity and Novel Magnetism 33, 1737-1746 (2020).

[123] Akihiro Kojima, Kenjiro Teshima, Yasuo Shirai and Tsutomu Miyasaka, Organometal Halide Perovskites as Visible-Light Sensitizers for Photovoltaic Cells. J. Am. Chem. Soc. 131, 6050-6051 (2009).

[124] Qi Jiang, Yang Zhao, Xingwang Zhang, Xiaolei Yang, Yong Chen, Zema Chu, Qiufeng Ye, Xingxing Li, Zhigang Yin and Jingbi You, Nature Photonics **13**, 460-466(2019).

[125] Z. K. Tan, R. S. Moghaddam, M. L. Lai, P. Docampo, R. Higler, F. Deschler, M. Price, A. Sadhanala, L. M. Pazos, D. Credgington, F Hanusch, Thomas Bein, Henry J. Snaith and Richard H. Friend, Bright Light-Emitting Diodes Based on Organometal Halide Perovskite. Nat. Nanotechnol. 9, 687-692 (2014).

[126] S. D. Stranks, H. J. Snaith, Metal-Halide Perovskites for Photovoltaic and Light Emitting Devices. Nat. Nanotechnol. 10, 391-402 (2015).

[127] C. Zuo, H. J. Bolink, H. Han, J. Huang, D. Cahen, L. Ding, Advances in Perovskite Solar Cells. Adv. Sci. 3, 1-16 (2016).

[128] F. Deschler, M. Price, S. Pathak, L. E. Klintberg, D. D. Jarausch, R. Higler, S. Hüttner, T. Leijtens, S. D. Stranks, H. J. Snaith, M. Atatüre, R. T. Phillips and R. H. Friend, High Photoluminescence Efficiency and Optically Pumped Lasing in Solution-Processed Mixed Halide Perovskite Semiconductors. J. Phys. Chem. Lett. 5, 1421-1426 (2014).

[129] W. Denk, J. H. Strickler and W. W. Webb, Two-Photon Laser Scanning Fluorescence Microscopy. Science 248, 73-76 (1990).

[130] H. Wang and D. H. Kim, Perovskite-Based Photodetectors: Materials and Devices. Chem. Soc. Rev. 46, 5204-5236 (2017).

[131] M. I. Saidaminov, V. Adinolfi, R. Comin, A. L. Abdelhady, W. Peng, I. Dursun, M. Yuan, S. Hoogland, E. H. Sargent and O. M. Bakr, Planar-Integrated Single-Crystalline Perovskite Photodetectors. Nat. Commun. 6, 1-7 (2015).

[132] W. Zhang, G. E. Eperon and H. J. Snaith, Metal Halide Perovskites for Energy Applications. Nat. Energy, 1, 1-8 (2016).

[133] W. Tian, H. Zhou and L. Li, Hybrid Organic–Inorganic Perovskite Photodetectors. Small 13, 1702107 (2017).

[134] M. Petrović, V. Chellappan and S. Ramakrishna, Perovskites: Solar Cells & Engineering Applications-Materials and Device Developments. Sol. Energy 122, 678-699 (2015).

[135] J. Chen, S. Zhou, S. Jin, H. Li, T. Zhai, Crystal Organometal Halide Perovskites with Promising Optoelectronic Applications. J. Mater. Chem. C 4, 11-27 (2016).

[136] Aslihan Babayigit, Anitha Ethirajan, Marc Muller and Bert Conings, Toxicity of organometal halide perovskite solar cells. Nature Materials 15, 247-251 (2016).

[137] Bekele Hailegnaw, Saar Kirmayer, Eran Edri, Gary Hodes and David Cahen, Rain on Methylammonium Lead Iodide Based Perovskites: Possible Environmental Effects of Perovskite Solar Cells. J. Phys. Chem. Lett. 6, 1543-1547 (2015).

[138] Nicholas Aristidou, Irene Sanchez-Molina, Thana Chotchuangchutchaval, Michael Brown, Luis Martinez, Thomas Rath and Saif A Haque, The Role of Oxygen in the Degradation of Methylammonium Lead Trihalide Perovskite Photoactive Layers. Angew. Chem. Int. Ed. Engl. 54, 8208-82012 (2015).

[139] C. Rossel, M. Sousa, C. Marchiori, J. Fompeyrine, D. Webb, D. Caimi, B. Mereu, A. Ispas, J. P. Locquet, H. Siegwart, R. Germann, A. Tapponnier and K. Babich, SrHfO3 as gate dielectric for future CMOS technology. Microelec. Eng. 84, 1869-1873 (2007).

[140] Cuffini, Silvia, J. A. Guevara, Y. P. Mascarenhas, P. de la Presa, A. Ayala and A. Lopez Garcia, High temperature studies of Perovskite oxides: x-ray diffraction and PAC spectroscopy. Ceramica 31, 91-94 (1997).

[141] B. J. Kennedy, C. J. Howard, B. C. Chakoumakos, High-temperature phase transitions in SrHfO3. Phys. Rev. B 60, 2972 (1999).

[142] D.P.Rai, Sandeep, A. Shankar, Anup Pradhan Sakhya, T. P. Sinha, B. Merabet, M. Musa Saad H.-E, R. Khenata, Arash Boochani, Shahram Solaymani and R. K. Thapa, Electronic and optical properties of cubic SrHfO3 at different pressures: A first principles study. Materials Chemistry and Physics 186, 620-626 (2017).

[143] Vali R. Structural phases of SrHfO3. Solid state communications. 148, 29-31 (2008).

[144] C. Rossel, B. Mereu, C. Marchiori, D. Caimi, M. Sousa, A. Guiller, H. Siegwart, R. Germann, J. P. Locquet, J. Fompeyrine, D. J. Webb, C. Dieker and J. W. Seo, Field-effect transistors with $SrHfO_3$ as gate oxide. Appl. Phys. Lett. 89, 053506 (2006).

[145] Rose, G. De Novis Quibusdam Fossilibus, Quae in Montibus Uraliis Inveniuntur, Scripsit. Ann. Phys. 1839, 558.

[146] Popov, V. A. The Akhmatov Mine in the South Urals: Notes on Mineralogy. Mineral. Alm. 2012, 17, 8.

[147] Akihiro Kojima et al., « Organometal Halide Perovskites as Visible-Light Sensitizers for Photovoltaic Cells », *Journal of the American Chemical Society* 131, n^{o} 17 (6 mai 2009): 6050-51, https://doi.org/10.1021/ja809598r.

[148] Qi Jiang et al., « Surface Passivation of Perovskite Film for Efficient Solar Cells », *Nature Photonics* 13, nº 7 (juillet 2019): 460-66, https://doi.org/10.1038/s41566-019-0398-2.

[149] Aslihan Babayigit et al., « Toxicity of Organometal Halide Perovskite Solar Cells », *Nature Materials* 15, nº 3 (mars 2016): 247-51, https://doi.org/10.1038/nmat4572.

[150] Bekele Hailegnaw et al., « Rain on Methylammonium Lead Iodide Based Perovskites: Possible Environmental Effects of Perovskite Solar Cells », *The Journal of Physical Chemistry Letters* 6, nº 9 (7 mai 2015): 1543-47, https://doi.org/10.1021/acs.jpclett.5b00504.

[151] Nicholas Aristidou et al., « The Role of Oxygen in the Degradation of Methylammonium Lead Trihalide Perovskite Photoactive Layers », *Angewandte Chemie International Edition* 54, nº 28 (6 juillet 2015): 8208-12, https://doi.org/10.1002/anie.201503153.

[152] H. Hahn, U. Mutschke, Untersuchungen über ternäre Chalkogenide. XI. Versuche zur Darstellung von Thioperowskiten. Z. Anorg. Allg. Chem. 288, 269-278 (1957).

[153] A. Clearfield, The synthesis and crystal structures of some alkaline earth titanium and zirconium sulfides. Acta Crystallogr. 16, 135-142 (1963).

[154] R. Lelieveld, D. J. W. Ijdo, Sulphides with the $GdFeO_3$ Structure. Acta Crystallogr. B36, 2223-2226 (1980).

[155] Y. Wang, N. Sato, T. Fujino, Synthesis of $BaZrS_3$ by short time reaction at lower temperatures. J. Alloy. Comp. 327, 104-112 (2001).

[156] C.-S. Lee, K. M. Kleinke, H. Kleinke, Synthesis, Structure, and electronic and physical properties of the two $SrZrS_3$ modifications. Solid State Sciences 7, 1049-1054 (2005).

[157] M. Ishii, M. Saeki, Raman and Infrared Spectra of BaTiS3 and BaNbS3. Phys. Stat. Sol. (b) 170, K49 (1992).

[158] M. Ishii, M. Saeki, M. Sekita, Vibrational spectra of barium-zirconium sulfides. Mater. Res. Bull. 28, 493-500 (1993).

[159] Y. Chen et al., Carbon Kagome Lattice and Orbital-Frustration-Induced Metal-Insulator Transition for Optoelectronics. Physical Review Letters 113, 085501 (2014).

[160] S. Niu *et al.,* Bandgap Control via Structural and Chemical Tuning of Transition Metal Perovskite Chalcogenides. *Adv. Mater*. **29**, 1604733 (2017).

[161] S. Perera *et al.*, Chalcogenide perovskites – an emerging class of ionic semiconductors. *Nano Energy* **22**, 129-135 (2016).

[162] K. Hanzawa, S. Iimura, H. Hiramatsu, H. Hosono, Material Design of Green-Light-Emitting Semiconductors: Perovskite-Type Sulfide SrHfS3. *J. Am. Chem. Soc.* **141**, 5343-5349 (2019).

[163] N. Gross et al., Stability and Band-Gap Tuning of the Chalcogenide Perovskite $BaZrS_3$ in Raman and Optical Investigations at High Pressures. Phys. Rev. Appl. 8, 044014 (2017).

[164] P. Blaha, K. Schwarz, G. Madsen, D. Kvasnicka, and J. Luitz, WIEN 2k, Augmented Plane Wave Local Orbitals Program for Calculating Crystal Properties, Vienna, Austria, 2001.

[165] P. Demchenko, et al., Opt. Mater. 49 (2015) 94–99.

[166] L. Zhang, et al. J. Phys. Chem. C 122 (2018) 15220-15225

[167] T.V.Vu, et al., Opt. Mater. 86 (2018) 191–197.

[168] N. Pandey, et al., RSC Adv. 9 (2019) 29556-29565.

[169] Cook TR, Dogutan DK, Reece SY, et al. Solar energy supply and storage for the legacy and nonlegacy worlds. Chem. Rev. 2010; 110: 6474-6502.

[170] Hagfeldt A, Boschloo G, Sun L, et al. Dye-Sensitized Solar Cells. Chem. Rev. 2010; 110: 6595-6663.

[171] Petrovic M, Chellappan V, Ramakrishna S. Perovskites: Solar cells & engineering applications - materials and device developments. Sol. Energy. 2015; 122 :678-699.

[172] Song Z, Watthage SC, Phillips AB, et al. Pathways toward high-performance perovskite solar cells: review of recent advances in organo-metal halide perovskites for photovoltaic applications. J. Photonics Energy. 2016; 6 :022001.

[173] Woodward PM. Octahedral Tilting in Perovskites. I. Geometrical Considerations. Acta Cryst. 1997; B53 :32–43.

[174] Sahoo SK, Manoharan B, Sivakumar N. Perovskite Photovoltaics, Amsterdam (Netherlands): Elsevier Academic Press; 2018. Chapter 1, Why Perovskite and Perovskite Solar Cells?; p. 1–24.

[175] Kagan CR, Mitzi DB, Dimitrakopoulos CD. Organic-Inorganic Hybrid Materials as Semiconducting Channels in Thin-Film Field-Effect Transistors. Science. 1999; 286 :945-947.

[176] Mitzi DB, Chondroudis K, Kagan CR. Organic-inorganic electronics. J. Res. Dev. 2001; 45 :29-45

[177] Schwarz U, Wagner F, Syassen K, et al. Effect of pressure on the optical-absorption edges of $CsGeBr_3$ and $CsGeCl_3$. Phys. Rev. B. 1996; 53:12545-12548.

[178] Von Helmolt R, Wecker J, Holzapfel B, et al. Giant negative magnetoresistance in perovskitelike La2/3Ba1/3MnOx ferromagnetic films. Phys. Rev. Lett. 1993; 71: 2331-2333.

[179] Haeni JH, Irvin P, Chang W, et al. Room-temperature ferroelectricity in strained SrTiO3. Nature. 2004; 430: 758-761.

[180] Bednorz JG, Muller KA. Perovskite-type oxides—The new approach to high-Tc superconductivity. Rev. Mod. Phys. 1988; 60: 585-600.

[181] Malinkiewicz O, Yella A, Lee YH, et al. Perovskite solar cells employing organic charge-transport layers. Nature Photonics. 2014; 8: 128-132.

[182] Michael ML, Joël T, Tsutomu M, et al. Efficient Hybrid Solar Cells Based on Meso-Superstructured Organometal Halide Perovskites. Science. 2012 ; 338: 643-647.

[183] Eperon GE, Burlakov VM, Docampo P, et al. Morphological control for high performance, solution-processed planar heterojunction perovskite solar cells. Advanced Functional Materials. 2014; 24: 151–157.

[184] Manjunath V, Krishna R, Maniarasu S, et al. Perovskite Photovoltaics, Amsterdam (Netherlands): Elsevier Academic Press; 2018. Chapter 4, Perovskite Solar Cell Architectures; p. 89–121.

[185] Correa-Baena JP, Abate A, Saliba M, et al. The rapid evolution of highly efficient perovskite solar cells. Energy Environ. Sci. 2017; 10: 710-727.

[186] Stockhausen V, Mesquita I, Andrade L, et al. Insights in Perovskite Solar Cell Fabrication: Unraveling the Hidden Challenges of Each Layer. IEEE J. Photovoltaics. 2018; 8: 1029-1038.

[187] Burschka J, Pellet N, Moon SJ, et al. Sequential deposition as a route to high-performance perovskite-sensitized solar cells. Nature. 2013; 499: 316-319.

[188] Stoumpos CC, Malliakas CD, Kanatzidis MG. Semiconducting tin and lead iodide perovskites with organic cations: phase transitions, high mobilities, and near-infrared photoluminescent properties. Inorg. Chem. 2013; 52: 9019-9038.

[189] Weber D, CH3NH3PbX3, a Pb (II)-system with cubic perovskite structure. Z. Naturforsch. 1978; B33: 1443-1445.

[190] Weber D. CH3NH3SnBrxI3-x (x=0-3), a Sn(II)-System with cubic perovskite structure, Z. Naturforsch. 1978; B33: 862-865.

[191] Mitzi DB. Progress in Inorganic Chemistry. John Wiley & Sons, Inc., Hoboken, NJ; 1999. vol. 48, Synthesis, structure, and properties of organic-inorganic perovskites and related materials; p. 1-121.

[192] Miyasaka T. Perovskite photovoltaics: rare functions of organo lead halide in solar cells and optoelectronic devices. Chem. Lett. 2015; 44: 720-729.

[193] Eperon GE, Paterno GM, Sutton RJ, et al. Inorganic cesium lead iodide perovskite solar cells. J. Mater. Chem. 2015; A3: 19688-19695.

[194] Kulbak M, Cahen D, Hodes G. How important is the organic part of lead halide perovskite photovoltaic cells? efficient CsPbBr3 Cells. J. Phys. Chem. Lett. 2015; 6: 2452-2456.

[195] Murtaza G, Ahmad I. First principle study of the structural and optoelectronic properties of cubic perovskites CsPbM3(M=Cl, Br, I), Phys. B Condens. Matter. 2011; 406: 3222-3229.

[196] Yantara N. Bhaumik S. Yan F, et al. Inorganic halide perovskites for efficient light-emitting diodes. J. Phys. Chem. Lett. 2015; 6: 4360-4364.

[197] Ramasamy P, Lim DH, Kim B, et al. All-inorganic cesium lead halide perovskite nanocrystals for photodetector applications. Chem. Commun. 2016; 52: 2067-2070.

[198] Rodova M, Brozek J, Knizek K, et al. Phase transitions in ternary cesium lead Bromide. J. Therm. Anal. Calorim. 2003; 71: 667-673.

[199] Moller CK. Crystal structure and photoconductivity of cesium plumbohalides. Nature. 1958; 182: 1436.

[200] Lim A, Jeong SY. Twin structure by 133Cs NMR in ferroelastic CsPbCl3 crystal. Solid State Commun. 1999; 110: 131-136.

[201] Cola M, Massarotti V, Riccardi R, Sinistri C. Binary systems formed by lead bromide with (Li, Na, K, Rb, Cs and Tl) Br: a DTA and diffractometric study. Z. Naturforsch.1971; A26: 1328-1332.

[202] Carrero SG, Galian RE, Prieto JP. Organic-inorganic and all-inorganic lead halide Nanoparticles. Opt. Express. 2016; 24: 285-301.

[203] Trots D, Myagkota S. High-temperature structural evolution of caesium and rubidium Triiodoplumbates. J. Phys. Chem. Solids. 2008; 69: 2520-2526.

[204] Blaha P, Schwarz K, Madsen G, et al. WIEN 2k, Augmented Plane Wave Local Orbitals Program for Calculating Crystal Properties, Vienna, Austria, 2001.

[205] Moreira RL, Anderson D. Comment on "Prediction of Lattice Constant in Cubic Perovskites" .J. Phys. Chem. of Solids. 2007; 68: 1617-22.

[206] Akihiro Kojima et al., « Organometal Halide Perovskites as Visible-Light Sensitizers for Photovoltaic Cells », **J**. Am. Chem. Soc 131, n° 17 (6 mai 2009): 6050-51, https://doi.org/10.1021/ja809598r.

[207] Martin A. Green et al., « Solar Cell Efficiency Tables (Version 51) », *Progress in Photovoltaics: Research and Applications* 26, n° 1 (janvier 2018): 3-12, https://doi.org/10.1002/pip.2978.

[208] Wei E. I. Sha et al., « Quantifying Efficiency Loss of Perovskite Solar Cells by a Modified Detailed Balance Model », Adv. Energy Mater. 8, nº 8 (mars 2018): 1701586, https://doi.org/10.1002/aenm.201701586.

[209] Aslihan Babayigit et al., « Toxicity of Organometal Halide Perovskite Solar Cells », *Nat. Mater* 15, nº 3 (mars 2016): 247-51, https://doi.org/10.1038/nmat4572.

[210] Bekele Hailegnaw et al., « Rain on Methylammonium Lead Iodide Based Perovskites: Possible Environmental Effects of Perovskite Solar Cells », J. Phys. Chem. Lett 6, nº 9 (7 mai 2015): 1543-47, https://doi.org/10.1021/acs.jpclett.5b00504.

[211] Nicholas Aristidou et al., « The Role of Oxygen in the Degradation of Methylammonium Lead Trihalide Perovskite Photoactive Layers », Angew. Chem. Int. Ed 54, nº 28 (6 juillet 2015): 8208-12, https://doi.org/10.1002/anie.201503153.

[212] Jun Pan et al., « Highly Efficient Perovskite-Quantum-Dot Light-Emitting Diodes by Surface Engineering », Adv. Mater 28, nº 39 (octobre 2016): 8718-25, https://doi.org/10.1002/adma.201600784.

[213] Xiaoli Zhang et al., « All-Inorganic Perovskite Nanocrystals for High-Efficiency Light Emitting Diodes: Dual-Phase $CsPbBr_3$ -$CsPb_2Br_5$ Composites », Adv. Funct. Mater. 26, nº 25 (juillet 2016): 4595-4600, https://doi.org/10.1002/adfm.201600958.

[214] Guan Z, Wu Y, Wang P, Zhang Q, Wang Z, Zheng Z, Liu Y, Dai Y, Whangbo M-Hwan, Huang B, Perovskite photocatalyst $CsPbBr_{3-x}I_x$ with a bandgap funnel structure for H2 evolution under visible light, APPL CATAL B-ENVIRON (2019), https://doi.org/10.1016/j.apcatb.2019.01.019.

[215] Bin Wang et al., « Ionic Liquid-Induced Strategy for Porous Perovskite-like PbBiO2Br Photocatalysts with Enhanced Photocatalytic Activity and Mechanism Insight », APPL CATAL B-ENVIRON 206 (juin 2017): 127-35, https://doi.org/10.1016/j.apcatb.2016.12.049.

[216] Jianxu Ding et al., « High Detectivity and Rapid Response in Perovskite CsPbBr 3 Single-Crystal Photodetector », J. Phys. Chem. C 121, nº 9 (9 mars 2017): 4917-23, https://doi.org/10.1021/acs.jpcc.7b01171.

[217] Jianxu Ding et al., « High-Quality Inorganic–Organic Perovskite CH3NH3PbI3 Single Crystals for Photo-Detector Applications », J. Mater. Sci. 52, nº 1 (janvier 2017): 276-84, https://doi.org/10.1007/s10853-016-0329-2.

[218] Qingsen Zeng et al., « Polymer-Passivated Inorganic Cesium Lead Mixed-Halide Perovskites for Stable and Efficient Solar Cells with High Open-Circuit Voltage over 1.3 V », Adv. Mater 30, nº 9 (mars 2018): 1705393, https://doi.org/10.1002/adma.201705393.

[219] Abhishek Swarnkar et al., « Quantum Dot–Induced Phase Stabilization of a-CsPbI3 Perovskite for High-Efficiency Photovoltaics », s. d., 5.

[220] Rebecca J. Sutton et al., « Bandgap-Tunable Cesium Lead Halide Perovskites with High Thermal Stability for Efficient Solar Cells », Adv. Energy Mater. 6, nº 8 (avril 2016): 1502458, https://doi.org/10.1002/aenm.201502458.

[221] C.K. Moller, Crystal structure and photoconductivity of cesium plumbohalides, Nature 182 (1958) 1436.

[222] A. Lim, S.Y. Jeong, Twin structure by 133Cs NMR in ferroelastic CsPbCl3 crystal, Solid State Commun. 110 (1999) 131 e 136.

[223] M. Cola, V. Massarotti, R. Riccardi, C. Sinistri, Binary systems formed by lead bromide with (Li, Na, K, Rb, Cs and Tl) Br: a DTA and diffractometric study, Z. Naturforsch. A 26 (1971) 1328 e 1332.

[224] Yanbo Gao et al., « CsPbBr3 Perovskite Nanoparticles as Additive for Environmentally Stable Perovskite Solar Cells with 20.46% Efficiency », *Nano Energy* 59 (mai 2019): 517-26, https://doi.org/10.1016/j.nanoen.2019.02.070.

[225] R. I. Eglitis and A. I. Popov, "Systematic trends in (001) surface ab initio calculations of ABO3 perovskites", J. Saudi Chem. Soc. 22, 459-468 (2018)

[226] R. I. Eglitis, "Ab initio calculations of the atomic and electronic structure of BaZrO3 (111) surfaces", Solid State Ionics 230, 43-47 (2013).

[227] Thang Phan Nguyen et al., « Facile Synthesis of CsPbBr 3 /PbSe Composite Clusters », Sci. Technol. Adv. 19, no 1 (31 décembre 2018): 10-17, https://doi.org/10.1080/14686996.2017.1412231.

Articles:

1) H. Zitouni et al, "*Physical properties of perovskite $SrHfO_3$ compound doped with S for photovoltaic applications: the ab initio study*", Journal of Applied Physics A, doi.org/10.1007/s00339-020-03987-4, 2020.

2) H. Zitouni et al., "*How the strain effects decreases the band gap energy in the $CsPbX_3$ perovskite compounds?*" Journal of phase transition, 10.1080/01411594.2020.1746964, 2020.

3) H. Zitouni et al., "*Electronic, transport and optical properties in perovskite compound $LaGaO_3$",* Journal of Materials Research Express, /doi.org/10.1088/2053-1591/ab778c, 2020.

4) H. Zitouni et al., *"Electronic, optical and transport properties of perovskite $BaZrS_3$ compound doped with Se for photovoltaic applications",* Journal of Chemical Physics, doi.org/10.1016/j.chemphys.2020.110923, 2020.

5) H. Zitouni et al., "Doping effect of Iodine on electronic and optical properties of perovskite $CsPbBr_3$ compound for photovoltaic applications: ab initio calculations", Journal of Electron Spectroscopy and Related Phenomena, doi.org/10.1016/j.elspec.2021.147043, 2021.